Spring 2015

Dynamics of transitions between capillary stable states under weightlessness

Praveen Srikanth
Purdue University

Graduate School Form 30
Updated 1/15/2015

PURDUE UNIVERSITY
GRADUATE SCHOOL
Thesis/Dissertation Acceptance

This is to certify that the thesis/dissertation prepared

By Praveen Srikanth

Entitled

DYNAMICS OF TRANSITIONS BETWEEN CAPILLARY STABLE STATES UNDER WEIGHTLESSNESS

For the degree of Master of Science in Aeronautics and Astronautics

Is approved by the final examining committee:

Dr. Steven H. Collicott
Chair

Dr. Stephen D. Heister

Dr. Timothée Pourpoint

To the best of my knowledge and as understood by the student in the Thesis/Dissertation Agreement, Publication Delay, and Certification Disclaimer (Graduate School Form 32), this thesis/dissertation adheres to the provisions of Purdue University's "Policy of Integrity in Research" and the use of copyright material.

Approved by Major Professor(s): Dr. Steven H. Collicott

Approved by: Dr. Weinong Chen 4/22/2015

Head of the Departmental Graduate Program Date

DYNAMICS OF TRANSITIONS BETWEEN CAPILLARY STABLE STATES UNDER WEIGHTLESSNESS

A Thesis

Submitted to the Faculty

of

Purdue University

by

Praveen Srikanth

In Partial Fulfillment of the

Requirements for the Degree

of

Master of Science in Aeronautics and Astronautics

May 2015

Purdue University

West Lafayette, Indiana

ACKNOWLEDGMENTS

I would like to take this opportunity to thank my advisor, Dr. Collicott, for giving me this wonderful chance to work on this problem and supporting me throughout the journey. His patience, guidance and experience in the field were vital throughout my research. I would also like to thank Dr. Heister and Dr. Pourpoint for participating in my defense committee.

I would like to thank the staff at ECN and specially Al Mondero for helping me access the available computational resources and for the additional storage which helped me complete this work. I would also like to thank Dr. Blaisdell for letting me use his resources on ITaP's compute server, Rossmann.

I am grateful to the administrative staff in the AAE department who helped me get through all the hurdles of graduate school and answered my endless questions and mails. Tyler Voskuilen, during his time as a post-doctoral scholar at Purdue was a fantastic resource on all things OpenFOAM. His suggestions and timely troubleshooting were very important for progress in this project.

Special thanks to everyone in my research group who helped me settle down initially and whose valuable advice got me to where I am right now. Finally, I would like to thank my family and friends for putting up with my long and dreary stories about graduate school and for their absolute and unquestioned support in all my dreams and efforts.

TABLE OF CONTENTS

Page

LIST OF TABLES

LIST OF FIGURES

Figure Page

Figure Page

Figure Page

Figure Page

SYMBOLS

Bo	Bond number
ρ	Density
g	Acceleration due to gravity
r	Characteristic radius
σ	Surface tension
θ	Contact angle
R_c	Radius of curvature of interface
R_T	Radius of tube
V_{min}	Minimum volume of existence for a plug solution
V	Dimensional volume
v	Non-dimensional volume
e	Non-dimensional energy
A_{FS}	Free surface area
A_{wetS}	Wetted surface area
R_b	Non-dimensional bend radius
R_{1N}	Inner bend radius
AR	Aspect ratio
ϕ	Flux
U	Velocity
S_ϕ	Source term
t	Time
Co	Courant number
g_b	Gradient
p	Pressure
κ	Local curvature

F_{sv}	Surface tension force
β	Level set function
ν	Kinematic viscosity
μ	Dynamic viscosity
α	Volume fraction function
S	Surface area
E_{pot}	Potential energy
E_{kin}	Kinetic energy
E	Energy
E_{dryS}	Dry surface energy
E_{wetS}	Wetted surface energy
E_{FS}	Free surface energy
A_{wetS}	Wetted surface area
A_{dryS}	Dry surface area
σ_{wetS}	Wetted surface energy density
σ_{dryS}	Dry surface energy density
τ	Transition time
Re	Reynolds number
Oh	Ohnesorge number

ABBREVIATIONS

EMU	Extra-vehicular Mobility Unit
STS	Space Transportation System
MEMS	Microelectromechanical Systems
3D	Three Dimensional
2D	Two Dimensional
NASA	National Aeronautics and Space Administration
VOF	Volume of Fluid
TDMA	Tri-diagonal Matrix Algorithm
DSMC	Direct Simulation Monte Carlo
MD	Molecular Dynamics
PCG	Preconditioned Conjugate Gradient
PBi-CG	Preconditioned Bi-Conjugate Gradient
GAMG	Geometric Algebraic Multi Grid
DIC	Direct Incomplete Cholesky
CSF	Continuum Surface Force
SLIC	Simple Line Interface Calculation
PLIC	Piecewise Linear Interface Calculation
LVIRA	Least Squares Volume of Fluid Interface Reconstruction Algorithm
PROST	Parabolic Reconstruction of Surface Tension
CLSVOF	Combined Level Set and Volume of Fluid
DNS	Direct Numerical Simulation
MULES	Multi Dimensional Universal Limiter with Explicit Solution
PISO	Pressure Implicit with Splitting of Operator
SIMPLE	Semi Implicit Method for Pressure Linked Equations

ABSTRACT

Srikanth, Praveen MSAA, Purdue University, May 2015. Dynamics of Transitions between Capillary Stable States under Weightlessness. Major Professor: Steven H. Collicott.

The study of two phase systems with one of the phases obstructing the other is of importance in a lot of fields. Liquid droplets in airways and air bubbles in the blood stream both fall under this category of problems. Helium bubbles in hydrazine fuel lines of satellites also have been found to cause frequent thruster shutdown and also seriously affect spacecraft control. Studies have been carried out until now to look at static equilibrium topologies and stability of such two phase systems in straight, bent and laterally compressed capillaries. In this investigation we look at the dynamics of the transitions between the stable topologies identified for a straight cylindrical capillary. The break up of the interface could adversely affect system performance. OpenFOAM is used to compute transitions from a stable droplet to a plug or the reverse by suitably adding or removing the obstructing phase through inlet patches on the wall of the cylinder.

The main parameters presented are the non-dimensional energy, non-dimensional transition times, non-dimensional transition volumes and the general dynamics of the transitions itself. Before computing transitions the static equilibrium topologies computed by OpenFOAM are compared with those predicted by Surface Evolver and are found to be within acceptable deviations. The grid dependence of these transitions has also been studied. Transitions are computed for contact angles in the range of 10° to 170°. Different modes of transitions are observed depending on the contact angle of the case for both the types of transitions. The transition volumes are compared to the volume of existence limits for the corresponding initial topology at a particular contact angle for both the transitions.

1. INTRODUCTION & LITERATURE REVIEW

When considering two-phase fluid systems in zero gravity it is often possible that a wall bounded volume of one phase could partially or completely occlude the movement of the other. The Bond number defined as $Bo = \rho g r^2/\sigma$ which relates the gravitational force to the surface tension forces. Here ρ is the fluid density, g is the acceleration due to gravity, r is the characteristic length scale and σ is the surface tension coefficient. In low gravity, the Bond number is generally very small. This means that in these conditions the surface tension forces play a major role in the physics of two-phase fluid problems.

The study of such occlusions in different capillary geometries has implications in multiple fields. One such example of interest is the development of liquid structures in airways leading to the lungs. Another example related to the same field would be the formation of air bubbles in blood vessels. Most studies in the medical community [1,2] related to meniscus formation in lungs focussed on axisymmetric topologies and also assumed that the liquid completely wets the surface. It was later shown by Collicott et al. [3] that this is not necessarily always the case and there may be other asymmetric liquid topologies which could exist. They also showed that the typical Bond numbers associated with these problems is around 0.033 which justifies neglecting the effect of gravity in these studies.

On the engineering side there have been numerous problems related to two phase occlusions in tubes which have plagued various space related missions. A typical and often quoted example is the case of formation of helium bubbles in hydrazine fuel lines which are used in hydrazine arc-jet thrusters. Helium gas is used to keep the hydrazine pressurized and this might enter the fuel lines during operation which might cause the system to sputter and misfire. The gas also dissolves in hydrazine at these high pressures and can later be released when lower pressures are encountered.

These gas bubbles would cause the thruster to shutdown which would mean that there would be much frequent restarts and as a result the life of the thruster might reduce [4, 5]. It also makes satellite control less precise and therefore is wasteful. A recent problem faced in the International Space Station was the failure of the Russian built oxygen generator which failed due to liquid occlusion in one of the pipes [6, 7]. The collection of gas bubbles in coolant pipes can also be seen listed as a possible mode of failure in the EMU critical items list catalogued during the aftermath of STS-107 [8, 9]. It is also relevant in formation of bubbles in MEMS where the small size causes very low Bond numbers and is similar in treatment to capillary surfaces in zero gravity. For example the problem of bubble occlusion occurs in lab on chip systems in cases where chemical reactions are carried out in nano scale channels [10].

Slobozhanin et al. [11] analytically calculated the possible connected axisymmetric shapes and their stability in a circular cylindrical vessel in the presence of acceleration directed in the axial direction and under weightlessness. In this study the region between the free surface and the cylinder wall is occupied by the gas but owing to the duality in the solution the results can be interpreted for the case where the liquid and gas positions are interchanged by taking the wetting angle to be $180^\circ - \theta$.

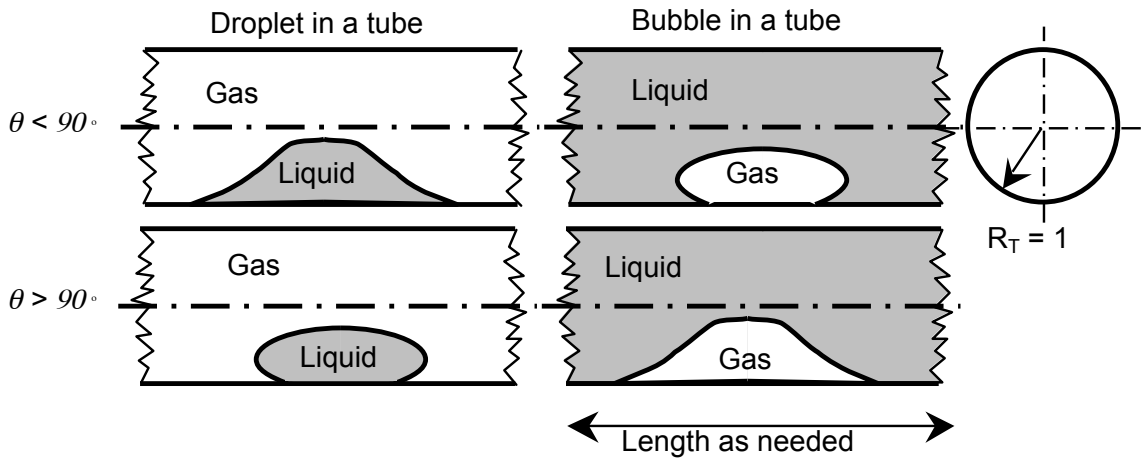

Figure 1.1.: Duality of solution when liquid and gas regions are interchanged. The contact angle is measured in the liquid phase.

It was shown that the shape and stability of these axisymmetric structures depended on three parameters viz. the relative volume, wetting angle, and the Bond number. The Bond number plays a major role only when one of the contact lines was on the flat wall of the cylinder. It was seen that a stable equilibrium for an annular surface with both contact lines on the cylindrical walls cannot exist for wetting angles greater than 59°. It was shown that for contact angles less than 59° there exists both minimum and maximum volume stability limits. When the volume is greater than the maximum stability limit the liquid could completely occlude the passage and when the volume is less than the minimum stability limit the liquid would collapse to become a non-axisymmetric wall bounded droplet.

Collicott et al. [12] extended the work by Slobozhanin and computed the minimum energy solutions for different contact angles and volumes using Surface Evolver [13]. The static equilibrium shape of the obstructing field was found to be either a plug, annulus or a droplet. The first two solutions are axisymmetric while the droplet is asymmetric in nature. The annulus has two contact lines on the cylindrical walls with a single connected free surface which does not cross the axis.

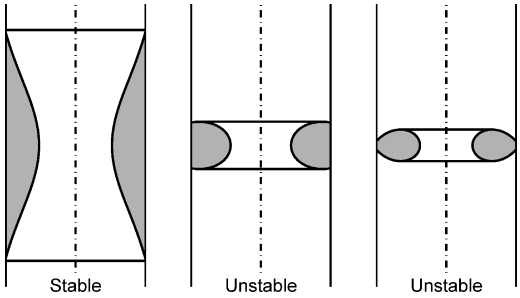

Figure 1.2.: Examples of Axisymmetric Annular Solutions. Only one is stable in 3D.

The liquid plug solution is similar to the annular solution in that it has two contact lines but unlike the annular solution it also has two free surfaces which are not connected. This type of topology completely occludes the passage. These plug solutions can be calculated rather easily analytically. Collicott et al. calculated the minimum volumes at which a plug type solution could exist and showed that such

a topology is possible for all contact angles. In the case of a plug the free surfaces are identical spherical caps. In a tube of radius R_T the radius of curvature of the interface turns out to be,

$$R_c = \frac{R_T}{\cos\theta} \tag{1.1}$$

They showed that the minimum volumes of existence for these plugs are when the two spherical caps meet at either the center which is the case with acute contact angles or at the perimeter of the tube as in the case of obtuse contact angles (Figure 1.3).

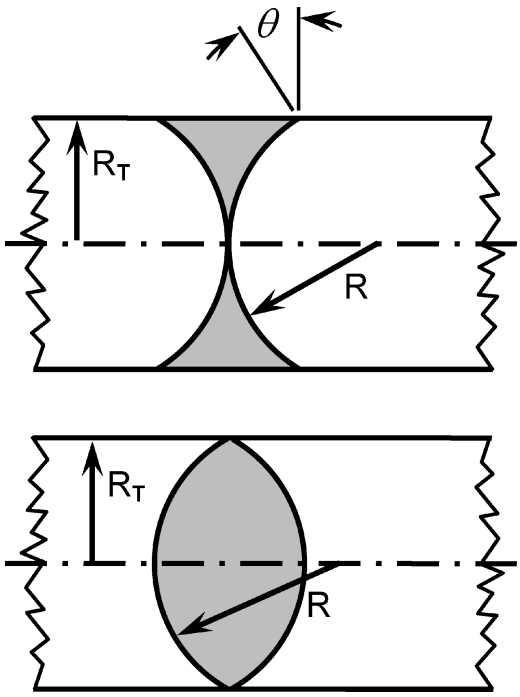

Figure 1.3.: Minimum volume conditions for plug type solution for wetting (top) and non-wetting (bottom) liquids

The minimum volume can be calculated from the volume of the two spherical caps. For a tube of radius R_T , this is given as,

$$V_{min} = \begin{cases} 2\pi R_T^3\left(\frac{1-\sin\theta}{\cos\theta}\right) - \frac{2\pi}{3}R_T^3\left(\frac{2-3\sin\theta+\sin^3\theta}{\cos^3\theta}\right) & \text{for } 0^\circ \le \theta \le 90^\circ, \\ -\frac{2\pi}{3}R_T^3\left(\frac{2-3\sin\theta+\sin^3\theta}{\cos^3\theta}\right) & \text{for } 90^\circ \le \theta \le 180^\circ \end{cases} \tag{1.2}$$

The nondimensional volume v is obtained from the dimensional volume V by $v = V/R_T^3$. For unity surface tension the energies are computed as,

$$E = A_{FS} - A_{wetS}\cos\theta \tag{1.3}$$

where A_{FS} is the surface area of both caps of the plug and A_{wetS} is the surface area of the cylinder wall in contact with the liquid. Collicott et al. showed that these areas for a plug are given by,

$$A_{FS} = \frac{4\pi R_T^2}{(1+\sin\theta)} \tag{1.4}$$

$$A_{wetS} = \begin{cases} 4\pi R_T^2 \frac{(1-\sin\theta)}{\cos\theta} & \text{for } 0^\circ \leq \theta \leq 90^\circ, \\ 0 & \text{for } 90^\circ \leq \theta \leq 180^\circ \end{cases} \tag{1.5}$$

The above formulae for the wetted areas are for the case when the plugs are at minimum volume condition. For larger volumes the wetted areas would include the surface area of the extra cylindrical liquid column due to the excess volume. Throughout this section the contact angle is measured inside the liquid plug.

The third solution of interest is the asymmetric droplet. The asymmetric droplet is a wall bounded topology with a single contact line on the wall of the cylinder. These droplet solutions were calculated for the whole space of volume and contact angle with the help of Surface Evolver. Collicott et al. plotted the non-dimensional energies and pressures for different contact angles over the volume domain. They proved that for any given volume the liquid will always exist as a single volume rather than split into two or more smaller volume regions as the energy of the single volume is always lesser than the total energies of the multiple volumes. They showed that this was true for all the three topologies. Throughout the study comparisons were made with the energy of a free spherical droplet which could exist in the tube.

Figure 1.4 shows the minimum energy solutions in the volume-contact angle plane and also shows the minimum and maximum volume lines for the plug and droplet

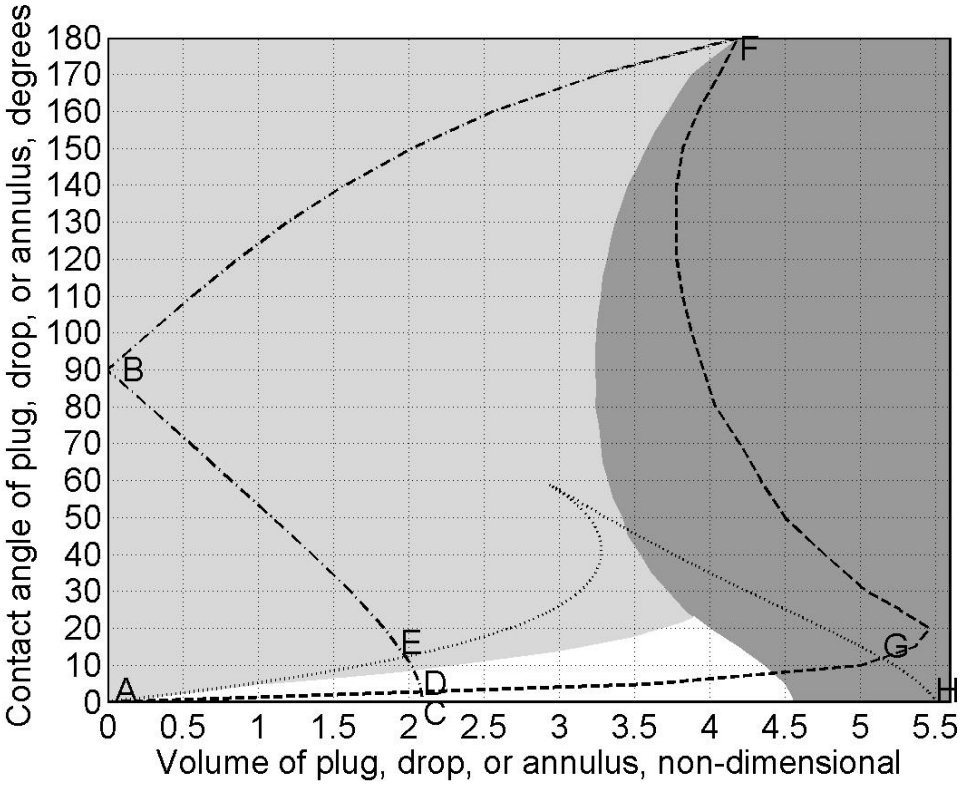

Figure 1.4.: Map of existence and minimum energy solutions. White = Annulus, Light Grey = Droplet, Dark Grey = Plug. Dashed line (FGDA) = Maximum volume of existence for droplet, Dash-dot line (CDEBF) = Minimum volume of existence for plug, Dotted line (AEGH) = Maximum volume of existence for annulus

solutions respectively. The plug is the minimum energy solution for most large volumes for all contact angles. The plug solution is possible for volumes beyond what is plotted in the map and is limited only by the length of the tube. At low volumes the asymmetric wall bounded droplet becomes the minimum energy solution for most contact angles. There is a small region at low contact angles (less than 21°) and at certain volumes where the annulus becomes the low energy solution. This region is shown in the map (Figure 1.4) in white. Collicott et al. also concluded that the free droplet is never the minimum energy solution at any volume.

Braun [14] studied the effect of tube bending on static equilibrium solutions and compared it with straight tube solutions under microgravity. Figure 1.5 shows the typical geometry which was studied. Here $R_b = R1_N/R_T$, where $R1_N$ is the inner bend radius and R_T is the centerline radius, is the non dimensional bend radius. Solutions were numerically computed using Surface Evolver for bend radii ranging from 2 to 50. Braun showed that there are four distinct topologies which are possible in the case of a bent tube, viz. plug, annulus, inner wall droplet and outer wall droplet. It was shown that the plug solution can still be solved analytically as the ends are spherical caps and are in contact with the tube wall. On comparing the minimum volume with the straight tube case it was found that in the case of a non wetting liquid the minimum volumes were found to be almost the same while the minimum volume for a wetting liquid was found to increase with decrease in bend radius.

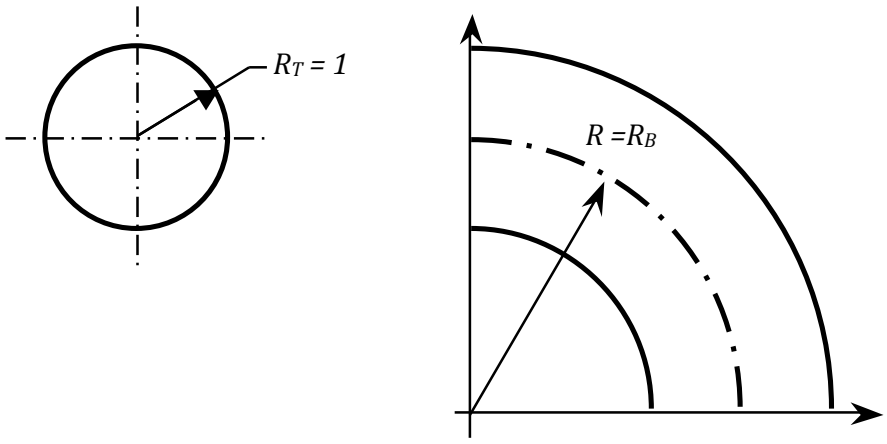

Figure 1.5.: Geometry of Bent Tube with tube radius of 1 and $R_b \geq 1$ [14]

The annular topology is nonexistent for bend radii below 5 and can be found only at low contact angles at large bend radii. The annulus was found to be the minimum energy solution only for a bend radius of 50 and for contact angles less than 10 in the volume range of 2.6 to 4.5. This in comparison to straight tube solutions is a very small region. Braun argued that due to the difference in arc length between

the inner and outer radial walls it is necessary to consider the inner wall droplet and outer wall droplet as two different solutions. It was found that the outer wall droplet was the lesser energy solution and for small volumes at all contact angles it was the equilibrium solution. As the bend radius decreases the maximum volume for the outer wall droplet was seen to increase while the maximum volume for the inner wall droplet decreased and at bend radii below 6 the inner wall droplet was completely eliminated for low contact angles. Figure 1.6 and Figure 1.7 show the minimum energy solutions along with maximum and minimum volumes of existence for bend radii of 2 and 50. It was concluded that as the bend radius increases the solutions converged towards that of a straight cylinder as the straight cylinder is essentially a bent tube with infinite bend radius.

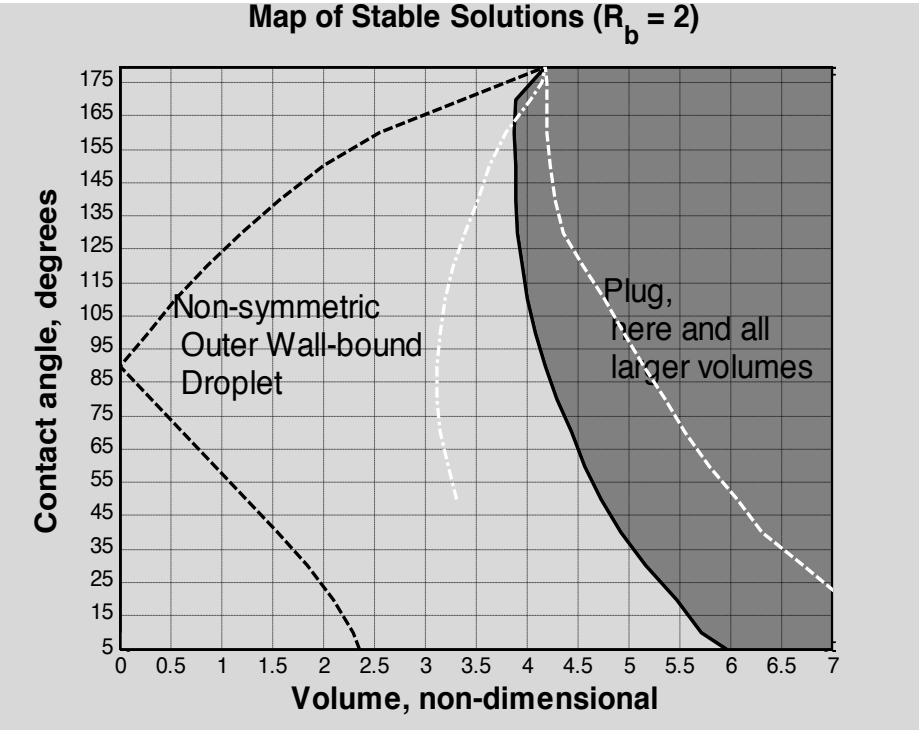

Figure 1.6.: Map of lowest energy solutions for $R_b = 2$ in the V-θ space. Black Dash Line = Minimum Plug Volume, White Dash-Dot Line = Maximum inner wall-bound Droplet Volume, White Dash Line = Maximum Volume for Outer Wall-Bound Droplet [14]

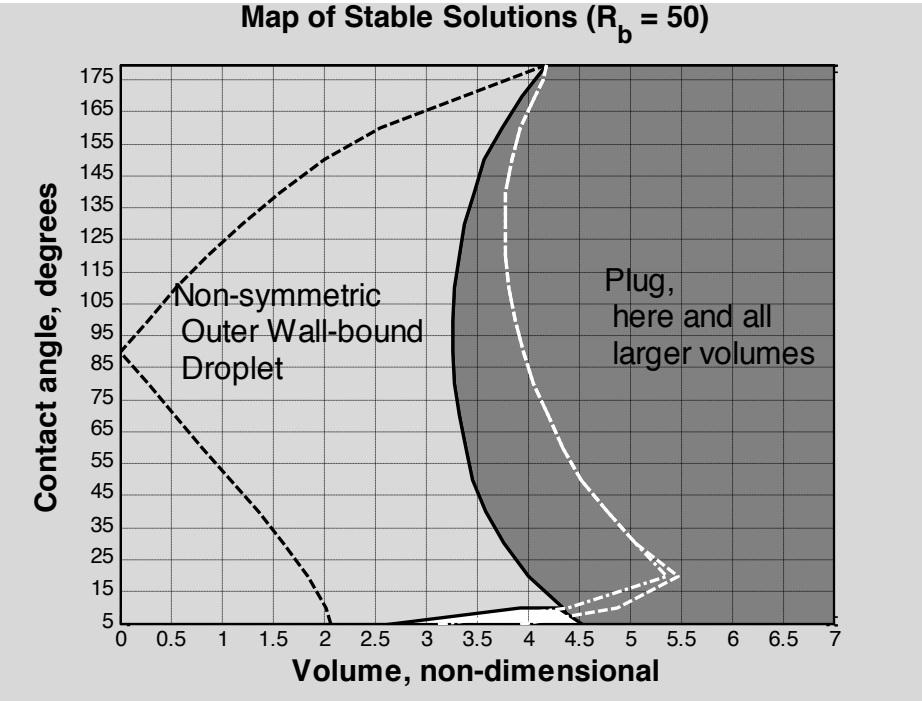

Figure 1.7.: Map of lowest energy solutions for $R_b = 50$ in the V-θ space. The white space corresponds to the region where the annulus is the minimum energy solution. Black Dash Line = Minimum Plug Volume, White Dash-Dot Line = Maximum inner wall-bound Droplet Volume, White Dash Line = Maximum Volume for Outer Wall-Bound Droplet [14]

Another study of liquid interfaces in tubes under zero gravity was with laterally compressed tubes by Jaron [15]. Jaron defines lateral compression by means of the aspect ratio which is the ratio of the height to the width. It was found that there were six possible solutions in the case of a laterally compressed tube, viz. annulus, plug, liquid bridge and three variations of the wall bounded droplet. Due to the lateral compression the wall bounded droplet could now exist on the curved part, the flat part or can be spread across both.

Jaron compared the equilibrium solutions with that of the perfectly circular cylinder and found that even for very small lateral compressions to the tune of AR = 1.1 the solutions changed drastically due to the possibility of the extra three topologies.

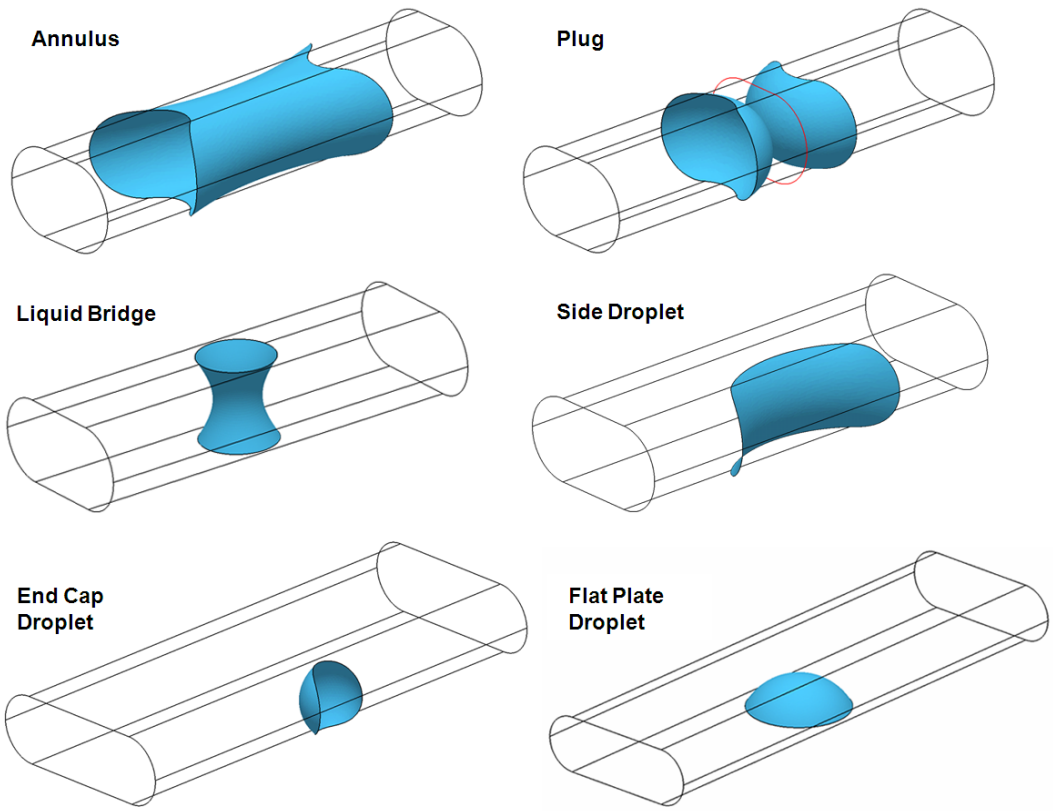

Figure 1.8.: Annulus AR = 1.5 V = 3.0 $\theta = 10°$; Plug AR = 1.5 V = 3.5 $\theta = 10°$; Liquid Bridge AR = 2.0 V = 1.2 $\theta = 60°$; Side Droplet AR = 3.0 V = 3.2 $\theta = 70°$; End Cap Droplet AR = 3.0 V = 0.2 $\theta = 120°$; Flat Plate Droplet AR = 3.0 V = 5.0 $\theta = 60°$ [15]

Unlike in the case of the perfectly circular cylinder where the droplet to plug boundary is determined by the minimum energy, in the case of the laterally compressed cylinder it is determined by the maximum volume of the droplet. This means that the side droplet is always the lower energy solution than the plug in this case. The annulus was found to be the minimum energy solution for a small region as shown in

Figure 1.9 but was not existent under $v = 1.0$. Other topologies such as the liquid bridge and the flat plate droplet are either non existent or have a higher energy.

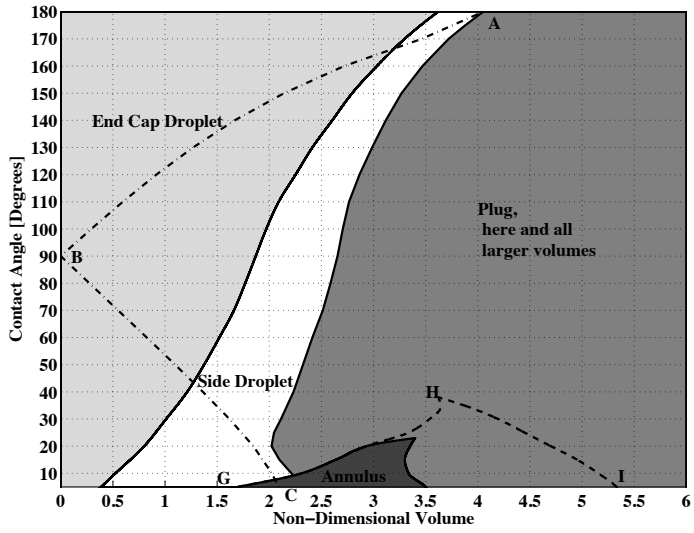

Figure 1.9.: Minimum Energy Topology Map for a Circular Tube with Lateral Compression of AR = 1.1 [15]

She found that when the aspect ratio increased to 1.5 the droplet plug boundary moved to higher volumes and was no longer bounded by the maximum droplet volume but rather by the minimum energy for contact angles below 130°. Also the energy of the annulus was never the minimum. At AR = 3.0 the end cap droplet is almost eliminated and existed only for $v < 1.0$ and the side droplet becomes the minimum energy solution till $v = 7$ for some contact angles. Following the trend for AR = 5.0 the side droplet was the minimum energy solution for volumes as high as 9. It was also seen that there was not much difference in the stability chart when the aspect ratio changed from 1.5 to 2.0. Thus it was concluded that one way to prevent a liquid from completely occluding the tube would be to have a high lateral compression.

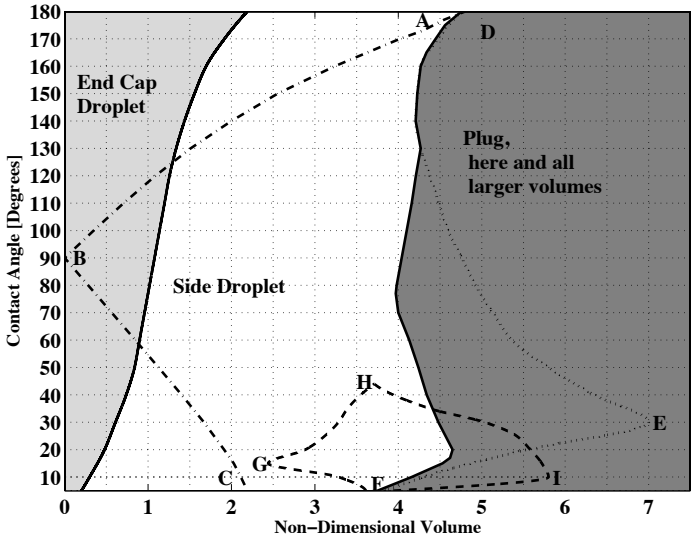

Figure 1.10.: Minimum Energy Topology Map for a Circular Tube with Lateral Compression of AR = 1.5 [15]

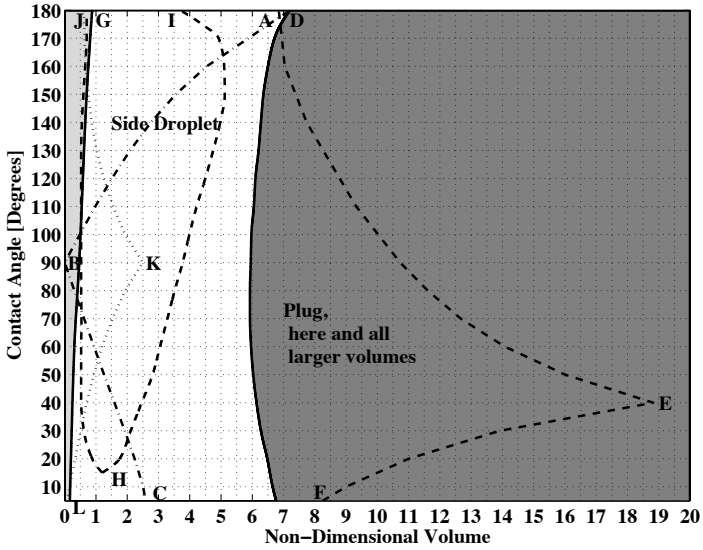

Figure 1.11.: Minimum Energy Topology Map for a Circular Tube with Lateral Compression of AR = 3.0 [15]

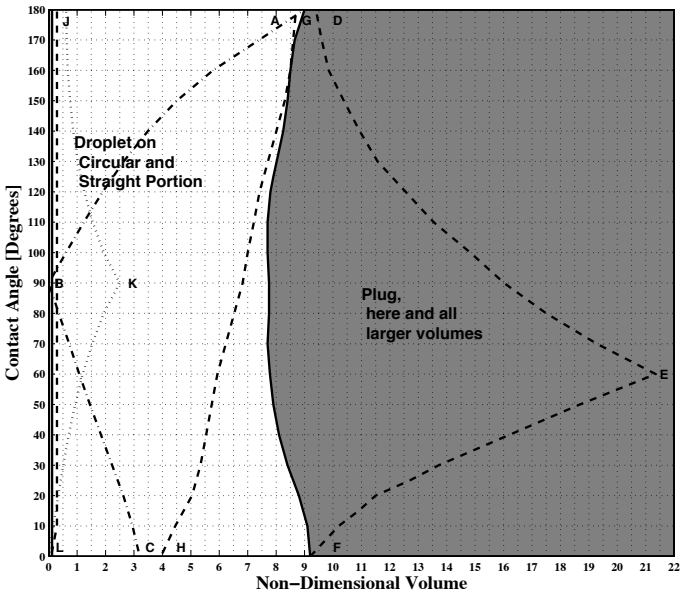

Figure 1.12.: Minimum Energy Topology Map for a Circular Tube with Lateral Compression of AR = 5.0 [15]

With the goal of comparing these results with real experimental data a couple of microgravity student experiments were carried out under the Reduced Gravity Education Flight Program run by NASA in 2007, 2009, and 2012. The first two experiments were focussed on trying to form the three topologies of interest by having certain volumes of liquid in tubular containers. An attempt was also made to study the stability of these topologies and compare them to results from Surface Evolver. The later experiment focussed on characterizing the breakup and transition from one topology to another which is the goal of this current study. This was to be achieved by means of either liquid addition or by boundary modifications. The data from this experiment was not satisfactory owing to the vibrations induced during the flight on the experimental setup. It is thus very important to evaluate the available computational methods to model transitions from one topology to another. This study focuses on modeling the transitions between the three different topologies

possible in a circular cylindrical tube with the help of the computational package OpenFOAM [16]. Understanding the interim stages during the transition between equilibrium stable topologies would help avoid disruptions to system operations due to interface breakup.

This thesis is divided into six chapters. The second chapter describes the finite volume method and its implementation in OpenFOAM. The various interface tracking methods available and specifically the use of the Volume of Fluid (VOF) method in interFoam are discussed in the third chapter. The fourth and the fifth chapters define the problem and the computational results are discussed in detail. The final chapter mentions the conclusions drawn from this effort and some potential future work that could be done to improve our understanding about zero gravity liquid interfaces.

2. FINITE VOLUME METHODS - OpenFOAM

OpenFOAM is the computational package of choice owing to its easy availability and satisfactory performance in previous multiphase studies. OpenFOAM is an open source computational toolbox which is used to solve a wide variety of problems in fluid mechanics, electromagnetics, solid dynamics and even finance. It includes capabilities to carry out Direct Simulation Monte Carlo (DSMC) and Molecular Dynamics (MD) computations. It also has numerous inbuilt utilities for mesh generation and conversion from other formats along with various post processing tools. The entire toolbox is written in the latest version of C++ and is one of the best examples of impeccable C++ programming. Being open source, users are encouraged to code additional capabilities to improve existing solvers or to completely build and compile a new solver using the basic framework provided by OpenFOAM. This is largely enabled by the simple implementation of all the necessary functions with classes and libraries. In this chapter, the finite volume method and its implementation will be discussed. This has already been discussed in detail by many authors [16–21] and the structure of this chapter will be similar to the Programmers Guide to OpenFOAM.

The equations which govern physical phenomena are mostly in the form of partial differential equations. Unless the equations are very basic it is much easier to convert them to simple algebraic relations and solve the resulting algebraic equations as a matrix. In fluid mechanics, most solution algorithms try to reduce these governing equations to a sparse matrix which can then be solved with the help of the tridiagonal matrix algorithm (TDMA) or iterative solvers. This process of converting an equation which is defined for a continuous domain into discrete algebraic relations is known as discretization. Discretization is mainly of two steps - first the solution domain has to be discretized into discrete points connected by lines called a grid and then the equations are discretized into algebraic relations on the grid.

2.1 Discretizing the Domain

The solution domain in most fluid and solid mechanics problems consists of the three spatial dimensions (x, y, and z) and time. Time does not come into the solution in the case of steady computations. But, OpenFOAM mostly deals with unsteady computations and hence temporal discretization is also vital. The three spatial directions are discretized with the help of a mesh which covers the entire solution domain. The most basic elements of a mesh are vertices which are connected by lines to form edges. A collection of edges form a face and a collection of faces form a cell. Three dimensional meshes are made up of cells arranged in a particular fashion to fill up the whole region. This breaks up the domain and the problem now becomes discrete and the equations can now be solved at these discrete steps. The cells in a mesh do not overlap and can be of different forms, most commonly tetrahedral or hexagonal. Each cell is considered as a control volume.

The faces of a cell are shared with only one other neighboring cell. The area of the face is computed as a vector normal to the face pointing outwards. All the information of the owner and neighboring cells for a particular face are catalogued in the case folder. Faces are categorized as either internal or boundary faces. Boundary faces are the faces which are along the boundaries of the solution domain and all other faces are internal faces. OpenFOAM has the capability to deal with unstructured meshes which makes the process of mesh generation much easier. This also means that problems with much complex geometries can now be solved easily. Mesh orthogonality is a parameter which greatly affects the solution. Orthogonal meshes are those meshes where the normal vector of a face coincides with the line joining the cell centers of the two adjacent cells which share the face. Additional correctors are needed when solving cases with non orthogonal meshes. The handling of non-orthogonality will be discussed further in this chapter.

Temporal discretization involves splitting of the time domain into discrete time steps. The time steps can be constant or could vary depending on certain flow and

fluid properties. Variable time stepping based on the Courant Friedrichs Levy condition will be discussed in later parts of Chapter 3.

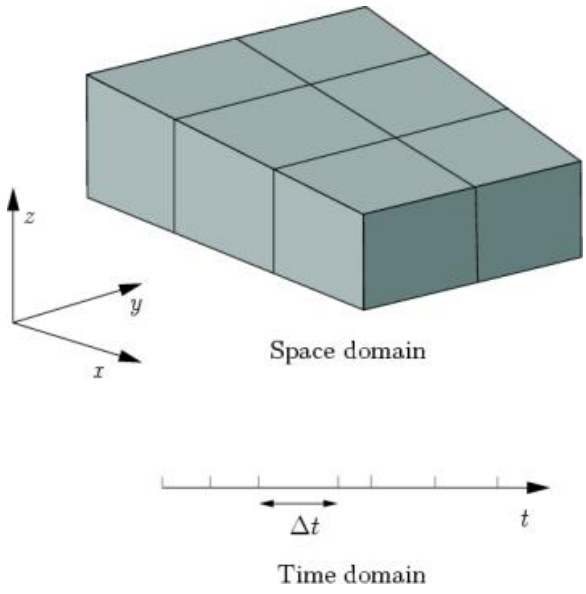

Figure 2.1.: Discretization of the Solution Domain [16]

2.2 Discretization of the Governing Equation

A generic transport equation can be considered to consist of a time derivative, convection, diffusion and a source term component. For any quantity ϕ, the transport equation is of the form,

$$\frac{\partial \rho\phi}{\partial t} + \nabla\cdot(\rho U\phi) - \nabla\cdot(\rho\Gamma_\phi\nabla\phi) = S_\phi(\phi) \tag{2.1}$$

Integrating this equation over the control volume for one time step gives us the equation,

$$\int_t^{t+\Delta t}\left[\frac{\partial}{\partial t}\int_{V_p}\rho\phi dV+\int_{V_p}\nabla\cdot(\rho U\phi)dV-\int_{V_p}\nabla\cdot(\rho\Gamma_\phi\nabla\phi)dV\right]dt = \int_t^{t+\Delta t}\left[\int_{V_p}S_\phi(\phi)dV\right]dt \tag{2.2}$$

This section focuses on discretizing each volume integral term of the finite volume equation into simple algebraic terms which can then be solved on the grid to get an approximate solution at each discrete point on the grid.

2.2.1 The Convection Term

The convection term is simplified by applying the Gauss theorem which gives,

$$\int_{V_p}\nabla\cdot(\rho U\phi)dV=\int_S dS\cdot(\rho U\phi)=\sum_f S\cdot(\rho U)_f\phi_f=\sum_f F\phi_f \tag{2.3}$$

The convection term in the generic transport equation has a divergence operator. Such terms are discretized in OpenFOAM by the Gauss Scheme similar to the equation above. The flux ϕ_f, which is $(\rho U)_f$ in the case of the convection term, is computed either directly if ϕ is defined as a surface field or is interpolated from the cell center values if it is defined as a volume field. Thus when specifying the divergence scheme which is to be used by OpenFOAM it is also necessary to define a suitable interpolation scheme. Some of the face interpolation schemes available will be discussed a few sections later. In the computations presented in this study the Gauss scheme is used with the limited linear interpolation scheme to limit the gradients.

2.2.2 Gradients

Though a gradient term is not explicitly present in the generic transport equation we have considered, it is necessary to look at how the term is handled due to the use of gradients in the diffusion component. Gradients are computed by three methods which can be either directly defined in the source code or can be selected at run time.

The three most common methods are the Gauss integration method, the least square method, and the surface normal gradient calculation. The Gauss scheme is used in this study with linear interpolation for the face gradients.

Gauss integration is applied on a gradient term integrated over the control volume by using the Gauss theorem thereby converting it to a summation over the faces of the control volume.

$$\int_{V_p} \nabla\phi dV = \int_S dS\phi = \sum_f S_f\phi_f \tag{2.4}$$

The surface normal gradient is the gradient of a quantity in the direction normal to the surface. It can be approximated as

$$\nabla\phi_f = \frac{\phi_N - \phi_P}{|d|} \tag{2.5}$$

Schemes for the surface normal gradient need to include orthogonal correction to improve the accuracy for non-orthogonal meshes. An explicit non-orthogonal correction technique is used in the calculation of the surface normal gradient here.

2.2.3 The Diffusion Term

The diffusion term is a typical example for a Laplacian term. Like in the case of the convection component, the Gauss scheme is the only option for discretization. The diffusion term is discretized as,

$$\int_{V_p} \nabla\cdot(\rho\Gamma_\phi\nabla\phi)dV = \sum_f S\cdot(\rho\Gamma_\phi\nabla\phi)_f = \sum_f(\rho\Gamma_\phi)_f S(\nabla\phi)_f \tag{2.6}$$

While mentioning the scheme for the diffusion term it is necessary to specify a face interpolation scheme as well as a scheme for the surface normal gradient. In the rare case that the mesh is orthogonal, the surface normal gradient can be treated as described in the previous section. In the case of non-orthogonal meshes additional care is needed as described a few sections later. Again, the Gauss scheme with linear

interpolation is used with explicit non-orthogonal correction for the surface normal gradient.

2.2.4 The Time Derivative

In the case of unsteady calculations, variations with time are also calculated and as a result the time derivative terms remain in the transport equation. The time derivative discretization scheme can be picked while defining the case.

Euler Implicit

The Euler implicit method is a simple first order backward differencing scheme. The Euler implicit method is mathematically given as,

$$\frac{\partial}{\partial t}\int_{V_p}\rho\phi dV = \frac{(\rho_P\phi_P V)^n - (\rho_P\phi_P V)^\circ}{\Delta t} \tag{2.7}$$

Here, n corresponds to the current time step and $\circ$ denotes the previous time step.

Backward Differencing

Backward differencing is similar to the Euler implicit scheme but is extended to include an extra time step. This makes it second order accurate.

$$\frac{\partial}{\partial t}\int_{V_p}\rho\phi dV = \frac{3(\rho_P\phi_P V)^n - 4(\rho_P\phi_P V)^\circ + (\rho_P\phi_P V)^{\circ\circ}}{2\Delta t} \tag{2.8}$$

The superscript $\circ\circ$ corresponds to two time steps before the current time. When dealing with second derivatives of time only the Euler implicit method is available. These implicit methods are unconditionally stable. The Euler implicit method is used in all computations presented later.

2.2.5 Source Terms

Source terms in transport equations play a vital role in the solution. Source terms are usually in the form of external forces, such as gravitational forces or surface tension forces in fluid mechanics. The source term has to be linearized as it affects the diagonal dominance of the sparse matrix while solving the discretized set of equations. The source term, assumed to be dependent on the flux, is linearized as,

$$S_\phi(\phi) = S_u + S_p\phi \tag{2.9}$$

Here, S_p and S_u could also be functions of the flux. This is substituted into the volume integral for the source term.

2.2.6 Temporal Discretization

The transport equation after the discretization of all the spatial and time derivatives is said to be in the semi discretized form.

$$\begin{aligned}\int_t^{t+\Delta t}\left[\left(\frac{\partial\rho\phi}{\partial t}\right)_P V_P + \sum_f F\phi_f - \sum_f(\rho\Gamma_\phi)_f S\cdot(\nabla\phi)_f\right]dt \\ = \int_t^{t+\Delta t}\Big(S_u V_P + S_P V_P \phi_P\Big)dt\end{aligned} \tag{2.10}$$

Following the notation used in [16], all the spatial terms can be grouped into a single term $A\phi$. The integral of this quantity over the control volume and time step gives,

$$\int_t^{t+\Delta t}\left[\int_V A\phi dV\right]dt = \int_t^{t+\Delta t} A^*\phi dt \tag{2.11}$$

where A^* denotes the spatial terms after discretization. In OpenFOAM the time integrals are handled with one of three methods.

Euler Implicit

The Euler implicit method is first order accurate, ensures boundedness and is unconditionally stable which makes it the most reliable method. Despite being only first order accurate this is most commonly used. In the Euler implicit method the the spatial terms take the values at current time.

$$\int_t^{t+\Delta t} A^*\phi dt = A^*\phi^n \Delta t \tag{2.12}$$

Euler Explicit

In this case the spatial terms take values from previous time. Again it is first order accurate, however this method is only conditionally stable. The stability criteria has been found to be,

$$Co = \frac{U \cdot d}{|d|^2 \Delta t} \tag{2.13}$$

where U is a characteristic velocity.

Crank Nicholson

This is the third method and is a blend of the implicit and the explicit methods. Based on the trapezoidal rule it uses an average between current and previous values. This method is unconditionally stable and is second order accurate but loses its boundedness.

$$\int_t^{t+\Delta t} A^*\phi dt = A^*\left(\frac{\phi^n + \phi^o}{2}\right)\Delta t \tag{2.14}$$

2.3 Face Interpolation Schemes

There are numerous schemes implemented for interpolating values from cell centers to face centers to calculate fluxes across the faces. We will limit our discussion in this chapter to a few basic schemes.

2.3.1 Central Differencing

The central differencing scheme assumes a polynomial fit between the values at the two cell centers. It is given as,

$$\phi_f = f_x \phi_P + (1 - f_x)\phi_N \tag{2.15}$$

Here, subscript P refers to values in the current cell while subscript N refers to values at the neighboring cell which shares the face. The factor f_x depends on the ratio of the distance between the face center and the neighboring cell and the distance between the two cell centers. This interpolation scheme is second order accurate but is not bounded.

2.3.2 Upwind Differencing

This method is dependent on the direction of flow. It is only first order accurate but is bounded. The value at the face is taken to be equal to the value at the previous cell. If we take $n-1$ to be the cell to the left of the current cell, n to be the current cell and $n+1$ to be the neighbor on the other side.

$$\phi_f = \begin{cases} \phi_n & \text{if flow is from n-1 to n+1,} \\ \phi_{n+1} & \text{if flow is from n+1 to n-1} \end{cases} \tag{2.16}$$

2.3.3 Blended Differencing

This type of interpolation scheme combines both the upwind and central differencing scheme. The advantage of this is that it maintains boundedness.

$$\phi_f = (1 - \varphi)(\phi_f)_{UD} + \varphi(\phi_f)_{CD} \tag{2.17}$$

φ is called the blending coefficient. This form of blended differencing is implemented as a Normalized Variable Diagram (NVD) scheme in the Gamma scheme. Higher order of curve fitting is also available with the cubic scheme which uses a cubic interpolation. More complex schemes such as Total Variation Diminishing schemes with the Van Leer or MUSCL limiter are also implemented in OpenFOAM. A more detailed description of these schemes can be found in [18].

2.4 Non-Orthogonality

A mesh is said to be orthogonal if the normal to the face surface is parallel to the line joining the cell centers. Unless special efforts and time are invested in order to generate an orthogonal mesh, care must be taken to include non orthogonality correction while solving the transport equations. This comes into play when calculating the surface normal gradients. In the case of non-orthogonal meshes the gradient calculation is split into two parts.

$$S\cdot(\nabla\phi)_f = \Delta\cdot(\nabla\phi)_f + k\cdot(\nabla\phi)_f \tag{2.18}$$

The first term in the equation is the orthogonal contribution while the other represents the non-orthogonal part. The two new vectors Δ and k are related as,

$$S = \Delta + k \tag{2.19}$$

Δ is chosen parallel to the vector d joining the centers of the two cells. This enables us to use the surface normal gradient formulation discussed earlier for the

orthogonal part. Following the discussion by Jasak [20] we will focus on three possible decomposition methods.

2.4.1 Minimum Correction Approach

The minimum correction approach tries to keep the non orthogonal component as small as possible. This would help increase the diagonal dominance of the solution matrix. This is achieved by making Δ and k perpendicular to each other.

$$\Delta = \frac{d \cdot S}{d \cdot d} d \tag{2.20}$$

2.4.2 Orthogonal Correction Approach

This approach tries to keep the contribution from the parent as well as the neighboring cells the same as on an orthogonal mesh.

$$\Delta = \frac{d}{|d|} |S| \tag{2.21}$$

2.4.3 Over-relaxed Approach

The importance of the contribution in the values from the two cells increases with increase in non-orthogonality. The performance of the three methods were compared by Jasak [20] and it was concluded that the over relaxed approach performed best even for non-orthogonality angles of 65°.

$$\Delta = \frac{d}{d \cdot S} |S|^2 \tag{2.22}$$

The use of finite volume methods on non orthogonal meshes have been discussed in much detail by Norris [22]. It is important to note that though there are ways to increase the diagonal dominance of the matrix, the non-orthogonal component

has to be completely eliminated in order to maintain boundedness. The over-relaxed approach has been implemented in OpenFOAM for non-orthogonal correction.

2.5 Boundary Conditions

Boundary conditions are necessary to solve a set of equations as they provide a starting point for the solution. Boundary conditions in the broad sense are of three main types.

2.5.1 Fixed Value Boundary Condition

The fixed value boundary condition is also referred to as the Dirichlet boundary condition. In this method the value of the variable at the boundary is specified. In the case of the convection term which is discretized the value at the boundary face can be directly used in the summation over faces.

For the diffusion term as discussed earlier the surface normal gradient is required. This is calculated from the known values of the field at the boundary face and the cell centers.

$$S\cdot(\nabla\phi)_b = |S|\frac{\phi_b - \phi_P}{|d_n|} \tag{2.23}$$

This can be plugged back into the diffusion term. Examples of the boundary conditions derived from the fixedValue type implemented in OpenFOAM include totalPressure, pressureInletVelocity etc.

2.5.2 Fixed Gradient Boundary Condition

The fixed gradient boundary condition specifies a value for the gradient normal to the boundary. This type is also known as the von Neumann type.

$$\left(\frac{S}{|S|}\cdot\nabla\phi\right)_b = g_b \tag{2.24}$$

When handling convection terms the value at the boundary has to be computed from the known value at the cell center and the given gradient at the boundary.

$$\phi_b = \phi_P + d_n \cdot (\nabla\phi) = \phi_P + |d_n| g_b \tag{2.25}$$

The diffusion term can now use the given gradient directly. However some correction will be needed in the case of non orthogonal cells. A fixed gradient can be directly specified along with the value of the gradient. Numerous other boundary types derived from the fixed gradient type are also implemented in OpenFOAM (eg. buoyantPressure). A special type of the fixed gradient boundary condition is the zeroGradient type which simply defines the gradient at the boundary to be zero.

2.5.3 Mixed Boundary Condition

OpenFOAM also has allowance to build boundary conditions which could be a combination of the fixed value and fixed gradient types. This type is dependent on a parameter defined as the value fraction which gives the extent to which the two are combined. If the value fraction is 1 it becomes a fixed value type boundary condition and when it is 0 it simplifies to a fixed gradient type. An example of a boundary condition derived from the mixed type is the inletOutlet boundary condition. If the reference gradient, the reference value and the value fraction are given by g_{ref}, ϕ_{ref} and f_x respectively we have,

$$\phi_b = f_x \phi_{ref} + (1 - f_x) g_{ref} \tag{2.26}$$

These three basic types form the basic blocks for a large library of boundary conditions. These can be studied from their respective source codes. Physical boundaries such as inlet, outlet, wall, symmetry, etc. are all specified with the help of these types.

2.6 Solution Procedure

The discretized transport equation now becomes a system of algebraic equations where each equation is centered around one control volume. In a general sense this can be written as,

$$a_P \phi_P^n + \sum_N a_N \phi_N^n = R_P \tag{2.27}$$

The values of the variables for a cell are dependent on the neighboring cells and also has a source term contribution, R_P. This system of linear equations can be written in matrix form as,

$$[A][\phi] = [R] \tag{2.28}$$

where A is the square matrix with all the coefficients a_P and a_N. This matrix A is generally a sparse matrix as the value at a particular cell is affected only by a few immediately neighboring cells depending on the order of accuracy of our discretization schemes. The vector $[\phi]$ contains all the variables and $[R]$ has all the source contributions. Based on the discretization of the transport equation each term of the transport equation contributes both to the matrix A as well as R. Those terms which are treated implicitly add up to the coefficients of A and those terms which have an explicit treatment are treated as source terms. OpenFOAM makes use of iterative methods to compute the solution of this system of equations. The biggest challenge with iterative methods is the need to maintain diagonal dominance. This can be achieved by careful handling of implicit and explicit terms or by using the under relaxation technique. The discussion on how each term of the transport equation affects the diagonal dominance of the matrix can be found in [17]. Here, the focus would be on the different solution methods available as part of OpenFOAM.

The solvers for each of the discretized equations are mentioned in the fvSolutions file in the case directory. The various solvers available are Preconditioned (bi-) conjugate gradient (PCG/PBi-CG), solver using a smoother (smoothSolver), gener-

alized geometric-algebraic multi grid (GAMG) and the diagonal solver for explicit systems. The PCG solver is only for symmetric matrices while we can use PBi-CG for asymmetric matrices. A pre-conditioner is used to improve the convergence rate of the solver. The pre-conditioner tries to reduce the condition number of the matrix A. The solution is quickest and its accuracy is highest when the condition number is close to 1. Diagonal incomplete Cholesky (DIC), Diagonal incomplete LU and GAMG are a few of the pre-conditioners available in OpenFOAM.

Another class of solvers used are smooth solvers. The Gauss Seidel is an example of a smooth solver available. The DIC can also be used with a smoother. GAMG which has been used both as a solver and a pre-conditioner is generally used to speed up the computation. It first computes a solution on a coarse grid and then uses that solution as an initial guess for the finer mesh. This study makes use of the PCG solver with the GAMG pre-conditioner for solving the pressure equations and the smooth Gauss Seidel solver for the momentum and VOF equation described later in Chapter 3.

3. TWO PHASE FLOW ALGORITHMS AND interFoam

In the case of two phase flows where there is an abrupt change in fluid or flow properties across a thin region called the interface it becomes necessary to have additional algorithms to describe the interface and the changes across it. There are two main approaches to characterize the interface in multiphase flows viz., the interface tracking and the interface capturing approaches. The interface tracking approach includes the Boundary Integral Method, Volume of Fluid (VOF), Front Tracking Algorithm, Immersed boundary methods, etc. In interface capturing algorithms such as the Level Set Method and the Phase Field Methods the interface is captured by means of a specific function.

While solving the Navier-Stokes Equations there arises a jump in the normal stress across the interface which is balanced by the surface tension. This can be written in terms of the surface pressure which is governed by the Young Laplace Equation.

$$p_s = p_2 - p_1 = \sigma\kappa \tag{3.1}$$

Here p_s is the surface pressure, p_α is the pressure in fluid $\alpha = 1$ or 2, σ is the surface tension, and κ is the local surface curvature. κ is given as $R_1^{-1} + R_2^{-1}$ where R_1 and R_2 are the principal radii of curvature of the surface. The Young Laplace equation can be solved at the exact boundary but there are certain issues such as the fact that we do not know explicitly the exact position and shape of the interface. To circumvent this issue Brackbill et al. [23] proposed the Continuum Surface Force (CSF) model. According to this model surface tension is considered as a three dimensional effect across an interface which is typically smoothed and diffused rather than as a boundary condition on a sharp interface. They argued that since the interface is now diffuse and since surface tension acts everywhere within the transition region it can be represented

by a volume force which gives the actual surface tension per unit interfacial area as the thickness of the interface tends to zero. This volume force is also localized such that it is zero outside the interface region. Now this volume force representing the surface tension can be added to the Navier-Stokes Equation which for an inviscid fluid becomes,

$$\rho \frac{dU}{dt} = -\nabla p + F_{sv} \tag{3.2}$$

where ρ is the density, U is the velocity and p is the pressure. They also showed that for an interface with finite thickness the volume force, $F_{sv}(x)$ is given as,

$$F_{sv}(x) = \sigma \kappa(x) \frac{\nabla \tilde{c}(x)}{[c]} \tag{3.3}$$

where σ is the surface tension coefficient, κ is the local surface curvature and $\widetilde{c}(x)$ is the smoothened color function and [c] is the jump in the color, i.e., $[c] = c_2 - c_1$. The function c is any function which has two distinct values in the two fluids and changes smoothly from c_1 to c_2 in the transition region. The interface is assumed to be given by the iso-surface at $\frac{1}{2}(c_1 + c_2)$.

3.1 Boundary Integral Method

The boundary integral methods are usually applied to simpler flows such as Stokes Flow which are inviscid and incompressible. Hou et al. [24] applied the boundary integral method to study the effect of surface tension on the Kelvin-Helmholtz and Rayleigh-Taylor instabilities. Boundary Integral Methods are much more difficult to apply for general flows which are governed by a more complicated equation such as the Navier-Stokes Equation. In situations where the Boundary Integral Method can be applied it has been seen that the accuracy and efficiency of this method is much better than any other method used for interface calculation. Thus this method is often used as a benchmark for calculating the accuracy of other methods such as the VOF method. The general form of the Boundary Integral Equation is given as

$$c(\xi)\phi(\xi) = \int_S \left(\phi^*(\xi, y) \frac{\partial \phi(y)}{\partial n_y} - \phi(y) \frac{\partial \phi^*(\xi, y)}{\partial n_y} \right) dS_y \tag{3.4}$$

By using the boundary integral method the solution for the entire domain can be computed from data for the interface which in turn means that it is not needed to discretize the whole domain but to just discretize the boundary. The method also reduces the dimension of the problem by one as now the fields are computed from values on the interface only. Though great strides have been made in using Boundary Integral Methods for 2-dimensional problems its use in 3-dimensional cases is still under research. Due to the presence of integrals in the formulation highly efficient and accurate quadratures are needed to calculate these integrals. Since the current study uses only the VOF method for tracking the interface the Boundary Integral Method will not be further discussed in this chapter. The application of this method for various problems in fluid mechanics have been shown by Power and Wrobel [25] and in the references mentioned by Hou et al. [24].

3.2 Front Tracking Method

The front tracking method makes use of two separate grids, a background stationary finite difference grid which is used to compute the flow properties for the whole domain and a moving interface grid which is used to track the interface. In 2-D computations the interface grid is just a bunch of Lagrangian points which are usually connected by means of straight lines. Other higher order curves may also be used to connect these points. The accuracy of the interface topology depends on the number of points used to define the interface and also the order of accuracy of the lines used to join them. It has been seen that this method works well in less refined grids and also unlike in the case of VOF grid alignment does not have much effect on the solution.

The points on the interface mesh are logically connected and each cell and its neighbors are continuously tracked. The main reason for this is to deal with break

up or combination of interfaces which often occurs in cases such as two droplets combining or in computations of boiling. This means that the interface mesh has to be cut and patched up based on the situation at each time step. This form of tracking the interface elements becomes very cumbersome when dealing with 3-D interfaces. A simpler form of the front tracking method for 3-D interfaces was suggested by Shin and Juric [26] where the continuous tracking of the cells and its neighbors is replaced by an interface reconstruction technique. The first step in the front tracking method once the two grids are defined is the advection of the marker particles on the interface mesh. In the absence of phase change these marker particles move with the velocity of the fluid which can be got by bilinear interpolation to find the velocity of each interface element. If the points on the interface grid move too far apart the points are usually redistributed to maintain accuracy. The next step is to calculate the source term in the momentum equation due to the surface tension force. The surface tension force is given as,

$$F_{sv}(x,t) = \int_{\Gamma(t)} \sigma \kappa_f \delta(x - x_f(s)) n_f ds \tag{3.5}$$

where the curvature κ and the normals are calculated on the interface. This information which is property of the interface then has to be transferred to the fixed background grid so that it can be added to the momentum equation while calculating the properties. This transfer of information from one grid to another is done with Peskins immersed boundary method [27]. Following [26] this can be written as,

$$F_{ij}(x) = \sum_k f_k \delta(x - x_{f,k}) \Delta s_k \tag{3.6}$$

where Δs is the elemental length in 2D or area in 3D. The dirac delta function is typically taken to be the one recommended by Peskin and McQueen [28]. Using the Frenet relation the surface tension force for each segment is then given as,

$$f_k = \int_A^B \sigma \kappa_f n_f ds = \int_A^B \sigma \frac{\partial t_f}{\partial s} ds = \sigma(t_B - t_A) \tag{3.7}$$

Here t_f is the tangent vector of the endpoints of each element. If the fluid properties between the two phases in question are largely different which is mostly the case (e.g. water/air systems) an additional parameter called the indicator function is introduced. This indicator function is similar to the color function in Brackbill's [23] CSF or the height function. This indicator function is calculated by solving the Poisson equation [26].

$$\nabla^2 I = \nabla \cdot \int_{\Gamma(t)} n\delta(x - x_f) ds \tag{3.8}$$

This method has been implemented and discussed in detail for computing boiling flows by Tryggvason and Juric [29] in 2D and Shin and Juric [26] in 3D.

3.3 Level Set Method

The level set method is a very common interface capturing method. Unlike in the case of the front tracking method there are no massless markers which are logically connected and move about with the interface. The method was first proposed by Osher and Sethian [30] and relies on representing the interface as the zero level of a higher dimensional function. The level set function used in the case of most fluid mechanics problems is,

$$\beta(x,t) \begin{cases} > 0 & \text{if } x \in \text{fluid 1} \\ = 0 & \text{if } x \in \Gamma \text{ (interface)} \\ < 0 & \text{if } x \in \text{fluid 2} \end{cases} \tag{3.9}$$

And this function β is set as the signed distance function to the interface. The evolution of the level set function is then governed by

$$\beta_t + U \cdot \nabla \beta = 0 \tag{3.10}$$

The level set method is advantageous because it is much easier to implement and can be used for 2D and 3D interfaces with minimal effort. The level set method also

deals with topological changes such as splitting of a droplet as the interface is now embedded in the function and there is no local surgery required at the interface. The main disadvantage with the level set method is its inability to conserve mass. After the initialization of the interface it is likely that ϕ would not remain a signed distance function. The interface is thus often reinitialized to the signed distance function while retaining the zero level which denotes the interface.

It is also important to note that the normal vector and the curvature which are needed to calculate the surface tension force can be directly calculated from the level set function as,

$$n = \frac{\nabla\beta}{|\nabla\beta|} \qquad ; \qquad \kappa = \nabla\cdot\frac{\nabla\beta}{|\nabla\beta|} \tag{3.11}$$

The density and viscosity in the two fluids are a constant value and depend on the sign of the level set function.

$$\begin{aligned} \rho(\beta) &= \rho_2 + (\rho_1 - \rho_2)H_\epsilon(\beta) \\ \nu(\beta) &= \nu_2 + (\nu_1 - \nu_2)H_\epsilon(\beta) \end{aligned} \tag{3.12}$$

The Heaviside function $H(\phi)$ is given as,

$$H_\epsilon(\beta) = \begin{cases} 0 & \text{if } \beta < -\epsilon \\ \frac{1}{2}\Big[1 + \frac{\beta}{\epsilon} + \frac{1}{\pi}\sin(\pi\beta/\epsilon)\Big] & \text{if } |\beta| \leq \epsilon \\ 1 & \text{if } \beta > \epsilon \end{cases} \tag{3.13}$$

This Heaviside function is for an interface of thickness $\frac{2\epsilon}{|\nabla\beta|}$. The level set function is reviewed in further detail by Sethian and Smereka [31].

3.4 Phase Field Method

The phase field method is based on the idea that the sharp fluid interface is now diffuse and instead of a jump in the fluid properties across the interface the sudden jump is now smoothened across the interface. It makes use of a conserved field

parameter called the order parameter which could be the mass concentration of the phases. The order parameter is a constant in the two bulk phases but varies in the interfacial regions.

$$\phi = \frac{m_1 - m_2}{m_1 + m_2}, \qquad c = \frac{m_1}{m_1 + m_2} \tag{3.14}$$

In this method the Navier-Stokes equations for the two fluids are solved along with the Cahn-Hillard equation for the mass concentration.

$$\frac{\partial c}{\partial t} + U \cdot \nabla c = \nabla \cdot (M(c) \nabla \mu) \tag{3.15}$$

$$\mu = F'(c) - \epsilon^2 \Delta c \tag{3.16}$$

Here $M(c) = c(1-c)$ is the mobility and ϵ is the interface thickness. The function F is called the Helmholtz free energy and is given as $F(c) = \frac{1}{4}c^2(1-c)^2$. The surface tension force in the momentum equation now depends on the phase field and is given as

$$F_{sv} = -6\sqrt{2}\epsilon \sum_{i=1}^{3} \sigma_i \nabla \cdot (\nabla c_i \otimes \nabla c_i) \tag{3.17}$$

This is one of the formulations for the surface tension force. Other forms have been used in various cases and is shown in Kim [32]. The density and viscosity as expected is dependent on the phase field parameter (mass concentration in this case) and can be given as just a linear interpolation based on the values of the two fields. Other definitions of the order parameter have also been studied. Recent reviews on the application of the phase-field methods in fluid problems can be found at [32] and [33].

The phase-field method like the level set method can handle topological changes very well and can be applied to systems with more than two fluids [32]. It could however be computationally expensive owing to the length scales associated with the interface thickness.

3.5 Volume of Fluid Method

The volume of fluid method was proposed by Hirt and Nichols [34]. The VOF method uses the concept of volume fraction which in many ways is similar to the indicator function. The volume fraction in a gas liquid system is essentially the ratio of the volume of a liquid (usually the denser liquid) in the cell to the volume of the cell. If the volume fraction is 1 then the cell is completely filled with the denser liquid and if it is 0 the cell is completely filled with the other fluid. The volume fraction value in the interfacial cells is between 0 and 1. The volume of fluid method basically is split into two steps. The first step is the interface reconstruction step. In this step the interface is explicitly reconstructed from the volume fraction field. One of the earliest algorithms used for reconstruction was the SLIC (Simple Line Interface Calculation). In the 2D case this method represents the interface with lines parallel to one of the coordinate axes. More recently a better reconstruction technique called PLIC (Piecewise Linear Interface Calculation) is being used. Here the interface is still made up of straight lines but instead of being parallel to the coordinate axes these lines are now perpendicular to the normal vector at the interface. The interface normal vector is computed from the volume fraction gradient in the cell.

The volume of fluid method has glaring issues in calculating the surface tension force which leads to spurious currents at the interface. Using an interface reconstruction technique which is of a higher accuracy would help reduce these errors. There have been various alternate interface reconstruction techniques which have been studied. Some of them are LVIRA [35] (Least-Squares Volume of Fluid Interface Reconstruction Algorithm), PROST [36] (Parabolic Reconstruction of Surface Tension) and CLSVOF [37] (Combined Level Set and Volume of Fluid). PROST uses a parabolic reconstruction which increases the accuracy.

The second step in the volume of fluid method is the advection, or interface propagation, step. Once the interface has been explicitly reconstructed it should then

be moved based on the velocity data which were computed. The interface advection is governed by,

$$\frac{\partial \alpha}{\partial t} + \nabla \cdot (U\alpha) = 0 \tag{3.18}$$

This equation is discretized and commonly solved by applying the operator split approach. The main advantage with the volume of fluid method is its inherent property of mass conservation. The surface tension force is still calculated using Brackbill's CSF formulation.

The CLSVOF method tries to use the advantages of both the VOF and the level set methods. The VOF method conserves mass which is not possible in the level set method and the Level Set method does a better job at calculating the curvature and the interface normal vectors as the interface is modelled as a continuous function. This gives a more accurate calculation of the surface tension force and greatly reduces the parasitic currents induced at the interface. The CLSVOF method has been discussed in further detail along with a comparison between the VOF, CLSVOF, and other Level Set Methods by Gerlach et al. [38] and Wang et al. [39].

3.6 interFoam

interFoam is a multiphase solver for incompressible, isothermal immiscible liquids. It was implemented in its original form based on the work of Ubbink [40]. interFoam employs the volume of fluid method for tracking the interface between the two fluids. The location of the two fluids is tracked by means of the volume fraction function (α).

$$\alpha = \begin{cases} 1 & \text{for fluid 1} \\ 0 & \text{for fluid 2} \\ 0 < \alpha < 1 & \text{interface} \end{cases} \tag{3.19}$$

This solver solves the volume fraction advection equation part of the VOF method along with the Navier-Stokes equations within the PIMPLE loop. These equations are given as,

$$\nabla \cdot U = 0 \tag{3.20}$$

$$\frac{\partial \alpha}{\partial t} + \nabla \cdot (U\alpha) = 0 \tag{3.21}$$

$$\frac{\partial (\rho U)}{\partial t} + \nabla \cdot (\rho U U) = -\nabla p + \nabla \cdot T + \rho f_b \tag{3.22}$$

In the equations above U is the velocity, T is the deviatoric viscous stress tensor, p is the pressure and f_b are the body forces per unit mass. It is important to note that the velocity field is common for both the phases. The use of a single velocity field does not tell us the velocity contribution of each phase at the interface. The fluid properties are calculated as in the case of a mixture, as a weighted average depending on the value of the volume fraction in the cell,

$$\rho = \rho_1 \alpha + \rho_2 (1 - \alpha) \tag{3.23}$$

$$\mu = \mu_1 \alpha + \mu_2 (1 - \alpha) \tag{3.24}$$

where μ_i and ρ_i correspond to viscosity and density for fluid i. The external forces generally include the force due to gravity and the force due to surface tension. The surface tension force is calculated based on Brackbill's CSF formulation. The curvature and surface normal required for calculating the surface tension force are calculated from the gradients of the volume fraction function. The interface extends over a few grid cells. The volume of fluid method is based on the assumption that the interface is computed at a DNS level. This assumes that the interface thickness is very small and the relative velocity across the interface between the two phases is zero. But in most cases we deal with diffuse interfaces and hence an additional term is included in the volume fraction advection equation to compress the interface [21].

$$\frac{\partial \alpha}{\partial t} + \nabla \cdot (\alpha \bar{U}) + \nabla \cdot [U_r \alpha (1 - \alpha)] = 0 \tag{3.25}$$

$\bar{U}$ is the average velocity of the two phases equal to $\alpha U_1 + (1-\alpha)U_2$ and U_r is the relative velocity at the interface equal to $U_1 - U_2$. This additional convective term is non-zero only at the interface. The alpha equation is solved by means of the MULES (Multi-Dimensional Universal Limiter with Explicit Solution) solver. The MULES algorithm ensures that the solution is bounded and stable but in its explicit formulation is limited by a very strict Courant number limit. In the latest implementation of OpenFOAM the MULES solver has been improved to include a semi-implicit treatment. In the semi implicit form first an implicit predictor step is run using schemes which ensure a bounded solution (e.g. Euler implicit for time and Upwind for space). This step is followed by an explicit correction step with the MULES limiter. This removes the limitation on the Courant number and reduces the computation times greatly.

Let us now look at how the volume fraction advection equation is discretized and a way to calculate the relative velocity at the interface. The advection equation in its discretized form is written as,

$$\frac{\partial \alpha}{\partial t} + \sum_f (\alpha \bar{U})_f \cdot S_f + \sum_f [\alpha(1-\alpha)U_r]_f \cdot S_f = 0 \tag{3.26}$$

This can then be written in terms of two fluxes as given in Marquez's work [41], the first term written in terms of the center of volume velocity flux and the second term as the compressive velocity flux. The relative velocity U_r is also known as compressive velocity. This velocity is not calculated directly but is computed in terms of the flux as,

$$\phi_r = n_f \min\left[C_\alpha \frac{|\phi|}{|S_f|}, \max\left(\frac{|\phi|}{|S_f|}\right)\right] \tag{3.27}$$

Here the constant C_α is provided by the user and determines the extent of interface compression. $C_\alpha = 1$ implies optimal interface compression while $C_\alpha = 0$ means there is no interface compression. The value of C_α can also be greater than 1 for higher

levels of interface compression but there are some stability issues for higher values. ϕ is the face volume flux, n_f is the face unit normal flux calculated as,

$$n_f = \frac{(\nabla\alpha)_f}{|(\nabla\alpha)_f + \delta_n|} \cdot S_f \tag{3.28}$$

For δ_n as a stabilization factor in the equation to prevent division by zero.

$$\delta_n = \frac{\epsilon}{\left(\frac{\sum_N V_i}{N}\right)^{\frac{1}{3}}} \tag{3.29}$$

V_i is the volume of control volume i and ϵ is usually a very small value and it is taken to be 10^{-8} in OpenFOAM.

An additional modified pressure field called p_{rgh} is used in interFoam to remove the hydrostatic component of pressure while calculating gradients. This also helps in specifying boundary conditions at the domain boundaries. Since in this study we are dealing with zero gravity the two pressure fields are the same.

$$p_{rgh} = p - \rho g h \tag{3.30}$$

There is no direct pressure equation in the set of governing equations mentioned earlier. Thus the pressure has to be calculated by a derived pressure equation. OpenFOAM uses the PIMPLE algorithm to compute pressure. The PIMPLE algorithm is a combination of the PISO (Pressure implicit with splitting of operator) and SIMPLE (Semi-implicit method for pressure linked equations) algorithms. The PISO algorithm is a pressure velocity coupling method which was proposed by Issa [42] and has been discussed in [18, 21, 41, 43] and a lot of other texts. This algorithm is the most commonly used method to solve for the pressure field when using the Navier-Stokes equations. It solves the discretized form of the pressure Poisson equation using a predictor corrector approach. The momentum equation is first solved with an approximate initial guess for the pressure gradient (predictor step) and these velocities are used to solve the pressure poisson equation to get the pressure. This pressure

is now used to correct the velocities explicitly (corrector step) and the procedure is repeated.

$$\nabla\cdot\left[[a_p]^{-1}\nabla p_f\right] = \nabla\cdot\left[[a_p]^{-1}[H(u) - g\cdot x\nabla\rho + \sigma\kappa\nabla\alpha]_f\right] \tag{3.31}$$

a_p refers to the diagonal terms to the coefficient matrix A, $H(u)$ corresponds to the non diagonal matrix coefficients for the neighboring cells multiplied by their corresponding velocities. $H(u)$ also includes the source term contributions other than those due to gravity and surface tension. The PISO algorithm however has a strict limit on the maximum time step size owing to stability issues. The PIMPLE algorithm uses the same formulation for the pressure equation as the PISO algorithm but uses additional under relaxation on the variables which helps in increasing the time step size. In addition to this the PIMPLE algorithm also has allowance to compute the pressure - velocity coupling multiple number of times for a single time step. These algorithms have been discussed in considerable detail in the references mentioned above and can also be comprehended from the solver source code.

The solver can make use of adaptive time stepping to ensure that it adheres to the Courant number limitation and a stable converged solution is obtained. Instead of defining a fixed time step by which the solution advances each step a few parameters such as the maximum courant number and the maximum time step are defined in the case directory. The time step is then calculated in situ by the equation,

$$\Delta t^n = \min\left\{\frac{Co_{\max}}{Co^o}\Delta t^o; \left(1 + \lambda_1\frac{Co_{\max}}{Co^o}\right)\Delta t^o; \lambda_2\Delta t^o; \Delta t_{\max}\right\} \tag{3.32}$$

Co^o is the maximum local courant number which is calculated from previous values of velocity and time step. λ_1 and λ_2 are damping factors which limit the maximum change in time step size. Usually the ratio between two consecutive time steps is limited to 1.2.

Another procedure incorporated to ensure stability and convergence of the solution is subcycling within a single time step while solving the volume fraction equation. This essentially solves the volume fraction advection equation multiple times within a

single time step using intermediate time steps. This is defined by the nAlphaSubCycles keyword in the case definition. The flux is computed at the end of each subcycle and the total flux over the total time step is just a weighted sum of the fluxes from the subcycles.

$$\Delta t_{sc} = \frac{\Delta t}{n_{sc}} \tag{3.33}$$

$$\phi = \sum_{i=1}^{n_{sc}} \frac{\Delta t_{sc}}{\Delta t} \phi_{sc,i} \tag{3.34}$$

where Δt is the global time step size, n_{sc} is the number of subcycles, Δt_{sc} is the time step size for each intermediate step in the subcycling process and $\phi_{sc,i}$ is the individual face flux corresponding to a subcycle time step.

3.7 Parasitic Currents

A discussion of the interFoam solver or any other solver which employs the Volume of Fluid method would be incomplete without a section on parasitic currents. The surface tension force is calculated using the CSF formulation where the curvature is computed from the gradients of the volume fraction function. The volume fraction function is discontinuous and this leads to an inconsistent force calculation. The surface tension force is not necessarily properly balanced by the pressure. Parasitic currents are a result of this. Parasitic currents are circulating vortex like structures which are formed close to the interface without any external forcing. This is much more pronounced in cases where the density between the two fluids is very high. The velocities associated with these spurious currents around a bubble was estimated by Lafaurie et al. [44] to be $0.01\sigma/\mu$ where σ is the surface tension coefficient and μ is the viscosity of the fluid. These high velocity currents might distort the interface or even cause breakup of the interface.

There have been numerous attempts to reduce these spurious currents. Gerlach et al. [38] found that using a parabolic reconstruction method for the force calculation

reduced the parasitic currents by two orders of magnitude. They found that the PROST method [36] had least magnitude of parasitic currents followed by CLSVOF [37]. Jamet et al. [45] studied the use of second-gradient models for surface tension. They argued that the parasitic currents are related to energy conservation and were completely eliminated in their study. Shin and Juric [26] showed that their method also generated lesser spurious velocities in comparison to the VOF method and is comparable to previous work by Popinet and Zaleski [46]. The problem of parasitic currents has been present from the beginning and two of the simplest methods to reduce it have been to introduce better force balancing methods at the interface and improving the curvature calculation. In this study parasitic currents are present close to the interface and are $\mathcal{O}(10^{-1})$. However they do not seem to produce any major disturbance on the free surface and often the only effect seems to be the movement of the droplet along the cylinder walls due to the pressure imbalance which in the case of transitions cause stretching of the free surface when the contact line reaches the inlet patches. The energies do not seem to be affected in most cases and are comparable to values from Surface Evolver. Hence no special efforts have been made to eradicate these vortices at this stage. Further discussions related to parasitic currents can be found in [47–49] and the references mentioned in them.

4. PROBLEM FORMULATION

4.1 Problem Description

In this study we look at the transitions between different capillary stable states in a cylindrical capillary tube. The geometry in consideration is a simple cylindrical tube of radius $R_T = 1$. The length of the tube is fixed depending on the volume of the liquid. For very low contact angles at higher volumes a longer tube ($h = 6$) is necessary as the liquid spreads over a much larger area of the wall. In most other cases a shorter tube ($h = 5$) is used. There are three possible static equilibrium solutions in the case of a straight circular cylinder as discussed in earlier chapters. This means that there are six possible transitions between the three states. Here only the transitions from a droplet to plug and from a plug to a droplet are considered as the annulus is a rather small region compared to the plug and the droplet.

When looking at droplet to plug transitions, it is expected that the transition occurs either where the droplet becomes the higher energy solution or at the maximum volume of existence limit for the droplet. It is actually seen that transitions occur close to the maximum volume of existence line. The reverse transition occurs close to the minimum plug volume line. The transitions between the stable static states can be activated in two ways. In the first method the contact angle can be varied keeping the volume constant. In the stability chart (Figure 1.4), at a particular volume the solution follows the constant volume line (vertical lines) as the contact angle changes and the transition occurs close to when it crosses the corresponding volume limit line. The second method of studying these transitions is by keeping the contact angle constant and increasing or decreasing the volume. In this case the solution follows the constant contact angle lines (horizontal lines) in the stability chart (Figure 1.4).

The volume is varied to force the transitions to occur in this study. This can be easily achieved by having an inlet on the cylinder wall and using it to either inject or withdraw liquid from the domain. For this purpose, two inlet patches are defined on the wall of the cylinder centered at $(x, y, z) = (0, 1, h/2)$ and $(x, y, z) = (0, -1, h/2)$. The inlets are square in shape, as it is easier to build the grid around the inlet and generate a uniform mesh than with circular inlets. The squares are 0.2mm by 0.2mm in size. The properties of the two liquids used are $\rho_1 = 1000kg/m^3$, $\nu_1 = 1\times10^{-6}m^2/s$, $\rho_2 = 1kg/m^3$, and $\nu_2 = 1.48 \times 10^{-5}m^2/s$. The subscripts 1 and 2 refer to fluid 1 and fluid 2, respectively. We are interested in the topology formed by the denser fluid. The contact angle is measured inside this fluid.

In the case of transitions from droplet to plug, the denser fluid is added to the initial droplet volume through the fixed inlet boundary, with a total constant flow rate of $4\times10^{-9}m^3/s$. For the reverse transition, liquid is removed from the domain through the fixed flow rate boundaries at a similar flow rate. We look at a non-dimensional number relating the volume flow rate, the time step size, and the transition volume to compare the liquid flow rate relative to the volume scales. This would tell us if the volume flow rate used is too high for this type of calculation. This non-dimensional number is given as $\dot{V}\Delta t/V_{tr}$ where $\dot{V}$ is the flow rate, Δt is the time step size, and V_{tr} is the transition volume. For the case of the plug to droplet transition at a contact angle of 60°, we find this non-dimensional number to be 3.05×10^{-6} and for a droplet to plug transition at the same contact angle the non-dimensional number is 2.23×10^{-6}. These are very small numbers, and hence the volume flow rate used should not affect the transitions much. The removal or addition of fluid is stopped as soon as the fluid volume begins to change its topology. The volumes and surface areas needed for the energy calculation are obtained from the alpha field and its gradients.

The transitions are observed for a range of contact angles (θ) from 10° to 170°. The initial volumes differ for each contact angle and are mentioned in the discussion later. The initial alpha field for the plug to droplet transitions is defined based on the radius of curvature of the interface ($R_c = R_T/\cos\theta$) and is defined using addi-

tion and subtraction of cylindrical and spherical volumes. For the reverse transition from a droplet to plug, the initial droplet volume is defined as a spherical volume in contact with the wall of the cylinder, and is allowed to change topologies due to the contact angle boundary condition at the wall and settle to an equilibrium topology. The duality in solution as described in earlier sections still holds when looking at transitions.

4.2 Energy Minimization

Following the discussion by Langbein [50] the total energy of the two phase system is a combination of the surface, potential and kinetic energies.

$$E = \sigma A + E_{pot} + E_{kin} \tag{4.1}$$

The potential energy is the contribution due to gravity and the kinetic energy may be either due to rotation or in the case of transitions, due to the break up of the interface. Since this study focuses on zero gravity liquid surfaces there is no potential energy contribution to the total energy. It is also assumed that since the initial and the final equilibrium states are static we can neglect the kinetic energy. This is however an assumption as there will be velocities during the transition phase when the liquid topology breaks up and changes to a different state. Neglecting the potential and kinetic energies, now the total energy is the summation of the individual surface energies due to the three different surface interactions viz. liquid and solid, gas and solid, and liquid and gas in our case.

$$E = E_{FS} + E_{dryS} + E_{wetS} \tag{4.2}$$

The wetted and the dry energies are written as the product of their respective surface energy densities and areas. The Young boundary condition, which relates energy densities to contact angle, $\sigma \cos\theta = \sigma_{dryS} - \sigma_{wetS}$, is then applied to this equation.

$$E = \sigma A_{FS} + \sigma_{wetS} A_{wetS} + \sigma_{dryS} A_{dryS} \tag{4.3}$$

$$E = \sigma A_{FS} + (\sigma_{dryS} - \sigma \cos\theta) A_{wetS} + \sigma_{dryS} A_{dryS} \tag{4.4}$$

$$E = \sigma A_{FS} - A_{wetS} \sigma \cos\theta + \sigma_{dryS} (A_{wetS} + A_{dryS}) \tag{4.5}$$

The second term on the right can be further simplified as the sum of the two areas is simply the area of the entire wall of the cylinder, i.e., $A_{cylinder} = A_{wetS} + A_{dryS}$. This is a constant depending on the length of the cylinder and adds a constant contribution to the total energy.

$$E = \sigma (A_{FS} - A_{wetS} \cos\theta) + \sigma_{dryS} A_{cylinder} \tag{4.6}$$

$$E = \sigma (A_{FS} - A_{wetS} \cos\theta) + C \tag{4.7}$$

We drop this constant when calculating the energies in this study. The energies reported are in the non-dimensional form. The energies are non-dimensionalized by dividing by σR_T^2 where R_T is the radius of the tube.

$$e = \tilde{A}_{FS} - \tilde{A}_{wetS} \cos\theta \tag{4.8}$$

The energy is thus dependent just on the non-dimensional wetted ($\tilde{A}_{wetS}$) and free ($\tilde{A}_{FS}$) areas and the contact angle (θ).

4.3 Dimensional Analysis

This section looks at the various non-dimensional numbers associated with the transition problem and the transition time is expressed in terms of fluid properties and other non-dimensional numbers. The change in energy (ΔE) is defined as the difference in energies between the initial stable state before transition and the final stable state after transition. The transition time (τ) is defined as the time from when the initial topology breaks up till the time when the variation in energy of the new stable state is within 1% of the change in energy between the initial and the

final state. There are nine variables considered to be relevant in the study of such a transition problem and these are listed in the table below,

Table 4.1.: Dimensional Analysis Quantities

#	**Quantities**		**M**	**L**	**T**
1	Change in Energy	ΔE	1	2	-2
2	Liquid Volume	V	0	3	0
3	Surface Tension	σ	1	0	-2
4	Acceleration	a	0	1	-2
5	Viscosity	μ	1	-1	-1
6	Density	ρ	1	-3	0
7	Tube Radius	R_T	0	1	0
8	Transition Time	τ	0	0	1
9	Contact Angle	θ	0	0	0

Since we have nine variables and three fundamental dimensions (mass, length and time) we will have six non-dimensional numbers which should help define the problem. The contact angle (θ) has no dimensions and can be a non-dimensional number.

$$\Pi_1 = \theta \tag{4.9}$$

The volume can be non-dimensionalized by the radius of the tube and is a second non-dimensional number.

$$\Pi_2 = v = \frac{V}{R_T^3} \tag{4.10}$$

The Bond number is chosen as the non-dimensional number for the effect of acceleration or gravity. The energy change is non-dimensionalized using the surface tension and the radius of the tube.

$$\Pi_3 = Bo = \frac{\rho a R_T^2}{\sigma} \tag{4.11}$$

$$\Pi_4 = e = \frac{\Delta E}{\sigma R_T^2} \tag{4.12}$$

We now have four non-dimensional quantities and we have used all the variables except the transition time and the viscosity. We assume Reynolds number as the non-dimensional number including both the remaining quantities. This gives us the freedom to pick the last non-dimensional number. For the sixth non-dimensional number, the Ohnesorge number is used to limit the transition time to appear in just one non-dimensional number.

$$\Pi_5 = Re = \frac{\rho R_T^2}{\mu \tau} \tag{4.13}$$

$$\Pi_6 = Oh = \frac{\mu}{\sqrt{\rho \sigma R_T}} \tag{4.14}$$

Now the Reynolds number can be taken to be a function of the remaining non-dimensional numbers.

$$f_1(\theta, v, Bo, Re, e, Oh) = 0 \tag{4.15}$$

$$\frac{1}{Re} = f_2(\theta, v, Bo, e, Oh) \tag{4.16}$$

Reynolds number can be substituted in and we can write the transition time as,

$$\tau = \frac{\rho R_T^2}{\mu} f_2(\theta, v, Bo, e, Oh) \tag{4.17}$$

To deal with the non-linear dependence on the tube radius, we can define length in terms of the energy and surface tension as $\sqrt{\frac{\Delta E}{\sigma}}$.

$$\tau = \frac{\rho R_T}{\mu} \sqrt{\frac{\Delta E}{\sigma}} f_4(\theta, v, Bo, e, Oh) \tag{4.18}$$

In this current study, we deal with zero gravity flows and hence the Bond number can be neglected. Also assuming a constant contact angle and volume we get,

$$\tau = \frac{\rho R_T}{\mu}\sqrt{\frac{\Delta E}{\sigma}} f_5(e, Oh) \tag{4.19}$$

4.4 Assumptions

The flow is considered to be incompressible and isothermal. The two fluids are immiscible and do not mix with each other under any circumstance. Phase change for both the fluids is neglected. Since the volume of fluid algorithm conserves volume, the volume of the two fluids should not change. The walls are assumed to be smooth and impermeable. This implies that there is no flow through the walls and any addition or removal of fluid happens through the specified inlet/outlet patches. There is no gravity or external acceleration in the model. Hence all body forces due to gravity can be neglected and the Bond number is negligible. The transition between the stable states is assumed to be slow enough to consider the flow to be laminar. This reduces the computation cost as there is no need to solve additional equations to calculate turbulence properties.

It is not possible to get a constant value for the free and wetted areas at static equilibrium in OpenFOAM as there appears to be some variation because of slight disturbances in the interface. Thus static equilibrium is assumed when the change in energy is less than 1% compared to the previous value. While computing plug to droplet transitions, transition time is calculated till the next immediate stable state which in most cases is a system of two droplets. It has been shown in previous studies with the straight circular cylinder that a single droplet always has a lower energy than two droplets of the same total volume. Two possible mechanisms for the merging of the two droplets into one, are possible phase change between the two drops, or movement of the droplets due to dust and other impurities on the surface of the cylinder. Since both of these are not modeled in this study, we take the

next immediate stable state for calculating transition times. The effects of parasitic velocities are neglected as they do not seem to affect the parameters of interest to us in this study. We also neglect the effect of density and velocities when calculating energies as both the initial and final states are at equilibrium.

5. RESULTS AND DISCUSSION

5.1 Static Equilibrium Solutions

Before we look at the transitions between the different topologies, it is necessary to evaluate the performance of OpenFOAM in such a study. To do this, we compare static equilibrium energies for a selected range of volumes and contact angles, in both the plug and the droplet regimes (from Figure 1.4), with the energies computed by Surface Evolver (droplet) or from the analytical solution (plug). Since we are looking at only the static equilibrium solutions, the model is a simple continuous circular cylinder and there is no inlet patch to add or remove fluid from the domain.

5.1.1 Grid Dependence Study

As with any computational study, it is important to look at how the grid affects the computations and to pick the ideal grid which is a good compromise between accuracy and computational cost. Initially the use of dynamic grid refinement around the region of the interface was employed. Since the location of the interface is determined by the value of the alpha field, the cells close to the interface can be marked if $(0 < \alpha < 1)$ and refined. Though the energy computed for a contact angle (θ) of 10° and $v = 0.5$ was within 3% of the energy calculated by Surface Evolver, it was found that the time steps became smaller and smaller and became computationally more expensive than using a static grid for the same accuracy.

We look at three different levels of grid refinement and compare the energies calculated from these computations with the energy calculated by Surface Evolver. Grid refinement in this case is defined as the increase in the number of cells in the domain decreasing the cell volumes. The results are presented in Table 5.1 where

v is the non-dimensional volume, e is the non-dimensional energy and A_{FS} is the non-dimensional free surface area.

Table 5.1.: Static Grid Dependence Study

# of Cells	A_{FS}	v	e
148000	3.62905	0.994079	1.791565
223000	3.66243	0.997876	1.82469
450000	3.64151	0.995392	1.796995
600795	3.75905	0.994996	1.837995
1058700	3.67993	0.999012	1.833175

These computations are for $\theta = 60^\circ$ and $v = 1$. Steady state is assumed to be attained when the variations in energies fall below 1% between two consecutive energy calculations. Energy is calculated once every 10^{-3}s during the solver run. It is observed that the relative error in non-dimensional area and energy compared to the values from Surface Evolver is always less than 5%. Comparing within the grid independence study, we see that the difference between the minimum and maximum non-dimensional energy values calculated is around 0.047. The solution with 600,795 cells seems to have a higher error than all the other cases though the difference is not much. The computation time to attain steady state using a grid with 450,000 cells is around 200 hours when running parallel with 16 processors. Further refinement would further increase the computational cost with not much increase in accuracy. We find that the energy for this particular case is within 2% of the energy computed by Surface Evolver and hence we use the grid with 450,000 cells in all the static equilibrium computations that follow. We also do not compute to find out the behavior of grid induced errors at higher refinement as it becomes computationally very expensive to even make an attempt. Errors reported in this section are all relative errors given as,

$$\%Error = \frac{E_{OF} - E_{SE}}{E_{SE}} \tag{5.1}$$

where E_{OF} is the energy from OpenFOAM and E_{SE} is the energy from Surface Evolver.

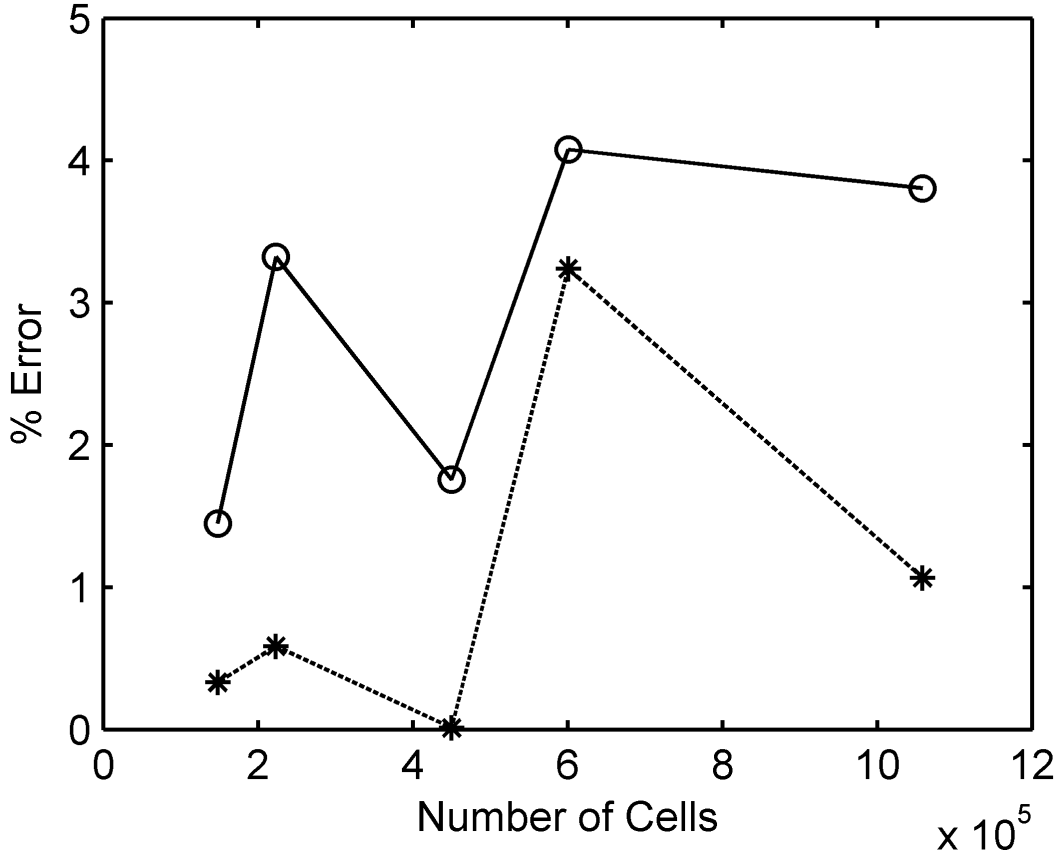

Figure 5.1.: % Error with Grid Cells. Dashed line is for non-dimensional free surface area. Solid line is for errors in non-dimensional energy. The markers denote exact data points.

5.1.2 Comparison of Solutions with Surface Evolver

Collicott et al. [12] used Surface Evolver to calculate energies for droplet topologies in a cylindrical tube, and most of the Surface Evolver results presented here are from

that study. We look at solutions for contact angles of 10°, 30°, 60°, 90°, and 120° for a whole range of volumes. We look at the non-dimensional energies and free surface areas and compare them with values from Surface Evolver. Unless specified, all the energies and free surface areas mentioned in this chapter are non-dimensionalised. The non-dimensional pressure is also compared for a contact angle of 30° (Figure 5.2). The difference in pressure across the interface is non-dimensionalised by the surface tension and radius of the tube.

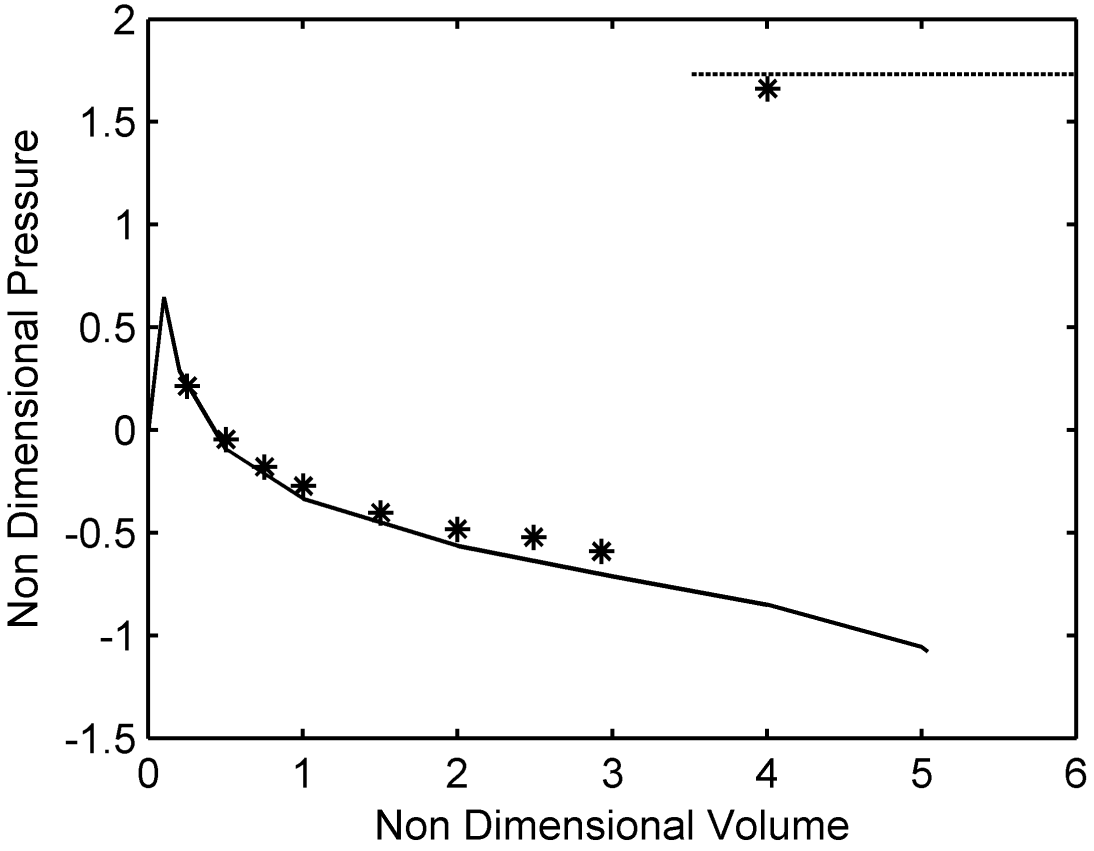

Figure 5.2.: Non-Dimensional Pressure for $\theta = 30°$. The solid line shows the non-dimensional pressure from surface evolver. The markers show non-dimensional pressure from OpenFOAM. The flat line at the top represent non-dimensional pressure for liquid plug solutions.

The non-dimensional pressure presented here for $\theta = 30°$ follows the trend predicted by earlier studies well. It is however seen that it is not very reliable to predict pressures, as there are inaccuracies in calculating the curvature, which plays a major role in predicting pressure. The presence of parasitic currents at the interface also does not help in the pressure calculation. This is evident at $\theta = 120°$ at lower volumes where the non-dimensional pressure value can be off by up to 0.5.

Hence we focus our attention on comparing the energies and the free surface areas to establish that the multiphase solver is effective at computing the interfaces of interest to us. The free surface areas for $\theta = 10°$ deviate quite a bit from the line predicted by Surface Evolver. At these low contact angles the interface is a lot more curved, and since the interface is approximated, such large difference in surface areas is not surprising. However we see that the energies are very close to the line predicted by Surface Evolver. As the contact angle increases we see that the areas are closer to Surface Evolver calculations. Throughout the $v - \theta$ space, the energies calculated are within 5% of Surface Evolver values.

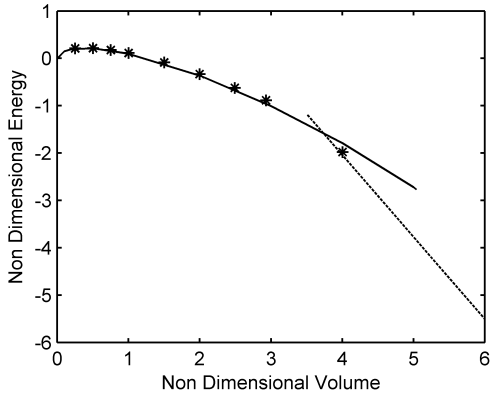

(a) Non-Dimensional Energy

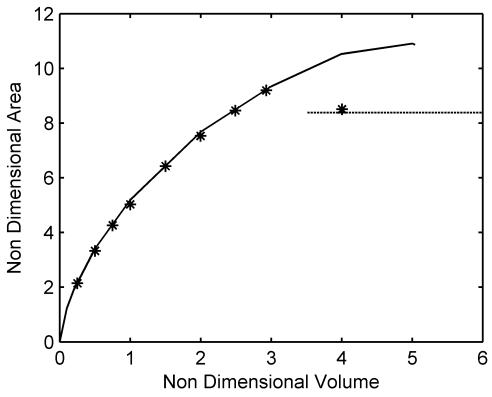

(b) Non-Dimensional Free Surface Area

Figure 5.3.: Contact Angle = 30°; The solid line shows results from Surface Evolver and the markers are from OpenFOAM

As described in earlier studies Surface Evolver works with an algorithm which minimizes the total energy. In the case of OpenFOAM we find that the final topologies are dependent on the initial definition of the alpha field. This means that at volumes where both the plug and the droplet can exist but the droplet is the minimum energy solution (from Figure 1.4), a plug can be formed if the initial alpha field defined approximates the required plug topology. This liquid plug seems to be quite stable and does not collapse to the minimum energy state naturally. This fact is useful later in studying transitions from a plug to droplet as we can start close to the expected transition region rather than all the way in the stable plug region. Thus in order to get a droplet at these lower volumes, the initial alpha field is set as a spherical droplet in contact with the wall of the cylindrical tube.

It is also seen that the solution becomes dependent on the grid size as we get close to the minimum plug volume region and the maximum droplet region. Close to the maximum droplet volume, initializing a spherical droplet to get a stable droplet solution led to a liquid plug. This is because, as the contact angle boundary condition at the wall deforms the droplet making it adhere to the contact angle, the liquid surface touches the walls forming a contact line throughout the circumference of the cylinder which then forces the topology to shift to a plug. This is seen around $v = 3.7$ for all the contact angles presented here for the current grid. It is important to note that at these high volumes, the liquid plug is the minimum energy solution. One way to circumvent this problem would be to form a stable droplet at a lower volume and slowly add liquid till we get to the higher volumes.

On the other end of the spectrum, close to the minimum plug solution, when the contact surfaces touch at the center of the cylindrical tube ($0^\circ \leq \theta \leq 90^\circ$) or at the circumference of the tube ($90^\circ \leq \theta \leq 180^\circ$) the grid has to be well resolved in order to properly capture the small volumes in between the two surfaces. At the minimum volume point this corresponds to a grid size of almost zero, which is not practically possible to generate. Hence depending on the size of the cell we find that

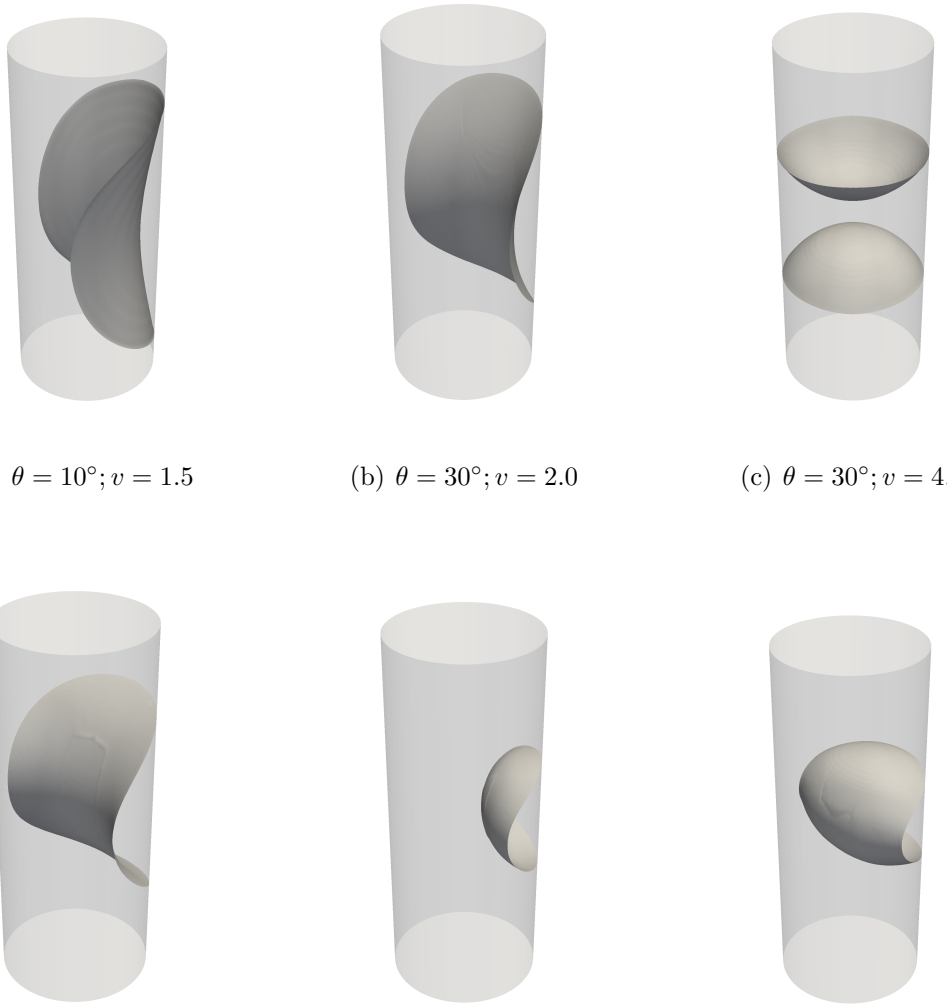

(a) $\theta = 10°; v = 1.5$ (b) $\theta = 30°; v = 2.0$ (c) $\theta = 30°; v = 4.0$

(d) $\theta = 60°; v = 3.0$ (e) $\theta = 90°; v = 1.0$ (f) $\theta = 120°; v = 2.5$

Figure 5.4.: Stable static equilibrium solutions for different contact angles θ and non-dimensional volumes v. Iso-surfaces are plotted at $\alpha = 0.5$ from the alpha field calculated by OpenFOAM.

the minimum volume of the plug varies. This is also seen in the plug to droplet transitions discussed later.

5.2 Transitions Between Stable States

Up to this stage we have established, based on the static cylindrical tube computations, that OpenFOAM predicts the energies of the stable states quite accurately in most cases. We now move on to computing transitions between the different stable states. The three main parameters that are of interest in this section are the non-dimensional energy, non-dimensional transition volumes and the non-dimensional transition time. Transition time, as mentioned earlier, is defined as the time from when the interface breaks up till the time when the energy variations between two time steps are within 1% of the energy difference across the transition. The model used now is a cylindrical tube with square inlets to add or remove fluid from the domain as described in Section 4.1.

5.2.1 Grid Dependence Study for Transitions

As in the case of the static equilibrium topologies, it is important to look at how the grid affects the transitions between the two states. First we consider the transition from a stable liquid droplet to a liquid plug topology for a contact angle of 60°. We consider three grids with nearly uniform cell volumes having 228125, 486000, and 960000 cells. Fluid is added into the cylinder through the square inlet at a constant volume flow rate. The energies, as the liquid volume increases with time, are shown in Figure 5.5 for all the three cases. The energies for all the three grid resolutions follow a similar trend and are very close in value, with the coarse grid having a slightly higher energy than the other two. We find that the transition volumes are also almost identical with 4.484, 4.518, and 4.519 for the three grids for increasing number of cells. Since the behavior is identical for 486000 and 960000 cells, the grid with lesser number of cells is used to save on computational cost.

For the transition from a liquid plug to a droplet we observe a greater dependence on the grid resolution as is expected. This is observed by looking at the non-dimensional energy variation with time for grids with 228125, 405000, 960000,

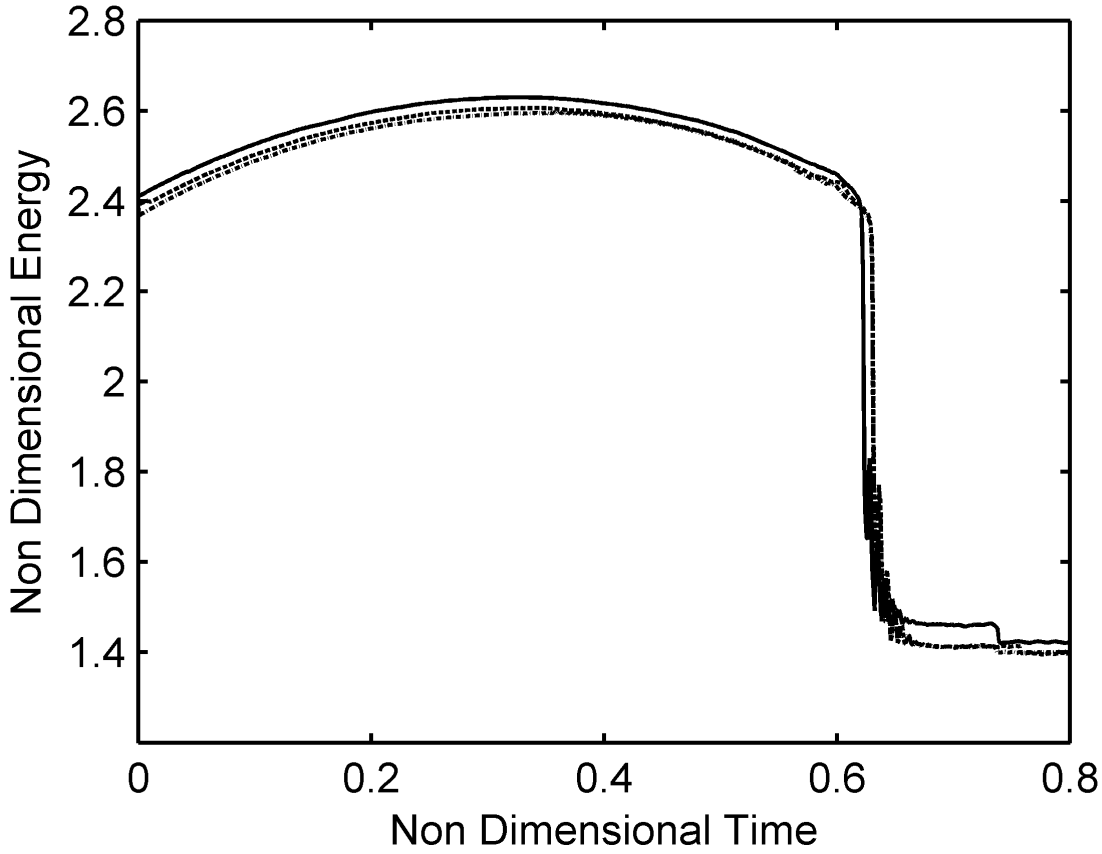

Figure 5.5.: Non-Dimensional energy with time for droplet to plug transitions. Inital Volume = 2.0. The solid line is for the grid with 228125 cells, the dashed line is for the grid with 486000 cells and the dash-dot line is for the grid with 960000 cells.

and 1875000 cells for a contact angle of 60°. The transitions from a liquid plug to a droplet, as will be seen in later sections, seem to occur close to the minimum volume of existence for the plug solution. At such low volumes the gap between the two free surfaces of the liquid plug has to be well resolved by the grid. If there are insufficient number of cells in the gap between the two free surfaces, the liquid plug would transition as it is no longer possible to reconstruct the interface accurately. It is seen that the transition is delayed to lower volumes as the number of cells increases. This delay in transition leads to a difference in energy, as seen in Figure 5.6. The volume

at which the liquid plug breaks up is 1.596, 1.446, 1.331, and 1.251 respectively for 228125, 405000, 960000, and 1875000 cells.

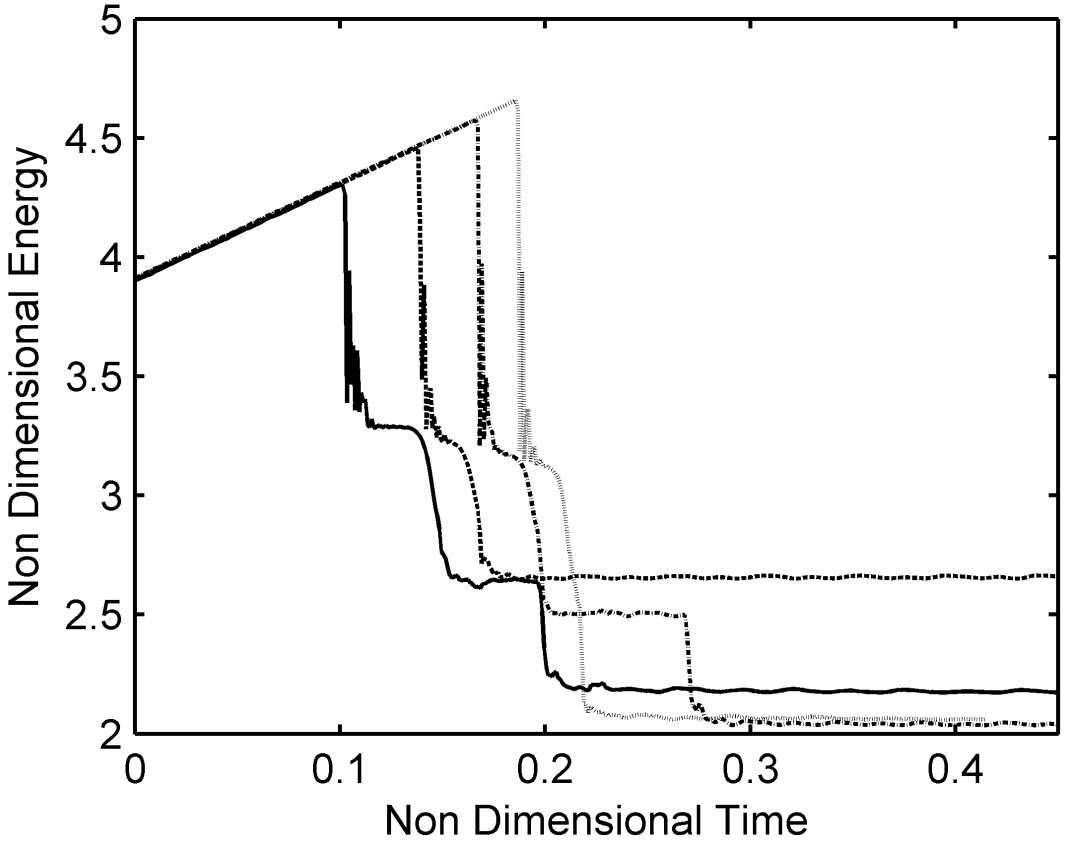

Figure 5.6.: Non-Dimensional energy with time for plug to droplet transitions. Inital Volume = 2.0. The solid line is for the grid with 228125 cells, the dashed line is for the grid with 405000 cells, the dash-dot line is for the grid with 960000 cells and the dotted line is for the gird with 1875000 cells.

With increase in the number of cells there is also an increase in the computation time, which goes as high as 600 hours for the grid with 1875000 cells, using 48 processors in parallel processing. Since we are dealing with very very small gaps in the case of liquid plugs at their minimum volume of existence it would mean that an infinite grid resolution would be required to capture the solution accurately. Hence it becomes a challenge of getting close to the actual solution, while still maintaining

reasonable computation times. Keeping this in mind the grid with 960000 cells is used for predicting the transitions from a liquid plug to a droplet in subsequent sections.

5.2.2 Droplet to Plug Transitions

The droplet to liquid plug transitions are effected by addition of fluid to an existing stable droplet volume through one of the inlet patches at a constant volume flow rate of $4 \times 10^{-9} m^3/s$. The transitions are computed for $\theta = 10^\circ$ to $\theta = 170^\circ$ in increments of 10°. The initial volumes are different for each contact angle as efforts were made to reduce the computational cost by having the initial volume as close to the expected transition volume as possible. It is also important to note that the fluid addition is stopped as soon as the topology changes and the liquid is allowed to form an equilibrium shape at a constant volume. Three main parameters, the non-dimensional energy variation, non-dimensional transition volumes and times are studied and plotted. The transition volumes are plotted for all the contact angles studied in Figure 5.7.

The solid line is the maximum volume of existence line for the liquid droplet predicted by Surface Evolver, while the markers are the volumes at which the transitions occur. The transitions occur around the maximum volume of existence region calculated by Surface Evolver. However, it is seen that for all acute contact angles the transitions occur at volumes higher than the maximum volume of existence for a droplet at that particular contact angle. This difference is particularly high for very small contact angles. It remains to be seen if this difference between the two is due to inadequacies in OpenFOAM or Surface Evolver. As seen in the previous section, this particular transition is independent of the grid resolution and hence it is very unlikely that this is caused by a grid related error. There are some other known issues with the interFoam solver, such as the poor curvature calculation and approximation of the interface, but these would not explain the difference in the maximum volume of existence for a droplet. Further investigation is required in this regard to precisely

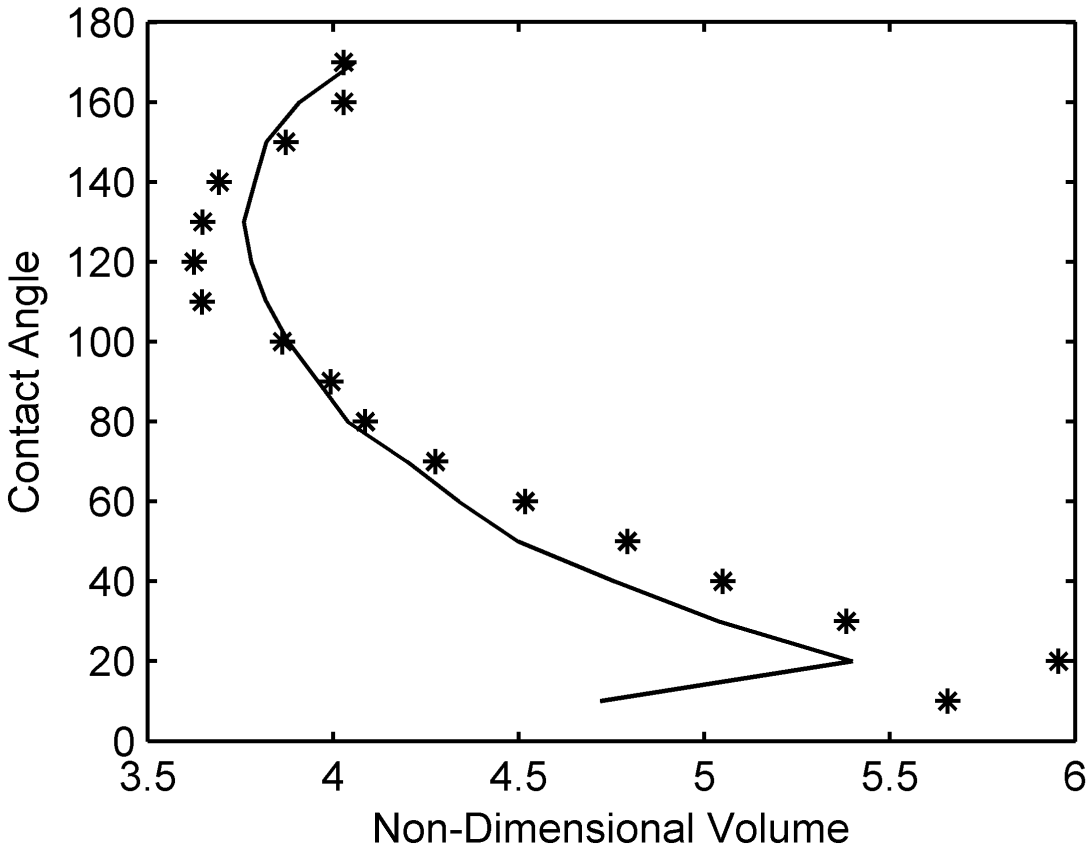

Figure 5.7.: Non-Dimensional transition volume at different contact angles (θ) in increments of 10°. Maximum volume of existence for droplet calculated using Surface Evolver is also shown.

isolate the problem and to try to correlate the results from both the computational methods.

There are three modes of transitions which are observed depending on the contact angle. For a low contact angle of 10° it is observed that as liquid volume increases the droplet grows around the walls of the cylinder until its angular extent reaches 2π. At this condition the tips of the contact lines touch at the circumference of the cylinder and the droplet collapses to an annular structure. However, as shown in Figure 1.4, the annulus is not a stable solution even at these low contact angles at such high

volumes. The annulus exists for about $\tau = 0.04$ before the neck of the annulus constricts and it transitions to a liquid plug. The non-dimensional transition time as defined in earlier sections is calculated to be 0.057. A similar transition is observed for $\theta = 20^\circ$ and $\theta = 30^\circ$ where the annular structure becomes unstable even quicker. The non-dimensional transition time for these cases are 0.025 and 0.033. For $\theta = 30^\circ$ the annular structure exists for only around $\tau = 0.001$. For higher contact angles from $\theta = 40^\circ$ to $\theta = 120^\circ$ the transition occurs before the angular extent of the droplet reaches 2π. In the study using Surface Evolver with a straight circular cylinder it was supposed that the transitions occur because of some sort of an instability. The instability was not captured in this study. We find that as the volume increases the liquid obstructs more of the tube and eventually transitions to a liquid plug when it gets close to the volume where it completely obstructs the tube. This can be seen in Figure 5.11. Once the tube is completely obstructed the two free surfaces wobble before settling down to a stable state. The non-dimensional transition times for these angles are calculated to be 0.038, 0.035, 0.034, 0.037, 0.051, 0.062, 0.052, 0.071, and ∞ respectively for every 10° increment in contact angle.

For higher contact angles when the liquid does not wet the surface of the tube wall, we observe that with increase in volume the droplet grows in size until it completely obstructs the tube and transitions to a liquid plug. In this case the free surface touches the wall of the tube when transition occurs. In quite a large number of cases the liquid structures seem to move along the walls of the tube. This is not physical and is most likely an effect of the parasitic currents induced at the interface or due to the presence of the inlet patch itself on the wall of the cylinder. This however does not seem to affect the transition and hence is overlooked. The non-dimensional transition times for $\theta = 130^\circ$ to $\theta = 170^\circ$ are ∞, ∞, 0.071, 0.065, and ∞ for every 10° increase in contact angle. In the case of $\theta = 120^\circ$, $\theta = 130^\circ$ and $\theta = 140^\circ$ the end caps are unstable and keep wobbling with amplitude increasing with time. However in the case of $\theta = 120^\circ$ and $\theta = 130^\circ$ this eventually dies down and the change in energy between two subsequent times reduces by a few orders of magnitude, but is

still not within the 1% limit imposed. For $\theta = 140^\circ$ the two end caps continue to wobble as can be seen from the plot showing the non-dimensional energy with time. When $\theta = 170^\circ$ the final topology is much more stable than the other three cases and is just a case where the limit imposed is very low as the change in energy is negligible across the transition.

Looking at the non-dimensional energy as time progresses, which consequently means that the volume increases until transition, it is seen that for contact angles below 60° the non-dimensional energy decreases as volume is added and there is a jump in energy as soon as the fluid volume changes topology. Looking at an example, at a contact angle of 10° (Figure 5.12) we see that the energy decreases as volume is added till a non-dimensional time of 1.012. At this point the droplet changes topology and begins to transition to a different state. The addition of liquid volume is stopped at this point and the fixed liquid volume is allowed to evolve to its final stable state. The transition is seen as the drop in energy. For all higher contact angles, the non-dimensional energy increases as the volume increases and then drops steeply during the transition to the energy of the plug topology. Since the transitions occur in the region where the droplet is the state with a higher energy there is always a fall in the non-dimensional energy over the transition period. For higher contact angles this drop is almost negligible as can be seen in the case of $\theta = 160^\circ$. From the non-dimensional plots we can also see small bumps in energy before the transition as seen in the case of $\theta = 160^\circ$. This is an artifact of the droplet moving along the tube wall or covering the second inlet as the droplet covers more of the wall as it grows.

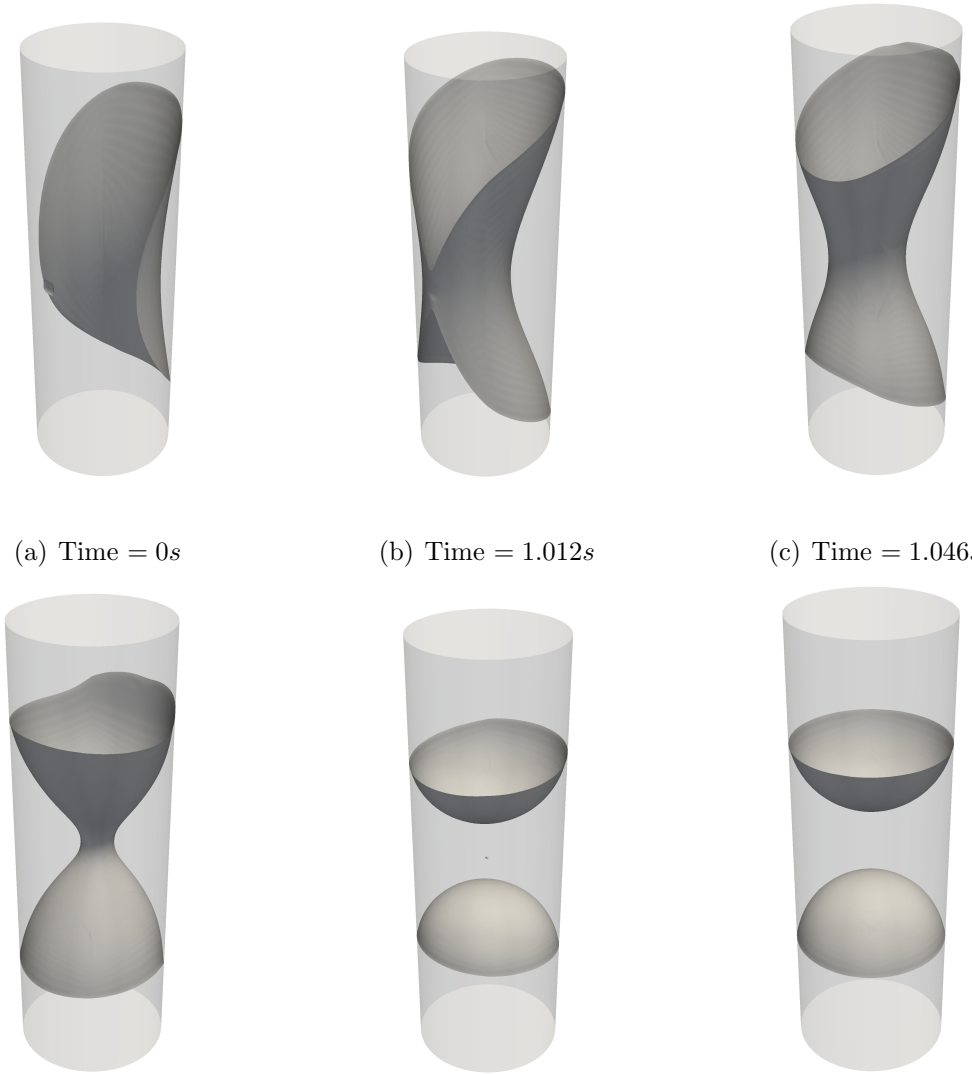

(a) Time = $0s$ (b) Time = $1.012s$ (c) Time = $1.046s$

(d) Time = $1.06s$ (e) Time = $1.07s$ (f) Time = $1.4s$

Figure 5.8.: Contact Angle = 10°; Droplet To Plug; Initial Volume = 1.65; Transition Volume = 5.66; Transition Time = $0.057s$. Iso-surfaces are plotted at $\alpha = 0.5$ from the alpha field calculated by OpenFOAM.

(a) Time = $0s$ (b) Time = $0.32s$ (c) Time = $0.63s$

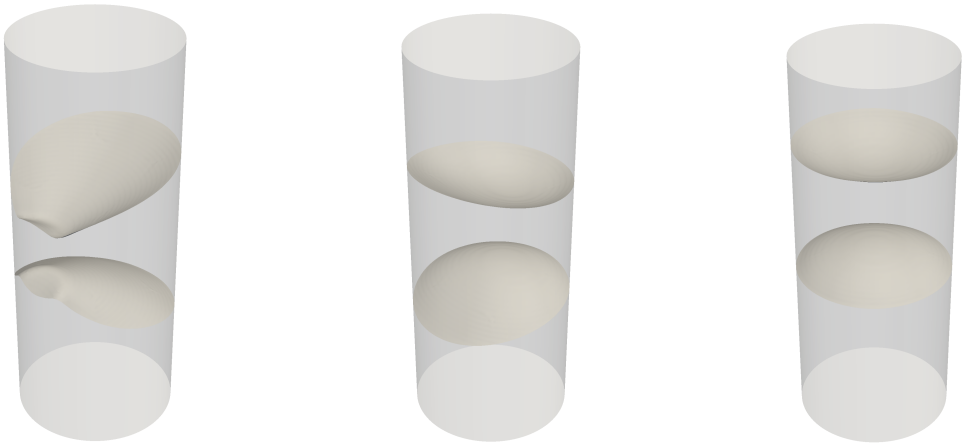

(d) Time = $0.631s$ (e) Time = $0.65s$ (f) Time = $2.3s$

Figure 5.9.: Contact Angle = 60°; Droplet To Plug; Initial Volume = 2.0; Transition Volume = 4.52; Transition Time = $0.034s$. Iso-surfaces are plotted at $\alpha = 0.5$ from the alpha field calculated by OpenFOAM.

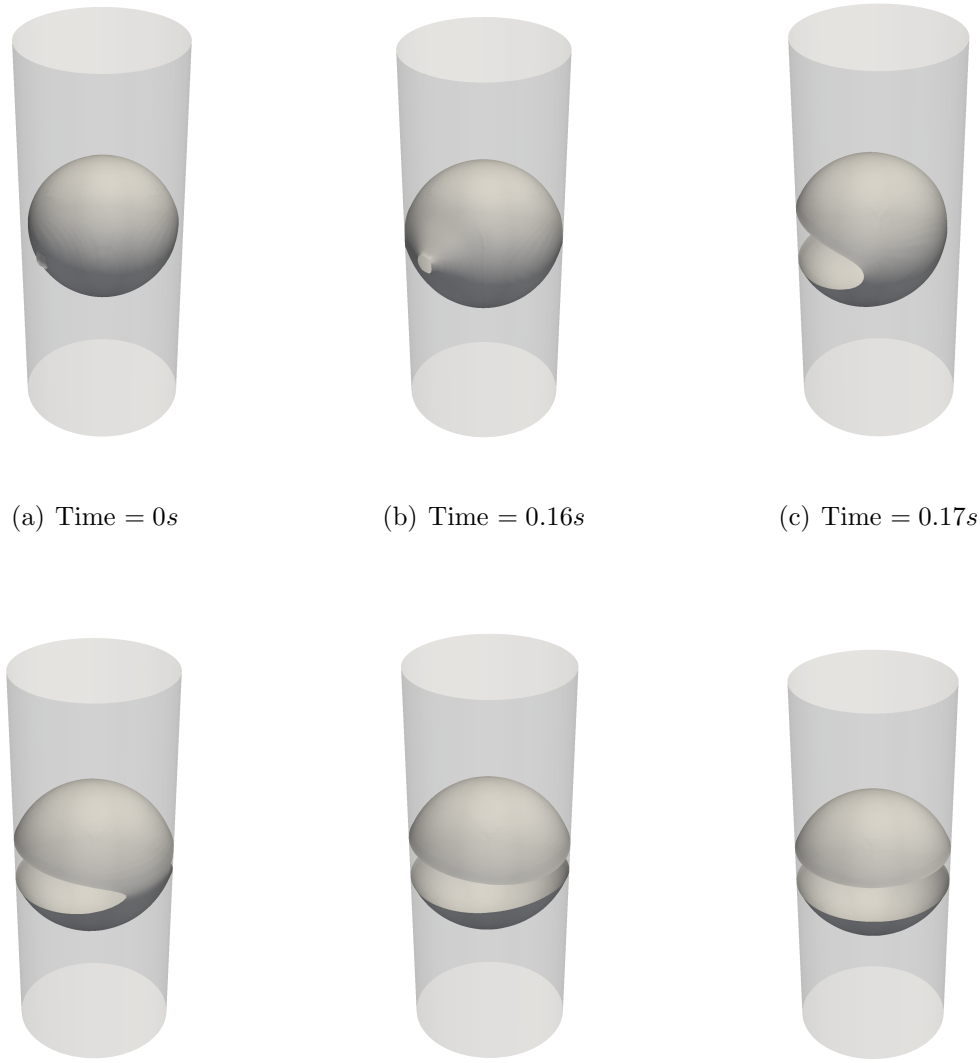

(a) Time = $0s$ (b) Time = $0.16s$ (c) Time = $0.17s$

(d) Time = $0.256s$ (e) Time = $0.257s$ (f) Time = $0.6s$

Figure 5.10.: Contact Angle = 160°; Droplet To Plug; Initial Volume = 3.0; Transition Volume = 4.03; Transition Time = $0.065s$. Iso-surfaces are plotted at $\alpha = 0.5$ from the alpha field calculated by OpenFOAM.

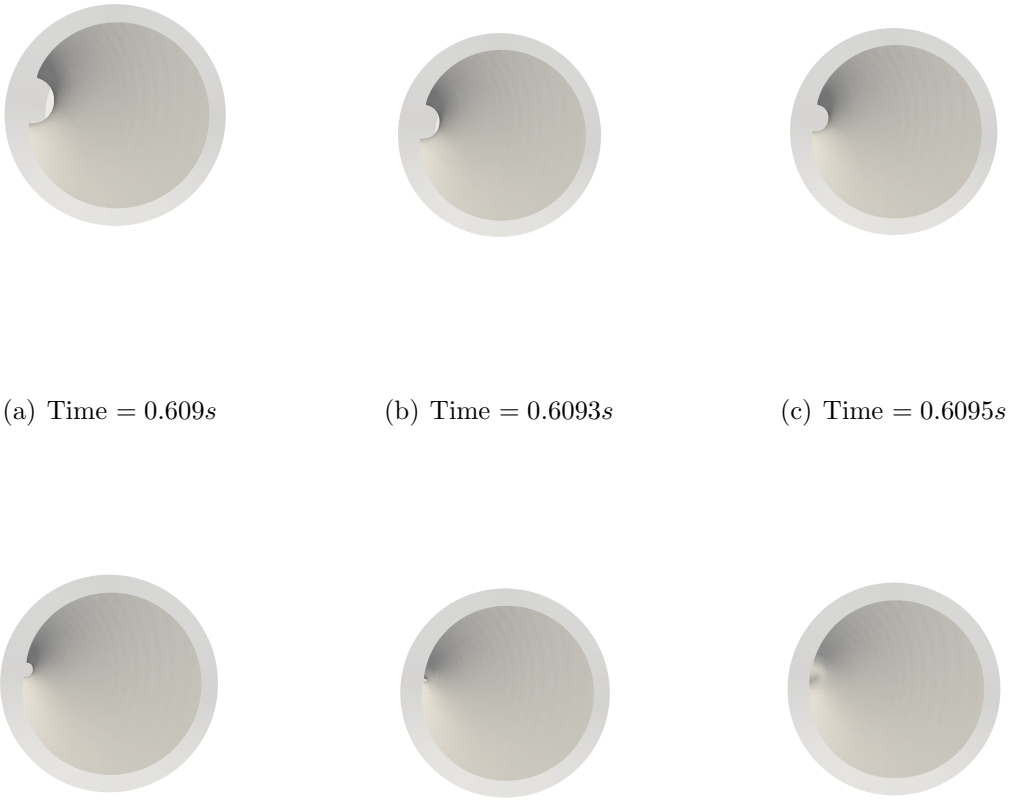

(a) Time = $0.609s$ (b) Time = $0.6093s$ (c) Time = $0.6095s$

(d) Time = $0.6097s$ (e) Time = $0.6098s$ (f) Time = $0.6099s$

Figure 5.11.: Contact Angle = 80°; Droplet To Plug; Iso-surfaces are plotted at $\alpha = 0.5$ from the alpha field calculated by OpenFOAM. The iso-surface is plotted every 0.0001s of computational time in order to capture the dynamics of the transition.

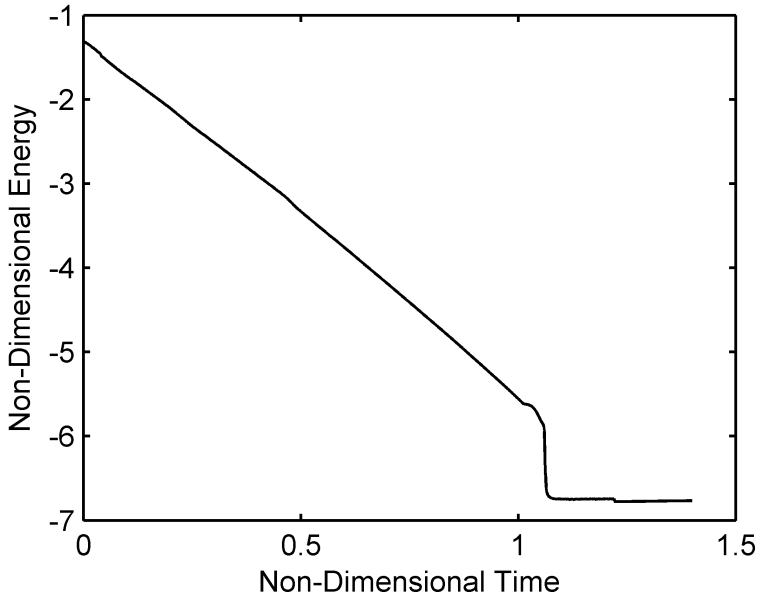

Figure 5.12.: Non-Dimensional energy with time for droplet to plug transitions at $\theta = 10°$. Initial Volume = 1.65. Transition Volume = 5.66.

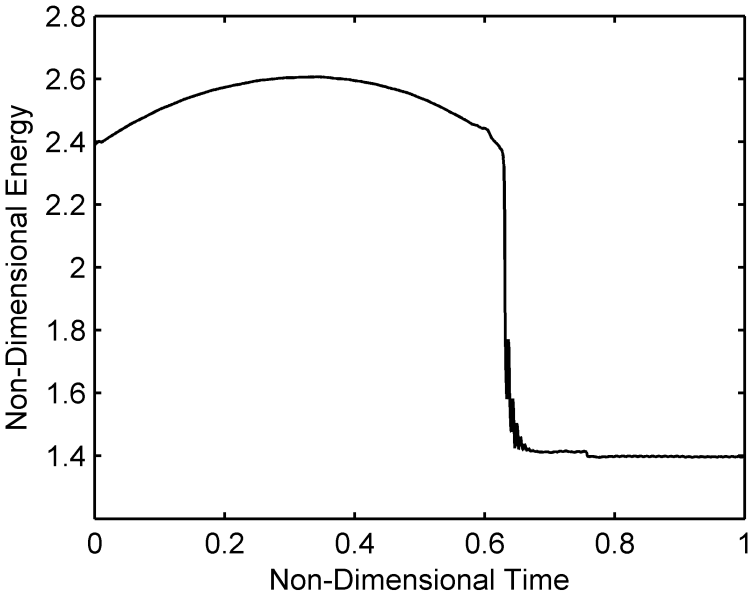

Figure 5.13.: Non-Dimensional energy with time for droplet to plug transitions at $\theta = 60°$. Initial Volume = 2.0. Transition Volume = 4.52.

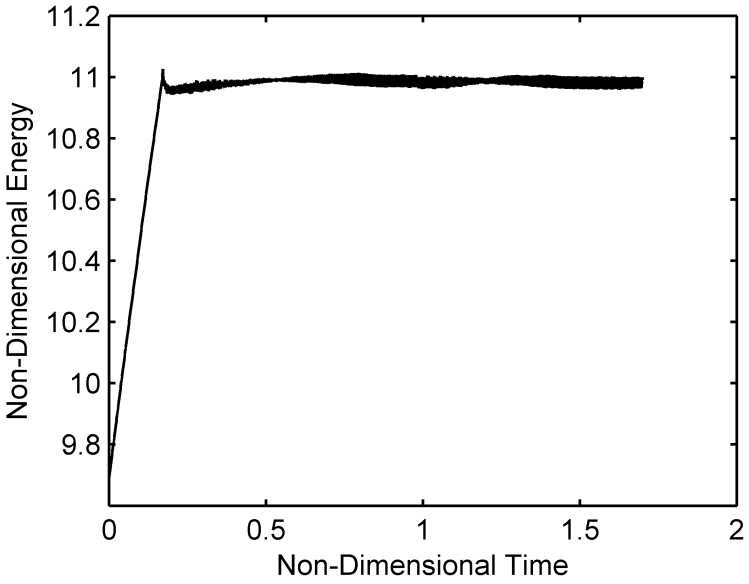

Figure 5.14.: Non-Dimensional energy with time for droplet to plug transitions at $\theta = 140°$. Initial Volume = 3.0. Transition Volume = 3.69. The effect of the unstable end caps can be seen by the fluctuations in the energy.

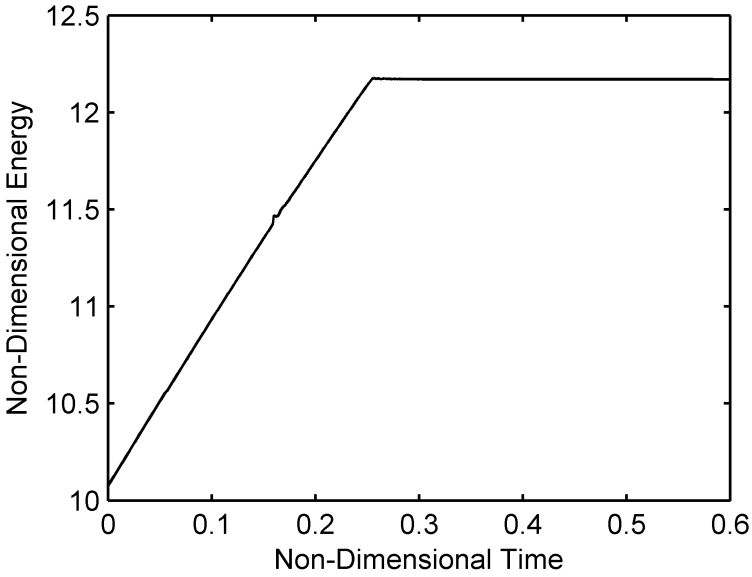

Figure 5.15.: Non-Dimensional energy with time for droplet to plug transitions at $\theta = 160°$. Initial Volume = 3.0. Transition Volume = 4.03.

5.2.3 Plug to Droplet Transitions

The plug to droplet transition is forced by removing fluid from a initial liquid plug topology through the two inlet patches till the liquid volume changes shape. The transitions are again computed for the same range of contact angles as earlier. The flow rate through the two inlet patches are $-2 \times 10^{-9} m^3/s$ each where the negative sign is to remove liquid from the domain. The flow through the inlet patches are stopped as soon as the liquid changes topology.

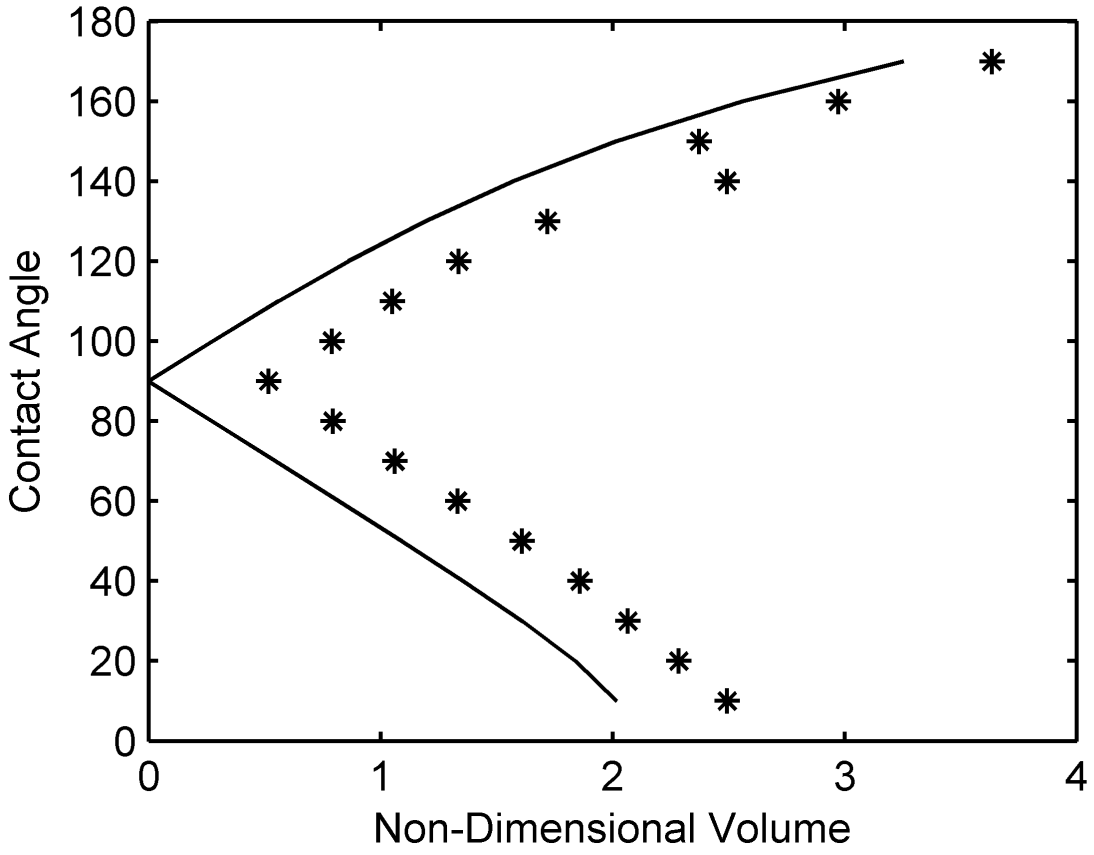

Figure 5.16.: Non-Dimensional transition volume for plug to droplet transitions at different contact angles (θ) in increments of 10°. The solid line shows the minimum volume of existence for a liquid plug calculated analytically and the markers show the transition volumes.

The transition volumes follow a similar trend with contact angle as the minimum volume of existence line for the plug. The minimum volume of existence was calculated analytically earlier in this study. The transition volumes are higher than the minimum volume of existence for the plug at a particular contact angle. This is because of the dependence of the solution on the grid resolution and a grid with more number of cells will push the transition volumes closer to the minimum volume of existence line for the liquid plug. It remains to be seen if the two would coincide at the same volume, as this would require an infinite grid resolution which is not practically possible in CFD studies.

There are two main modes of transition in the case of plug to droplet transitions depending on the contact angle. This is directly related to the minimum volume condition for the liquid plug (Figure 1.3) depending on the contact angle. For all contact angles less than 90° we find that as the volume of the plug decreases the two end caps move closer to each other until they collapse at the middle. This happens a bit before it reaches the minimum volume condition and this could be just a case of the grid unable to resolve the small volumes in-between the two caps as discussed in the grid dependence study. When $\theta = 10°$ the two end caps collapse at the center at $v = 2.494$ which is about 0.478 more than the minimum volume of existence at that contact angle. This difference is almost the same for all other contact angles. Once the end caps collapse the liquid now assumes an annular topology. In the case of this contact angle, the annulus is the minimum energy solution at this volume and thus we do not observe the annulus breaking up into a droplet. The non-dimensional transition time was calculated as 0.003. For all higher acute contact angles the end caps collapse at the middle just like earlier when the two end caps touch to form an annular structure. But since at these higher contact angles the annulus is not a stable solution it collapses by pinching on one side. The annulus breaks up into two droplets as the two contact lines of the annulus come together at two points along the circumference. When $\theta = 80°$ it is seen that the annulus breaks up into four droplets, two small droplets and two larger droplets. The two small droplets

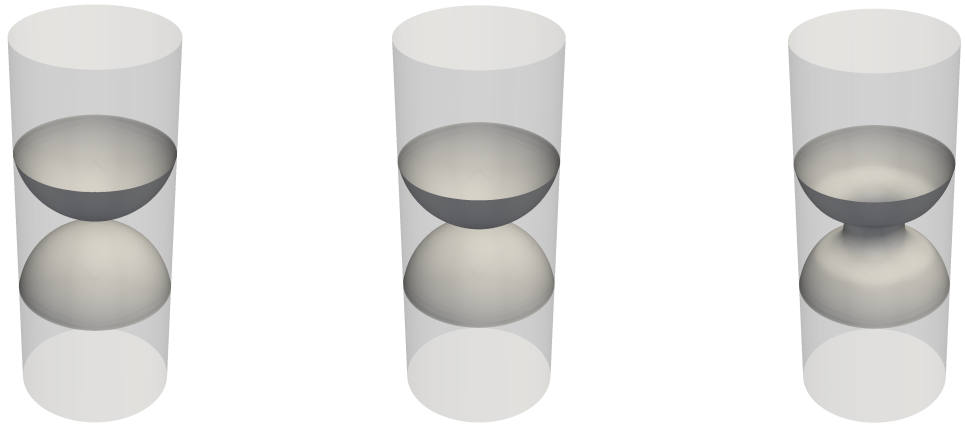

(a) Time = $0s$ (b) Time = $0.12s$ (c) Time = $0.124s$

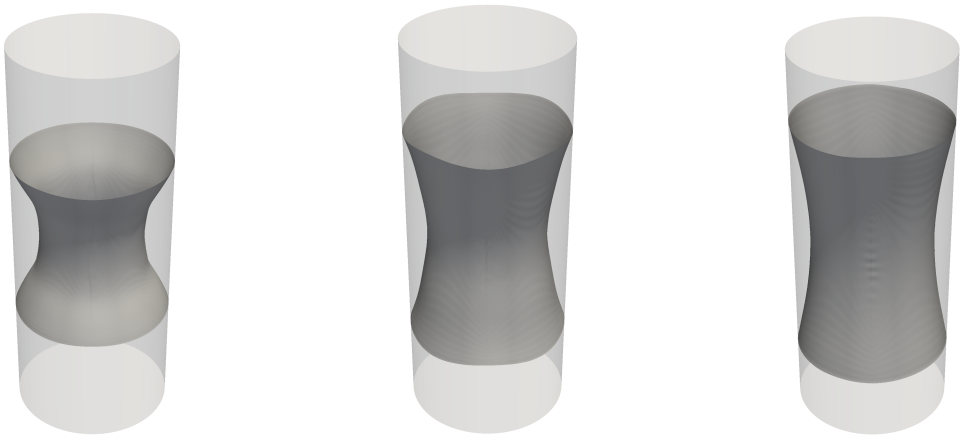

(d) Time = $0.125s$ (e) Time = $0.126s$ (f) Time = $0.2s$

Figure 5.17.: Contact Angle = 10°; Plug To Droplet; Initial Volume = 3.0; Transition Volume = 2.49; Transition Time = $0.003s$. Iso-surfaces are plotted at $\alpha = 0.5$ from the alpha field calculated by OpenFOAM.

are almost the same volume, and so are the two larger droplets. It is interesting to observe the location of the points where the two contact lines of the annulus meet. It is observed that as the contact angle increases, the two points move closer to the

mid plane of the tube, whose normal is perpendicular to the height of the tube. This means that the volume of the smaller droplet increases as the contact angle increases. The non-dimensional transition times for $\theta = 20^\circ$ to $\theta = 80^\circ$ in increments of 10° are 0.011, 0.071, 0.042, 0.012, 0.033, 0.03 and 0.094 respectively.

Starting from $\theta = 90^\circ$ we see the other mode of transition which is similar to the minimum volume condition for non wetting liquids. In this case the two end caps collapse close to the walls of the tube as they come closer together. For $\theta = 90^\circ$ the liquid plug breaks up at the periphery into two droplets of almost equal volume. For higher contact angles the transitions are identical. The liquid plug breaks up at the circumference of the tube and rolls up into a single droplet for all contact angles above 90°. In many cases both the initial plug and the final droplet move on the wall of the tube and are stretched by the two inlet patches. The movement stops and reverses direction when one of the free surfaces reaches the inlet patch. When looking at the velocity vectors around the interface it is observed that there are slightly high velocity vortex like structures close to the end caps. This could be due to the bad interface curvature calculation which causes parasitic currents at the interface. For $\theta = 90^\circ$ and $\theta = 130^\circ$ it is observed that the droplet moves out of the domain due to such movement along the walls. The transition times for $\theta = 90^\circ$ to $\theta = 170^\circ$ for increments of 10° are 0.007, 0.032, 0.03, 0.023, 0.019, 0.12, 0.215, ∞ and ∞.

For $\theta = 150^\circ$ the droplet gets pinned to both the inlets, and this causes an instability which coupled with the droplet movement makes the free surface move vigorously. The droplet eventually breaks free from one of the inlet patches and settles down. This means that the transition time is a lot higher than the other cases. In the case of $\theta = 160^\circ$ and $\theta = 170^\circ$ a similar phenomenon is observed where the droplet gets pinned to both the inlet patches and is unable to form a stable droplet solution. This can be seen in the energy variation plots as oscillations and do not die out. The amplitude of these decrease at around $\tau = 0.42$ when the droplet reorients itself but then continues though at a lower amplitude.

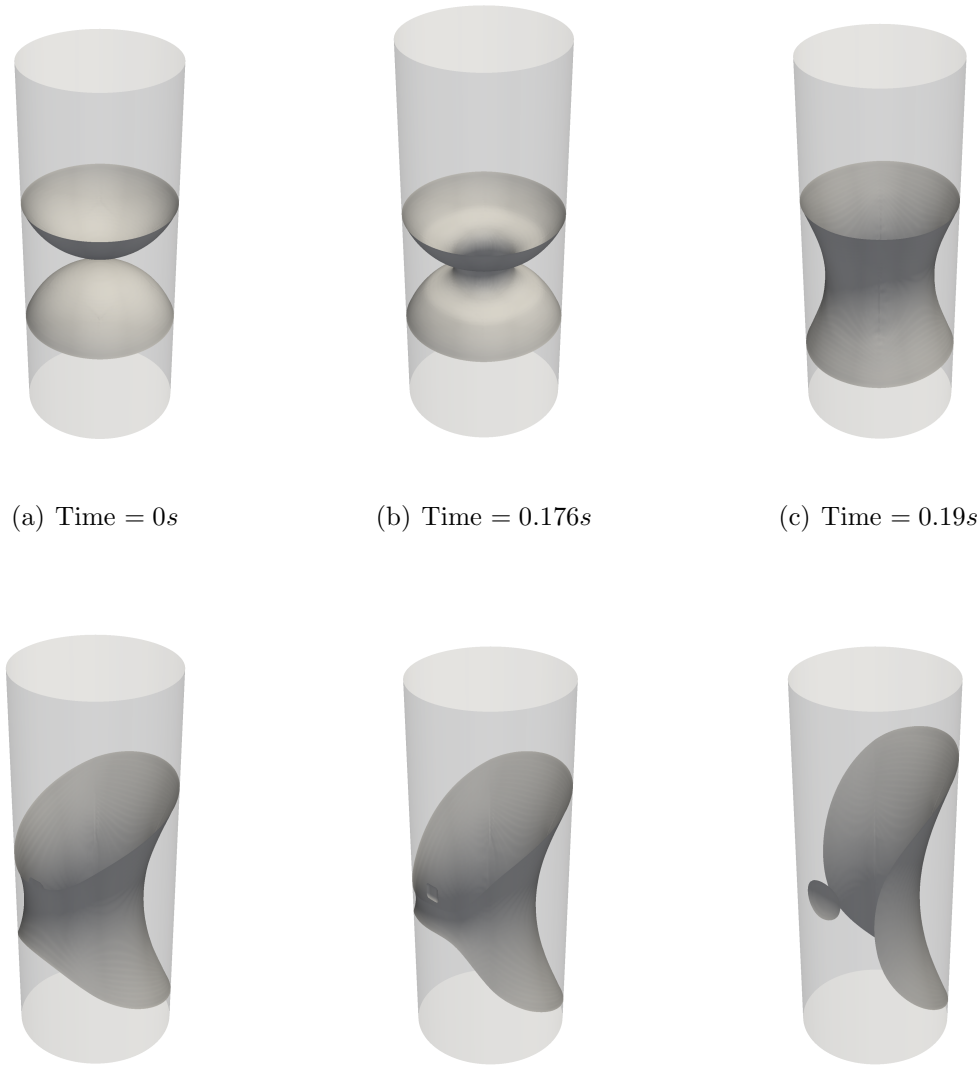

(a) Time = $0s$ (b) Time = $0.176s$ (c) Time = $0.19s$

(d) Time = $0.25s$ (e) Time = $0.26s$ (f) Time = $0.5s$

Figure 5.18.: Contact Angle = 20°; Plug To Droplet; Initial Volume = 3.0; Transition Volume = 2.28; Transition Time = $0.011s$. Iso-surfaces are plotted at $\alpha = 0.5$ from the alpha field calculated by OpenFOAM.

As volume of the liquid plug decreases the wetted surface area decreases. As a consequence the non-dimensional energy increases for acute contact angles and

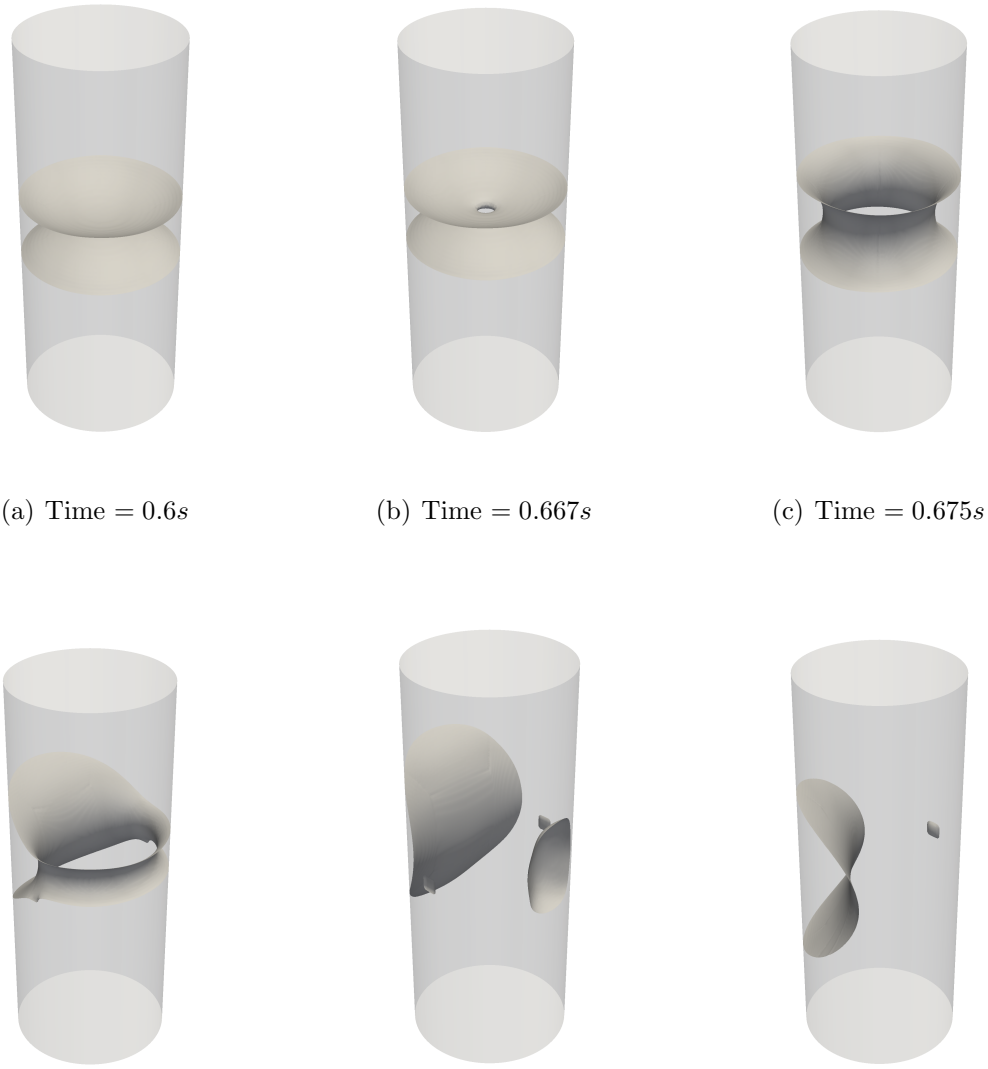

(a) Time = $0.6s$ (b) Time = $0.667s$ (c) Time = $0.675s$

(d) Time = $0.695s$ (e) Time = $0.7s$ (f) Time = $1.1s$

Figure 5.19.: Contact Angle = 60°; Plug To Droplet; Initial Volume = 4.0; Transition Volume = 1.33; Transition Time = $0.033s$. Iso-surfaces are plotted at $\alpha = 0.5$ from the alpha field calculated by OpenFOAM.

decreases for higher contact angles. The oscillations in energy seen at lower contact angles are because of the droplet moving along the tube walls and getting stretched

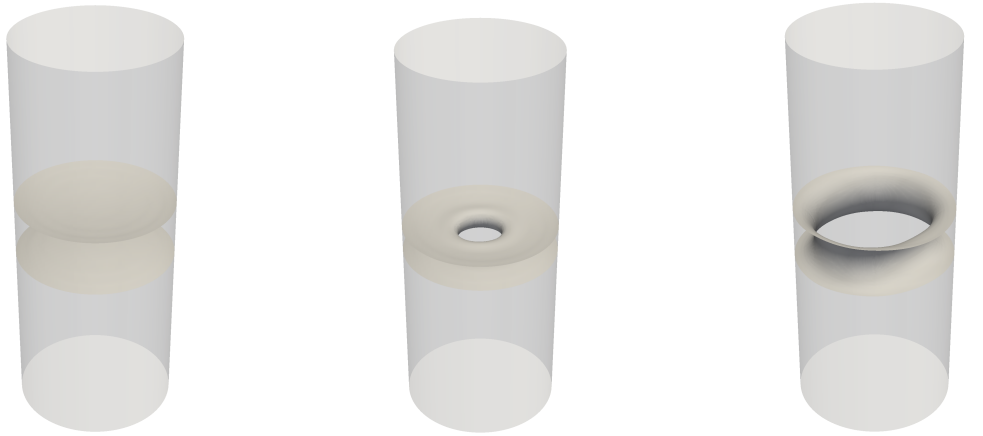

(a) Time = $0s$ (b) Time = $0.3s$ (c) Time = $0.305s$

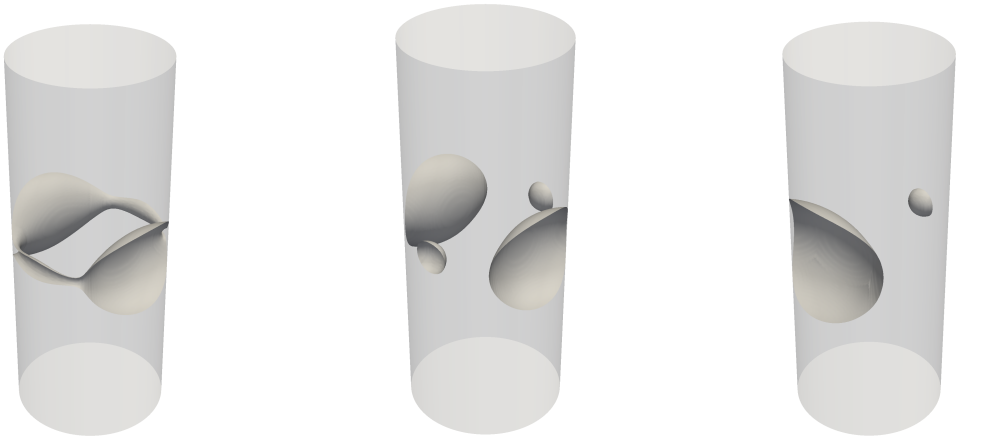

(d) Time = $0.31s$ (e) Time = $0.315s$ (f) Time = $1.5s$

Figure 5.20.: Contact Angle = 80°; Plug To Droplet; Initial Volume = 2.0; Transition Volume = 0.79; Transition Time = $0.094s$. Iso-surfaces are plotted at $\alpha = 0.5$ from the alpha field calculated by OpenFOAM.

as it nears the inlet patches. It is important to note that the initial volumes are different for each contact angle.

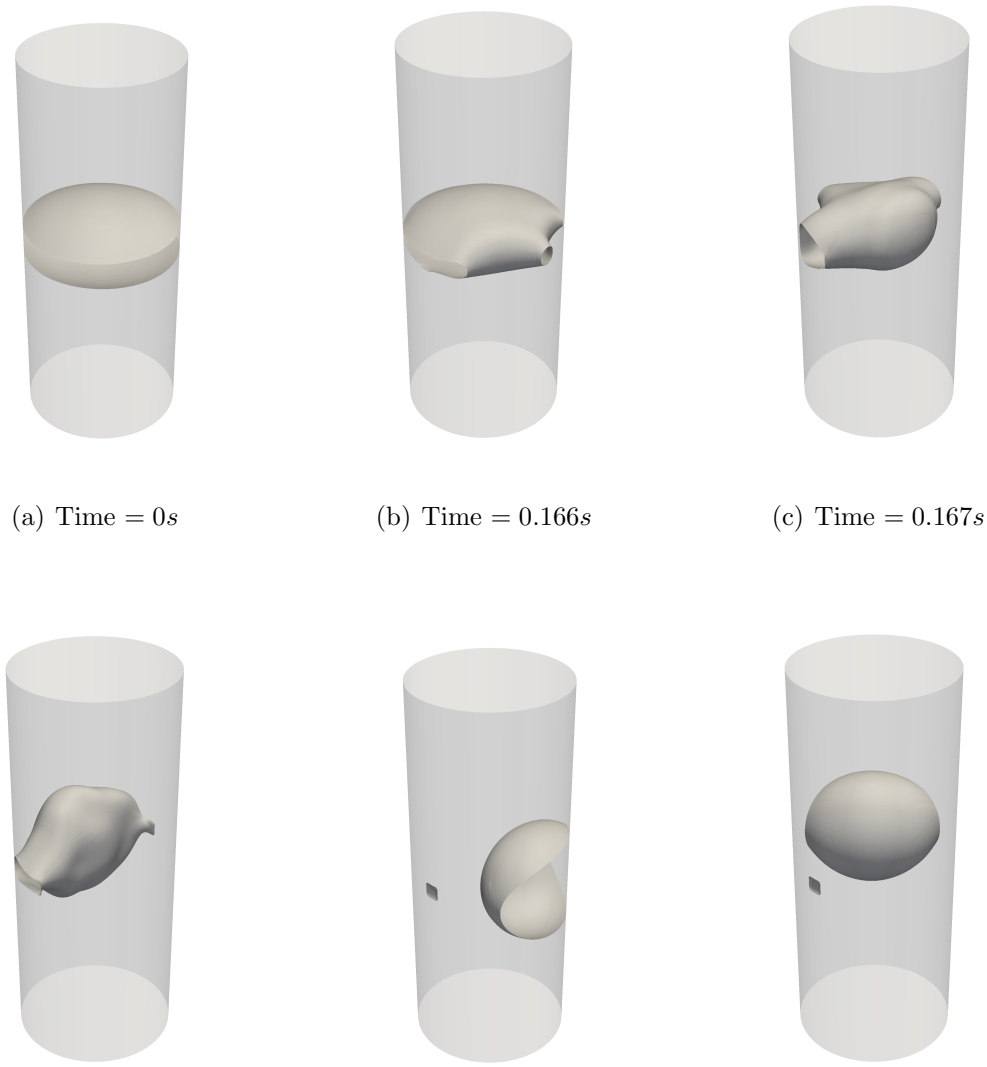

(a) Time = $0s$ (b) Time = $0.166s$ (c) Time = $0.167s$

(d) Time = $0.169s$ (e) Time = $0.2s$ (f) Time = $1.2s$

Figure 5.21.: Contact Angle = 120°; Plug To Droplet; Initial Volume = 2.0; Transition Volume = 1.34; Transition Time = $0.023s$. Iso-surfaces are plotted at $\alpha = 0.5$ from the alpha field calculated by OpenFOAM.

The second jump in energy seen for a few contact angles such as for $\theta = 60°$ are due to the merging of multiple droplets into a single droplet due to the moving

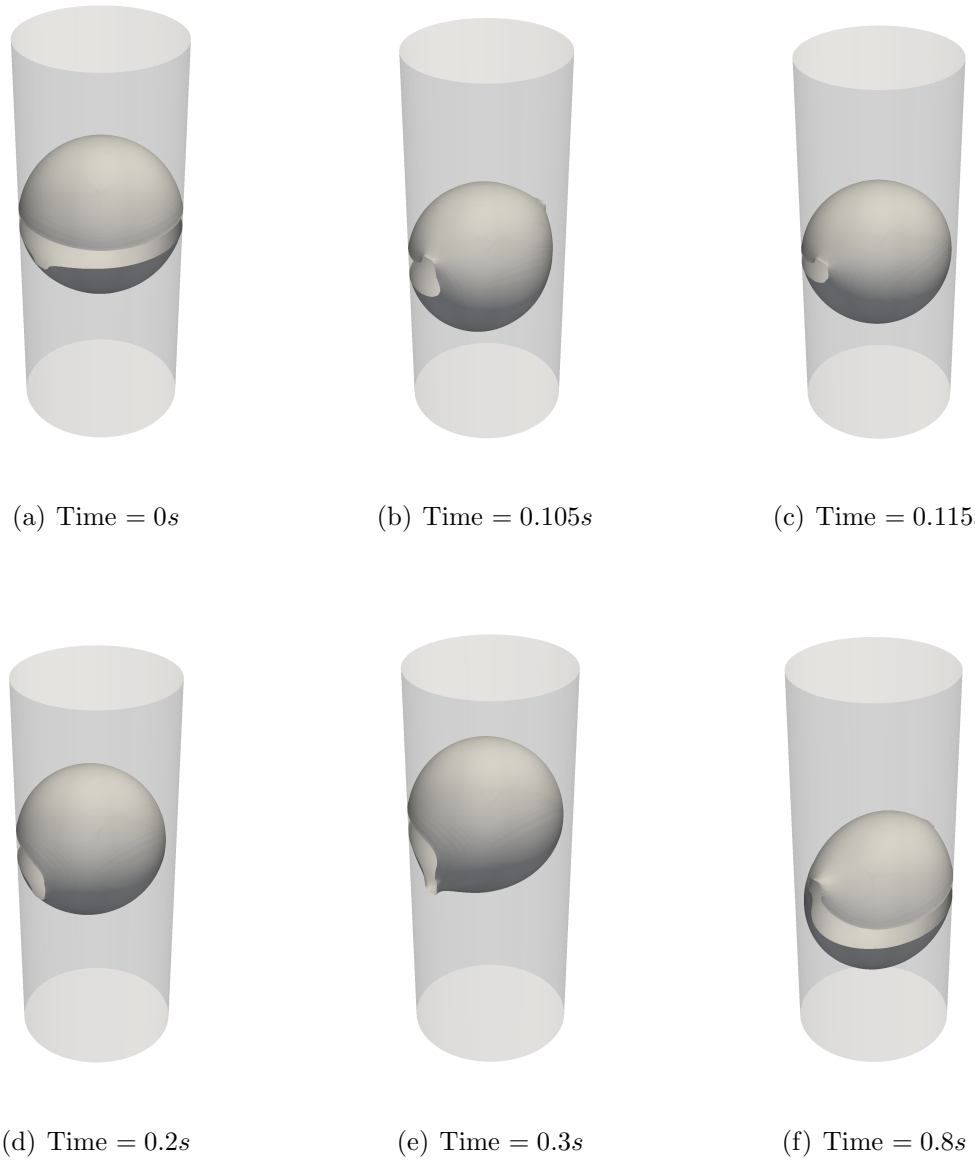

(a) Time = $0s$ (b) Time = $0.105s$ (c) Time = $0.115s$

(d) Time = $0.2s$ (e) Time = $0.3s$ (f) Time = $0.8s$

Figure 5.22.: Contact Angle = 170°; Plug To Droplet; Initial Volume = 4.0; Transition Volume = 3.64; Transition Time = ∞. Iso-surfaces are plotted at $\alpha = 0.5$ from the alpha field calculated by OpenFOAM. Shows droplet pinned to the inlet patch and being stretched.

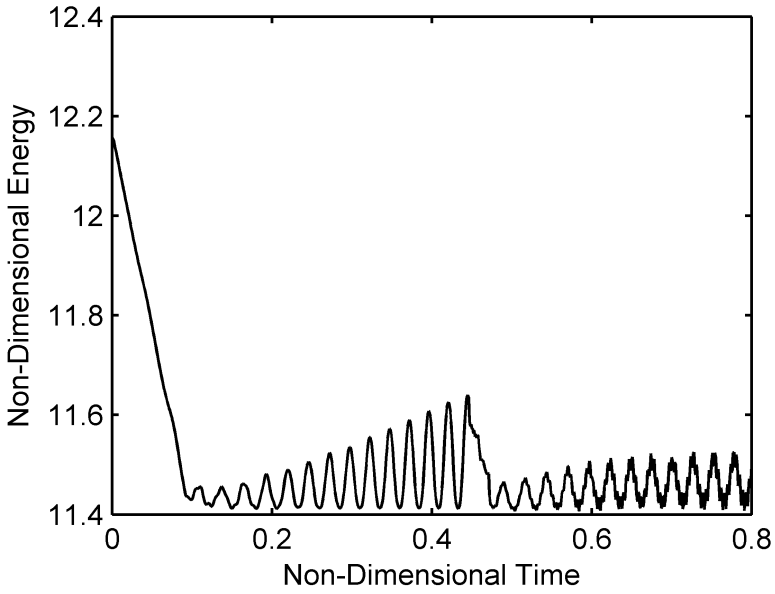

Figure 5.23.: Non-Dimensional energy with time for plug to droplet transitions at $\theta = 170°$. Initial Volume = 4.0. Transition Volume = 3.64. The oscillations are because of the movement of the droplet restricted by the inlet patch.

droplets. Transition times are calculated only to the next immediate stable state and does not include the time for such droplet merging. The transition times for both the types of transitions are plotted in Figure 5.26. This gives us an estimate for the magnitude of transition times that can be expected.

The next stage in this study is to look at the effect of fluid properties on non-dimensional transition times and energy variation. This is observed by looking at plug to droplet transitions for two different fluids for the denser phase. In the first case the denser phase has a density of $1000kg/m^3$ and in the second case the density is $2500kg/m^3$. The two cases are identical in every other aspect. The contact angle (θ) is 60° and the initial plug volume is $v = 2.0$. It is seen that the transition for the case with the higher density happens at a slightly lower volume than the other. The non-dimensional transition times for the two cases are compared. For the case with the denser liquid the transition time was calculated to be 0.076 compared to 0.033

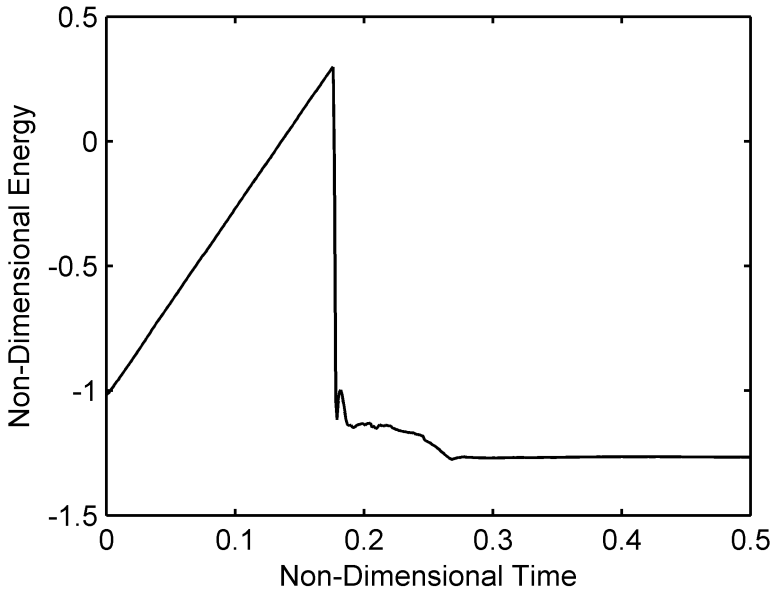

Figure 5.24.: Non-Dimensional energy with time for plug to droplet transitions at $\theta = 20°$. Initial Volume = 3.0. Transition Volume = 2.28.

for the case with the less denser liquid. This can also be seen clearly from the energy variation, where the energy changes much slower in the case of the denser liquid. This is in line with what we would expect as for the same volume there is more mass to move to get to the stable state. However further experiments are needed to completely study the effect of such changes in fluid properties on transition parameters.

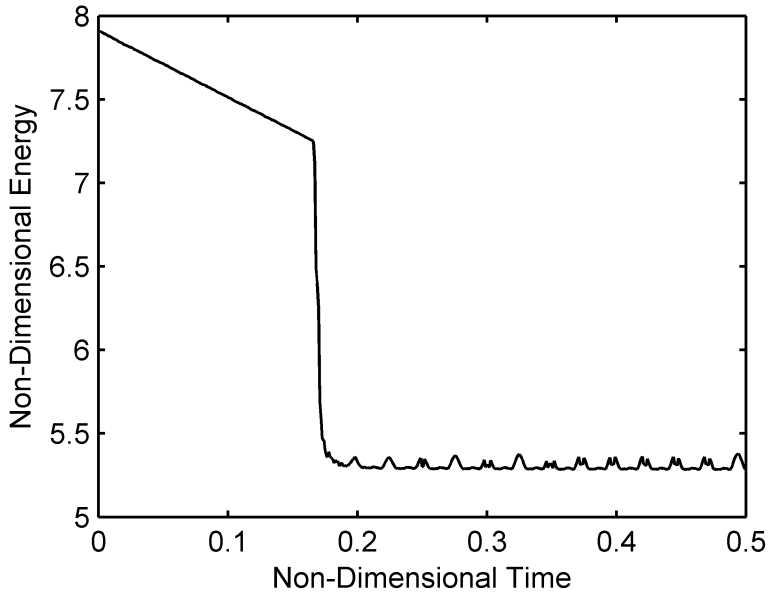

Figure 5.25.: Non-Dimensional energy with time for plug to droplet transitions at $\theta = 120°$. Initial Volume = 2.0. Transition Volume = 1.34.

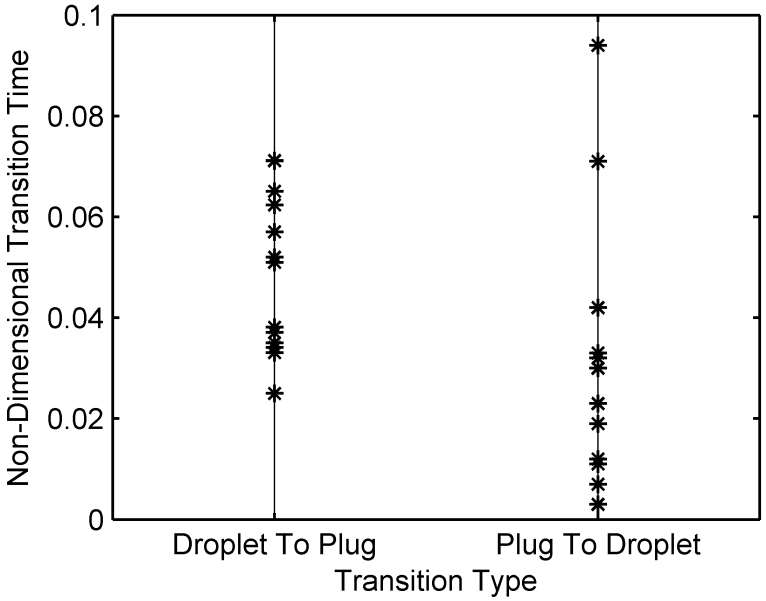

Figure 5.26.: Non-Dimensional transition times for both the droplet to plug and plug to droplet transitions.

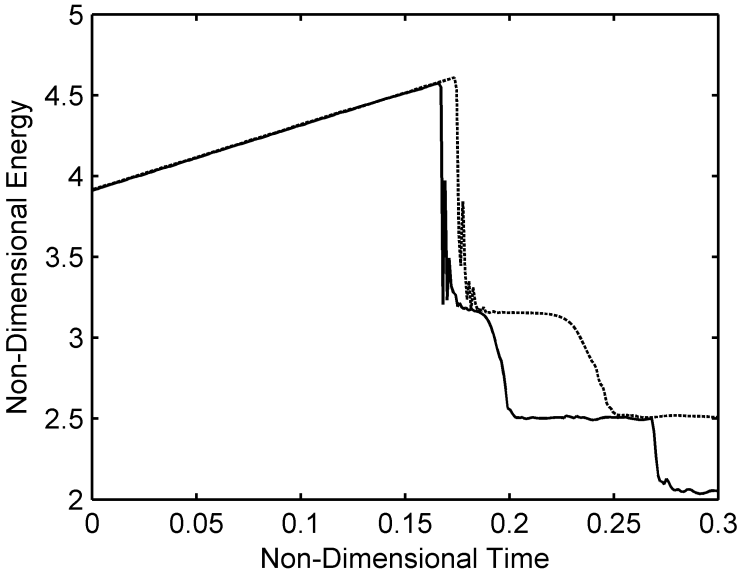

Figure 5.27.: Non-Dimensional energy with time for plug to droplet transitions at $\theta = 60°$. The solid line is for the case with a density of $1000kg/m^3$ and the dashed line is for the case with fluid density $2500kg/m^3$ for the obstructing phase.

6. CONCLUSIONS AND FUTURE WORK

6.1 Conclusions

The two-phase problem where one of the phases obstructs the other is a very important phenomenon in a wide range of fields, from medicine to space propulsion. Previously, efforts have been made to compute equilibrium static solutions in a cylindrical tube. Such solutions were also computed in a bent tube and a laterally compressed tube. It is known that in the case of a circular cylindrical tube there are three possible equilibrium solutions, viz. droplet, plug, and annulus. In this study, the transitions between these stable states actuated by small liquid volume changes have been computed. This is important as the breakup of an interface could adversely affect the operation of a system.

Two main transitions, droplet to plug and plug to droplet, which cover a large portion of the volume-contact angle space have been studied. The computational solver interFoam which is a part of the OpenFOAM package was used for this purpose. The volumes are all less than six times the cube of the radius of the tube. At all higher volumes only the plug solution exists. In order to establish the accuracy of interFoam in such a study, static equilibrium solutions at different volumes and contact angles were compared with the corresponding solution computed by Surface Evolver. Particularly the non-dimensional energy and the non-dimensional free surface areas were compared between the two methods. It is seen that for small contact angles the free surface areas computed by OpenFOAM are a little less than the ones from Surface Evolver. However the energies are a very good fit between the two. As the contact angle increases to the mid contact angles, the solutions are much closer and are more comparable. It was also seen that the equilibrium shape was dependent on the initial definition of the alpha field from where the shape is allowed to evolve.

The transitions were computed for θ from 10° to 170° in increments of 10°. The grid independence was evaluated by comparing the non-dimensional energies and the non-dimensional transition volumes. It is found that the transition from a droplet to a plug is independent of the grid resolution while the transition from a plug to a droplet was highly dependent on the grid resolution. This stems from the fact that a large number of cells are needed to properly resolve the small volumes as the two free surfaces of the plug come closer to each other as volume decreases. On the other hand increasing the grid resolution by increasing the number of cells increases the computational cost. Thus a balance between accuracy and computational cost is important in these computations.

The droplet to plug transitions were observed by increasing the volume of the obstructing phase through an inlet patch. Three main modes of transitions were observed depending on the contact angle. For lower contact angles, the droplet reaches the maximum angular extent possible in the tube when the contact lines touch. In the case of higher angles, the transitions occur much before the angular extent reaches 2π. Instead here the droplet grows until it completely obstructs the tube and then transitions. The third mode of transition is observed in contact angles greater than 130°, where the droplet grows in size and the free surface of the droplet touches the wall of the tube. It is seen that transitions occur at a volume greater than the maximum volume of existence in the case of acute angles. The exact source of this difference is not apparent from this study and further investigation is necessary with both these methods to reduce this difference.

The plug to droplet transitions on the other hand were observed by decreasing the volume of the obstructing phase. Two modes of transitions were found, and they are dependent on where the end caps meet which in turn depends on the contact angle. The transition volumes were consistently higher than the minimum volume of existence for a plug calculated analytically. The effect of fluid properties on the transition times is also briefly studied. It was seen that the transition times increase as the fluid density increases, which is as expected. Despite all the problems commonly

associated with the multi-phase solver in OpenFOAM, e.g. parasitic currents, it does a pretty good job at estimating these transitions. It would be interesting to look at other interface tracking algorithms and also validate these with experimental data which would cement our understanding of such a type of problem.

6.2 Future Work

There is always scope to improve on or expand a study to delve further into the problem. A few interesting considerations for further work related to the problem are listed in this section. Firstly, it would be interesting to find exactly the source of the difference between the computations from Surface Evolver and OpenFOAM. An alternative interface tracking algorithm such as the CLSVOF method or a higher order Volume of Fluid Method (PROST) could be used to compute with higher accuracy. This can be implemented in OpenFOAM under the framework of the interFoam solver. It is a bit more complicated and time consuming to write, evaluate and validate the new algorithm but could potentially provide a more accurate transition study. An experimental study would also help us better understand and establish the accuracy of the transitions computed in this study. Since the experiments under the Reduced Gravity Education Flight Program were not conclusive, the only other way of conducting experiments in stable microgravity is in the International Space Station. Such an experiment would benefit further exploration in this field and also potentially help validate either the Surface Evolver computations or the transitions predicted by OpenFOAM. Spurious currents have been prevalent in VOF methods since its inception and even in the current version of OpenFOAM these non-physical velocities exist at the interface. Though there have been some developments to reduce these velocities they have not been yet implemented in mainstream distributions. It is also necessary to see if there is any change in the transition behavior if the size of the inlet patches are changed, as in some cases the contact lines of the end caps seem to get pinned to the inlet patches.

The same procedure can be easily adapted to study transitions between the different solutions in the case of other tube geometries. For example the static equilibrium study for the bent tube and the laterally compressed tube can now be extended to study transitions using OpenFOAM. It would also be interesting to further study the effect of fluid properties on the transition times for a whole range of contact angles and properties.

REFERENCES

REFERENCES

[1] D.R. Frazer, P.W. Stengel, and K.C. Weber. Meniscus formation in airways of excised rat lungs. *Respiration Physiology*, 36(2):121 – 129, 1979.

[2] P.T. Macklem. Airway obstruction and collateral ventilation. *Physiological Reviews*, 51(2):368–436, 1971.

[3] W.G. Lindsley, S.H. Collicott, G.N. Franz, B. Stolarik, W. McKinney, and D.G. Frazer. Asymmetric and axisymmetric constant curvature liquid-gas interfaces in pulmonary airways. *Annals of Biomedical Engineering*, 33(3):365–375, JAN 2005.

[4] D. Zube, P. Lichon, D. Cohen, D. Lichtin, J. Bailey, and N. Chilelli. Initial on-orbit performance of hydrazine arcjets on A2100 satellites. *35th Joint Propulsion Conference and Exhibit*, 2015/02/09 1999.

[5] D. Zube and D. Cohen. Improvements to hydrazine arcjet system performance and operational robustness against gas ingestion. *37th Joint Propulsion Conference and Exhibit*, 2015/02/09 2001.

[6] NASA - International Space Station status report: SS05-001. Online at: `http://www.nasa.gov/home/hqnews/2005/jan/HQ_ss05001_station_status_prt.htm`.

[7] J. Oberg. Oxygen has its ups and downs on space station, 2005. Online at: `http://www.nbcnews.com/id/6800245/ns/technology_and_science-space/t/oxygen-has-its-ups-downs-space-station/#.VQ34JkIXmyP`.

[8] Extravehicular mobility unit systems safety review panel review for the I-141 gas trap critical item list (CIL). Online at: `http://www.jsc.nasa.gov/news/columbia/nsts08399/book07/part2/141fm01.pdf`.

[9] NASA - Columbia Accident Investigation Documents. Online at: `http://www.nasa.gov/centers/johnson/news/shuttle/columbia.html`.

[10] D. Belder. Microfluidics with droplets. *Angewandte Chemie International Edition*, 44(23):3521–3522, 2005.

[11] L.A. Slobozhanin, J.I.D. Alexander, and A.I. Fedoseyev. Shape and stability of doubly connected axisymmetric free surfaces in a cylindrical container. *Physics of Fluids*, 11:3668, 1999.

[12] S.H. Collicott, W.G. Lindsley, and D.G. Frazer. Zero-gravity liquid-vapor interfaces in circular cylinders. *Physics of Fluids*, 18(8), AUG 2006.

[13] K.A. Brakke. The surface evolver. *Experimental Mathematics*, 1(2), 1992.

[14] J.P. Braun. Zero gravity two-phase stability solutions of droplets in a bent circular cylinder. Master's thesis, Purdue University, 2008.

[15] J.M. Jaron. Static two-phase solutions in a laterally-compressed circular cylinder in zero gravity. Master's thesis, Purdue University, 2007.

[16] OpenFoam. *OpenFOAM. The Open Source CFD Toolbox. User Guide*. Free Software Foundation, Inc., 2009.

[17] S.M. Damián. Description and utilization of interfoam multiphase solver.

[18] W. Malalasekera and H.K. Versteeg. *An Introduction to Computational Fluid Dynamics : The Finite Volume Method*. Pearson Education Ltd., 2007.

[19] M. Perić and J.H. Ferziger. *Computational methods for fluid dynamics*. Springer, Berlin, 2002.

[20] H. Jasak. *Error analysis and estimation for the finite volume method with applications to fluid flows*. PhD thesis, Imperial College of Science, Technology and Medicine, 1996.

[21] H. Rusche. *Computational fluid dynamics of dispersed two-phase flows at high phase fractions*. PhD thesis, Imperial College of Science, Technology and Medicine, 2003.

[22] S.E. Norris. *A Parallel Navier Stokes Solver for Natural Convection and Free Surface Flow*. PhD thesis, University of Sydney, 2000.

[23] J.U. Brackbill, D.B. Kothe, and C. Zemach. A continuum method for modeling surface tension. *Journal of Computational Physics*, 100(2):335–354, 1992.

[24] T.Y. Hou, J.S. Lowengrub, and M.J. Shelley. Boundary integral methods for multicomponent fluids and multiphase materials. *Journal of Computational Physics*, 169(2):302–362, 2001.

[25] L.C. Wrobel and H. Power. *Boundary integral methods in fluid mechanics*. Computational Mechanics Publications, Southampton, UK, 1995.

[26] S. Shin and D. Juric. Modeling three-dimensional multiphase flow using a level contour reconstruction method for front tracking without connectivity. *Journal of Computational Physics*, 180(2):427–470, 2002.

[27] C.S. Peskin. Numerical analysis of blood flow in the heart. *Journal of Computational Physics*, 25(3):220–252, 1977.

[28] C.S. Peskin and D.M. McQueen. A general method for the computer simulation of biological systems interacting with fluids. *Symposia Of The Society For Experimental Biology*, 49:265, 1995.

[29] D. Juric and G. Tryggvason. Computations of boiling flows. *International Journal of Multiphase Flow*, 24(3):387–410, 1998.

[30] S. Osher and J.A. Sethian. Fronts propagating with curvature-dependent speed: Algorithms based on hamilton–jacobi formulations. *Journal of Computational Physics*, 79(1), 1988.

[31] J.A. Sethian and P. Smereka. Level set methods for fluid interfaces. *Annu. Rev. Fluid Mech.*, 35(1 1):341–372, 2003.

[32] J. Kim. Phase-field models for multi-component fluid flows. *Commun. Comput. Phys*, 2012.

[33] D.M. Anderson, G.B. McFadden, and A.A. Wheeler. Diffuse-interface methods in fluid mechanics. *Annu. Rev. Fluid Mech*, 30(1 1):139–165, 1998.

[34] C.W. Hirt and B.D. Nichols. Volume of fluid (VOF) method for the dynamics of free boundaries. *Journal of Computational Physics*, 39(1):201–225, 1981.

[35] E.G. Puckett, A.S. Almgren, J.B. Bell, D.L. Marcus, and W.J. Rider. A high-order projection method for tracking fluid interfaces in variable density incompressible flows. *Journal of Computational Physics*, 130(2):269–282, 1997.

[36] Y. Renardy and M. Renardy. PROST: A parabolic reconstruction of surface tension for the volume-of-fluid method parabolic reconstruction of surface tension for the volume-of-fluid method. *Journal of Computational Physics*, 183(2):400–421, 2002.

[37] M. Sussman and E.G. Puckett. A coupled level set and volume-of-fluid method for computing 3d and axisymmetric incompressible two-phase flows. *Journal of Computational Physics*, 162(2):301–337, 2000.

[38] D. Gerlach, G. Tomar, G. Biswas, and F. Durst. Comparison of volume-of-fluid methods for surface tension-dominant two-phase flows. *International Journal of Heat and Mass Transfer*, 49(3–4):740–754, 2 2006.

[39] Z. Wang, J. Yang, and F. Stern. Comparison of particle level set and CLSVOF methods for interfacial flows. *46th AIAA Aerospace Sciences Meeting and Exhibit*, 2015/02/22 2008.

[40] O. Ubbink. *Numerical prediction of two fluid systems with sharp interfaces*. PhD thesis, Imperial College, London, 1997.

[41] S.M. Damian. *An Extended Mixture Model for the Simultaneous Treatment of Short and Long Scale Interfaces*. PhD thesis, Universidad Nacional del Litoral, Santa Fe, Argentina, 2013.

[42] R.I. Issa. Solution of the implicitly discretised fluid flow equations by operator-splitting. *Journal of Computational Physics*, 62(1):40 – 65, 1986.

[43] P. Lopes. *Free-surface flow interface and air-entrainment modelling using OpenFOAM*. PhD thesis, Universidade De Coimbra, 2013.

[44] B. Lafaurie. Modelling merging and fragmentation in multiphase flows with SURFER. *Journal of Computational Physics*, 113(1), 1994.

[45] D. Jamet, D. Torres, and J.U. Brackbill. On the theory and computation of surface tension: The elimination of parasitic currents through energy conservation in the second-gradient method. *Journal of Computational Physics*, 182(1):262–276, 2002.

[46] S. Popinet and S. Zaleski. A front-tracking algorithm for accurate representation of surface tension. *International Journal for Numerical Methods in Fluids*, 30(6):775–793, 1999.

[47] S.S. Deshpande, L. Anumolu, and M.F. Trujillo. Evaluating the performance of the two-phase flow solver interfoam. *Computational Science & Discovery*, 5(1):014016, 2012.

[48] A.Q. Raeini, M.J. Blunt, and B. Bijeljic. Modelling two-phase flow in porous media at the pore scale using the volume-of-fluid method. *Journal of Computational Physics*, 231(17):5653–5668, 2012.

[49] C. Galusinski and P. Vigneaux. On stability condition for bifluid flows with surface tension: Application to microfluidics. *Journal of Computational Physics*, 227(12):6140–6164, 2008.

[50] D.W. Langbein. *Capillary surfaces: shape-stability-dynamics, in particular under weightlessness*. Number 178. Springer Science & Business Media, 2002.

APPENDIX

A. Additional Figures and Plots

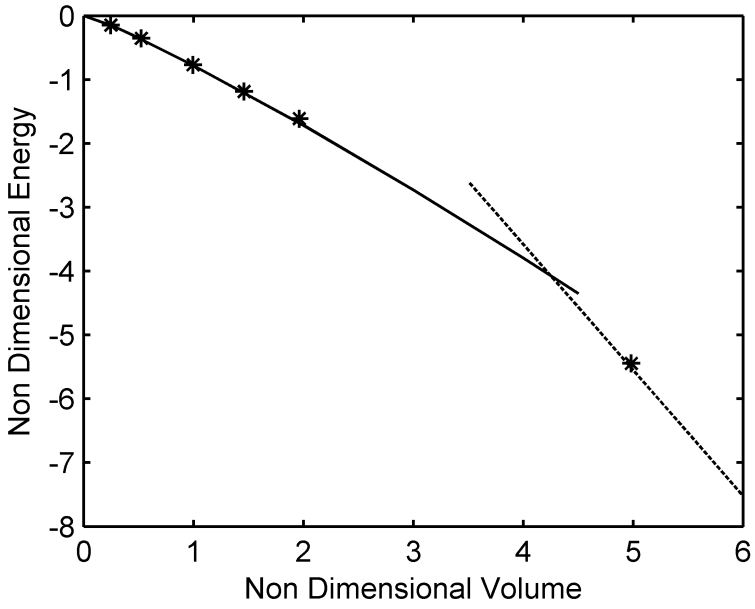

(a) Non-Dimensional Energy

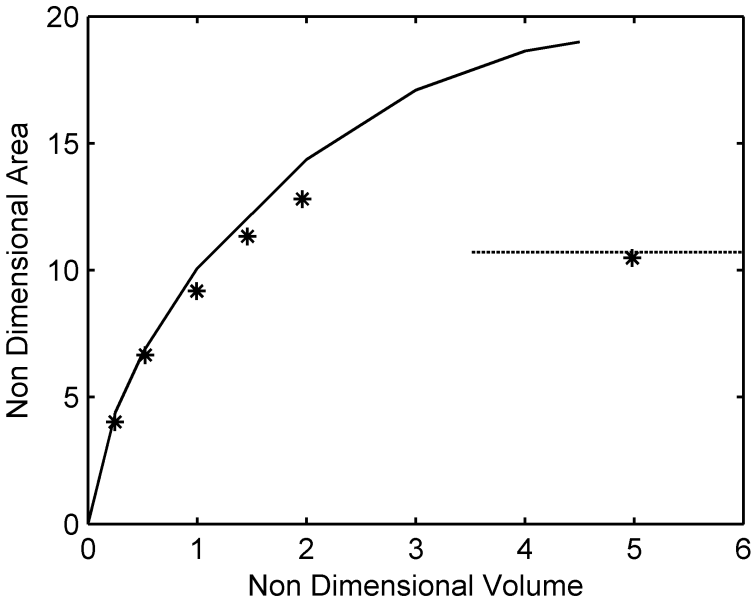

(b) Non-Dimensional Free Surface Area

Figure A.1.: Contact Angle = 10°; The solid line shows results from Surface Evolver and the markers are from OpenFOAM

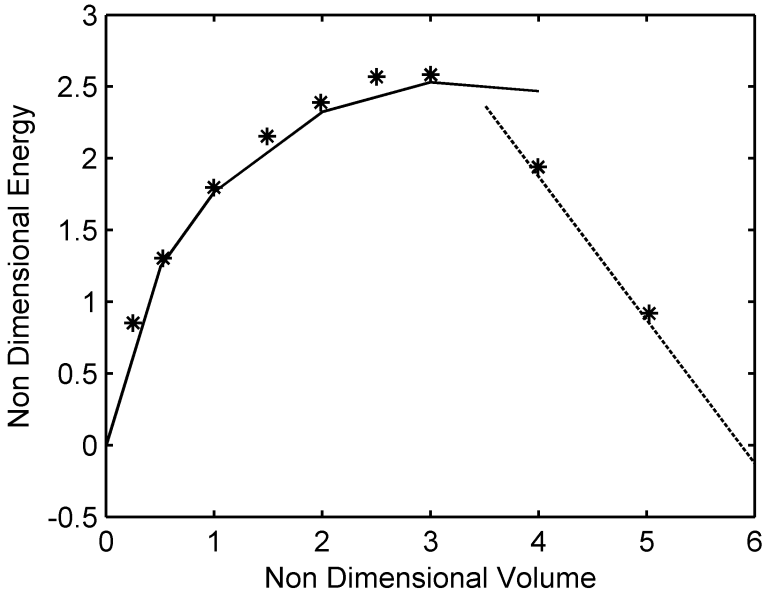

(a) Non-Dimensional Energy

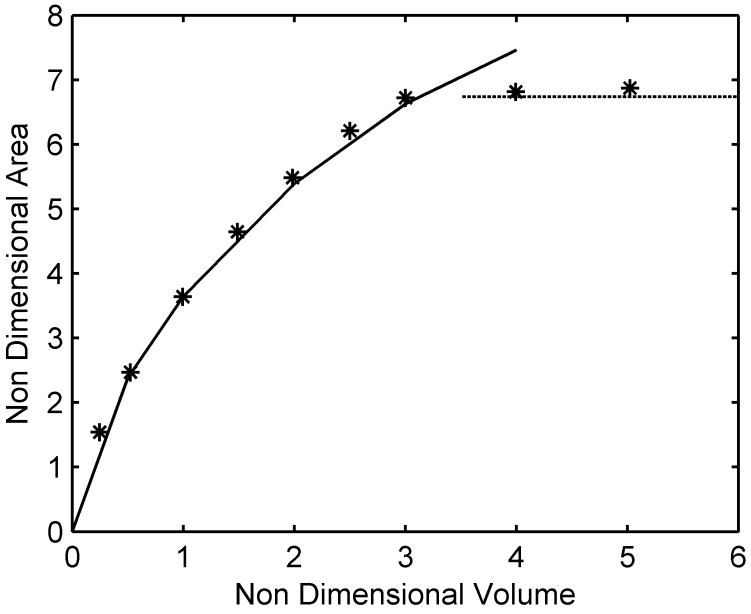

(b) Non-Dimensional Free Surface Area

Figure A.2.: Contact Angle = 60°; The solid line shows results from Surface Evolver and the markers are from OpenFOAM

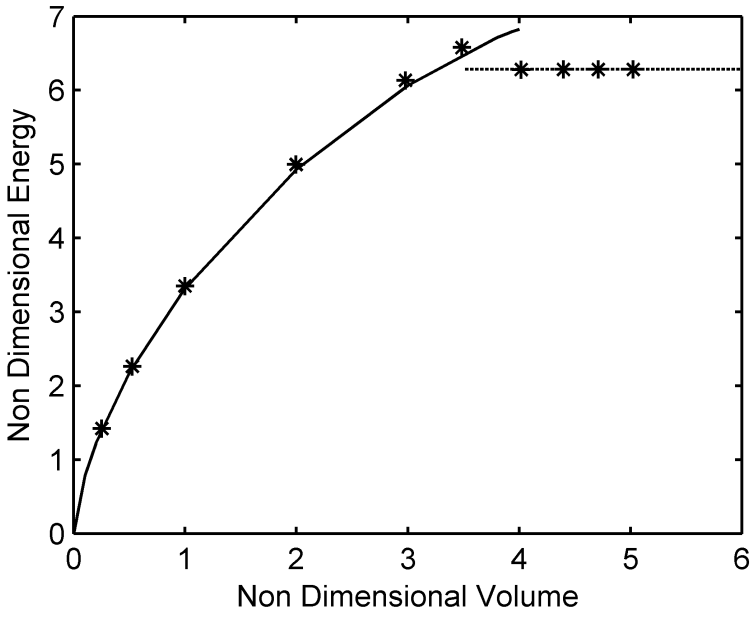

(a) Non-Dimensional Energy

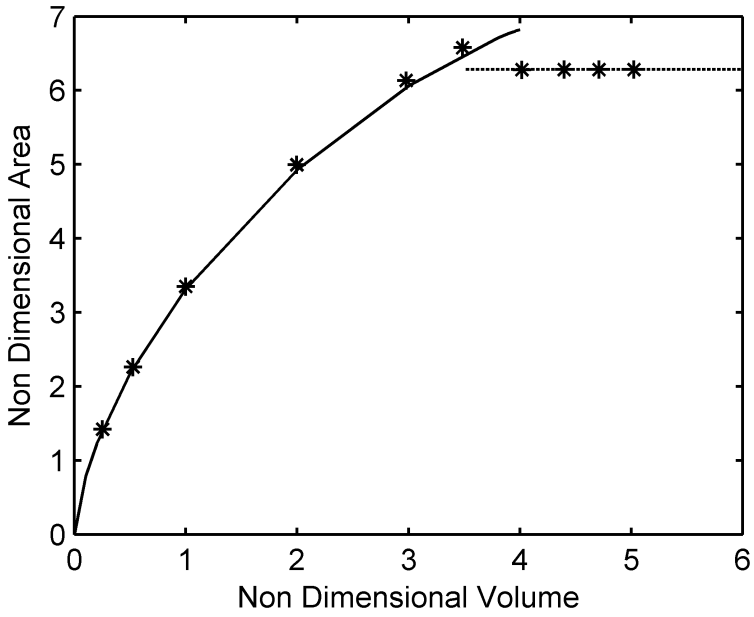

(b) Non-Dimensional Free Surface Area

Figure A.3.: Contact Angle = 90°; The solid line shows results from Surface Evolver and the markers are from OpenFOAM

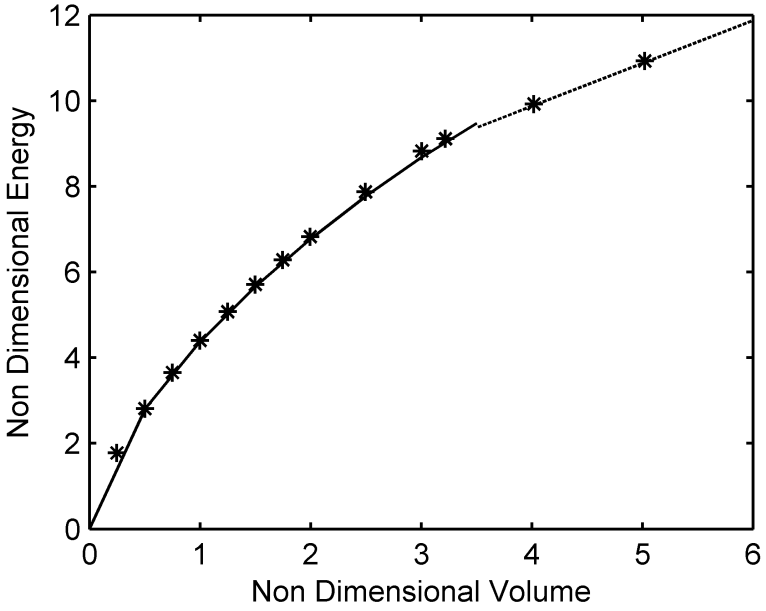

(a) Non-Dimensional Energy

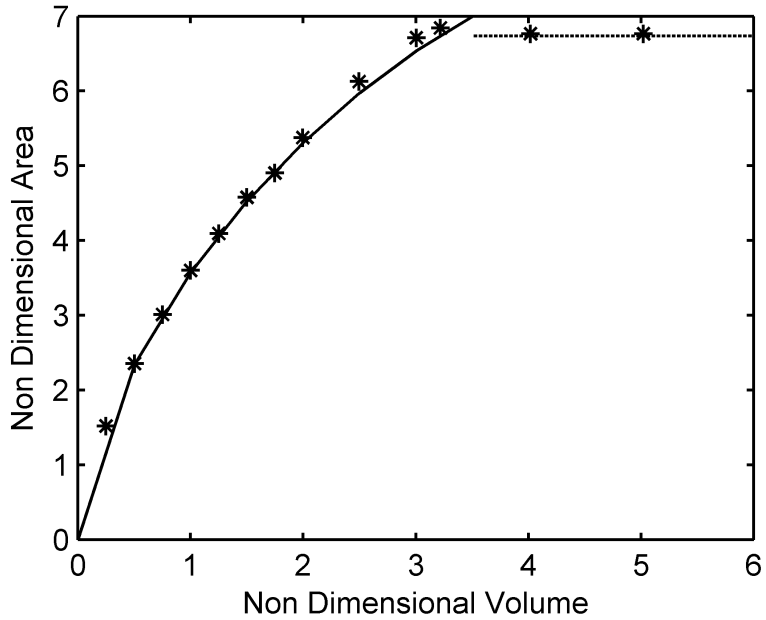

(b) Non-Dimensional Free Surface Area

Figure A.4.: Contact Angle = 120°; The solid line shows results from Surface Evolver and the markers are from OpenFOAM

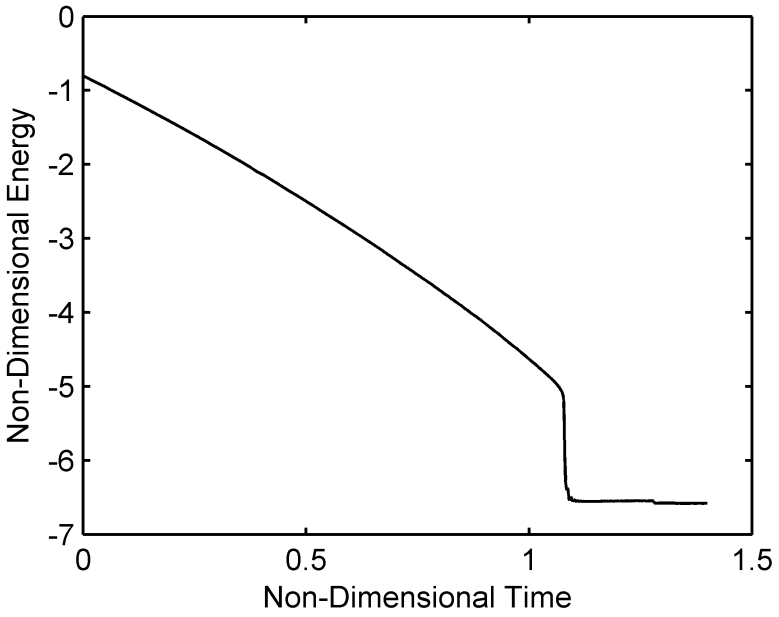

Figure A.5.: Non-Dimensional energy with time for droplet to plug transitions at $\theta = 20°$. Initial Volume = 1.65. Transition Volume = 5.96.

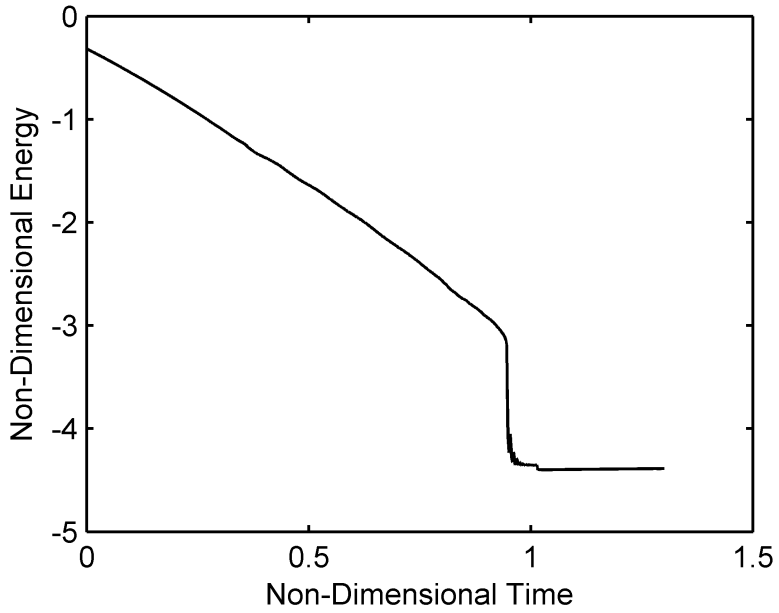

Figure A.6.: Non-Dimensional energy with time for droplet to plug transitions at $\theta = 30°$. Initial Volume = 2.0. Transition Volume = 5.38.

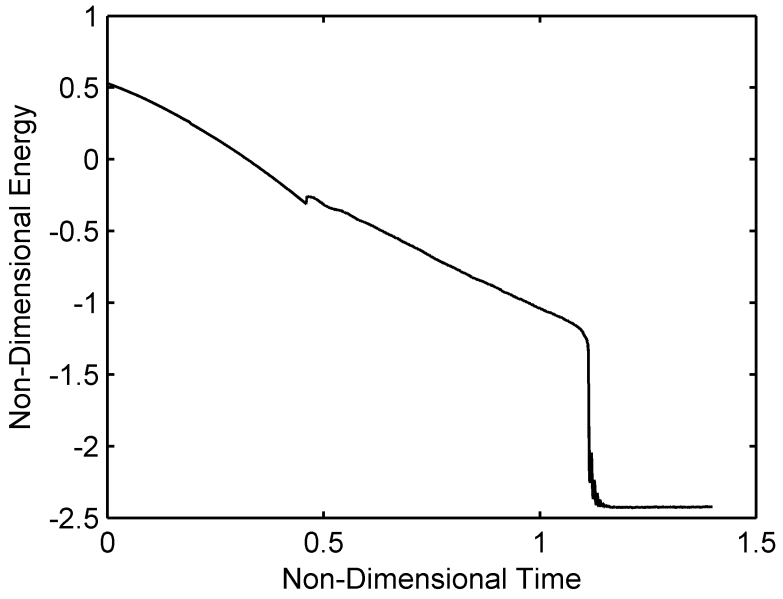

Figure A.7.: Non-Dimensional energy with time for droplet to plug transitions at $\theta = 40°$. Initial Volume = 2.0. Transition Volume = 5.05.

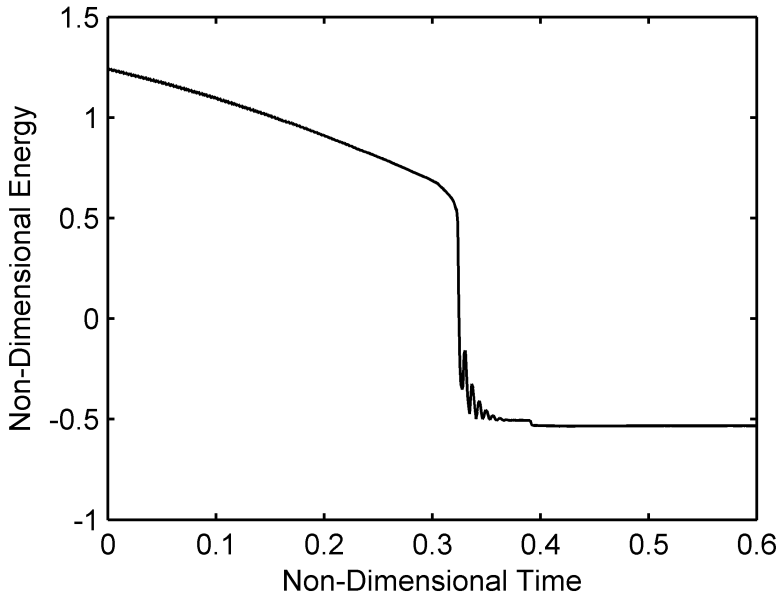

Figure A.8.: Non-Dimensional energy with time for droplet to plug transitions at $\theta = 50°$. Initial Volume = 3.5. Transition Volume = 4.79.

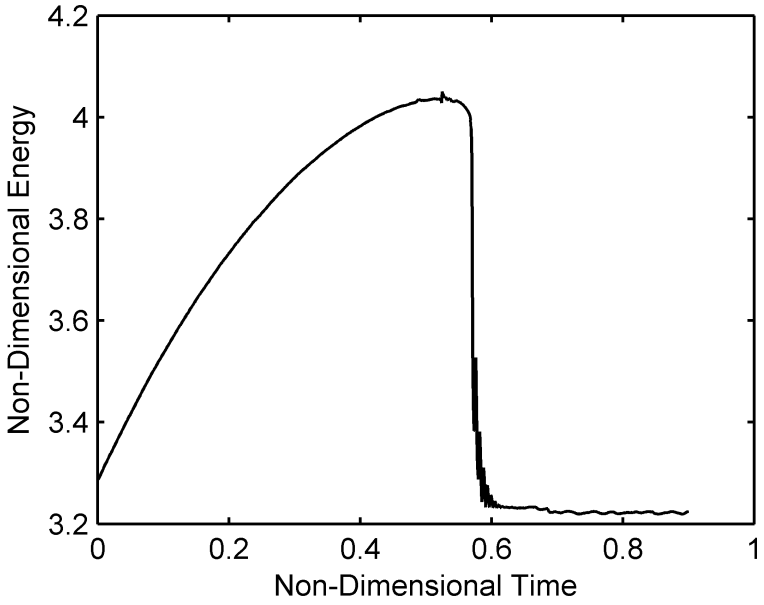

Figure A.9.: Non-Dimensional energy with time for droplet to plug transitions at $\theta = 70°$. Initial Volume = 2.0. Transition Volume = 4.28.

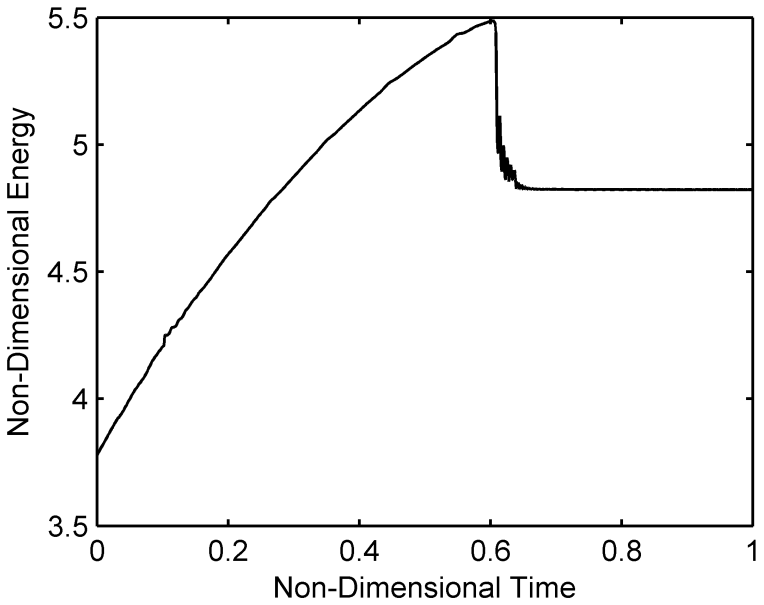

Figure A.10.: Non-Dimensional energy with time for droplet to plug transitions at $\theta = 80°$. Initial Volume = 1.65. Transition Volume = 4.09.

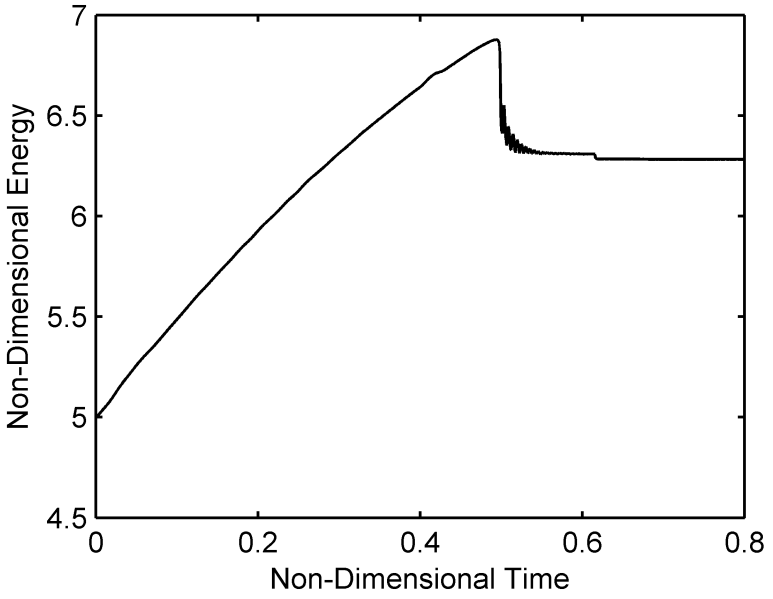

Figure A.11.: Non-Dimensional energy with time for droplet to plug transitions at $\theta = 90°$. Initial Volume = 2.0. Transition Volume = 3.99.

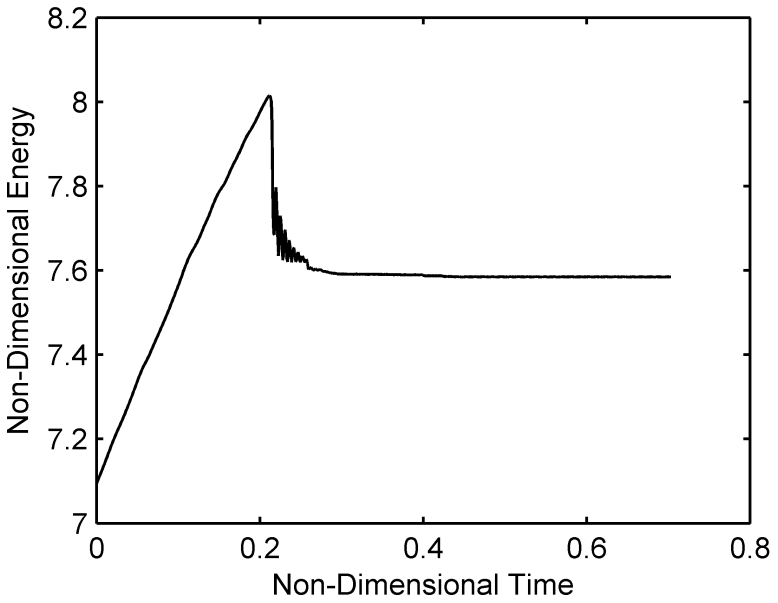

Figure A.12.: Non-Dimensional energy with time for droplet to plug transitions at $\theta = 100°$. Initial Volume = 3.0. Transition Volume = 3.86.

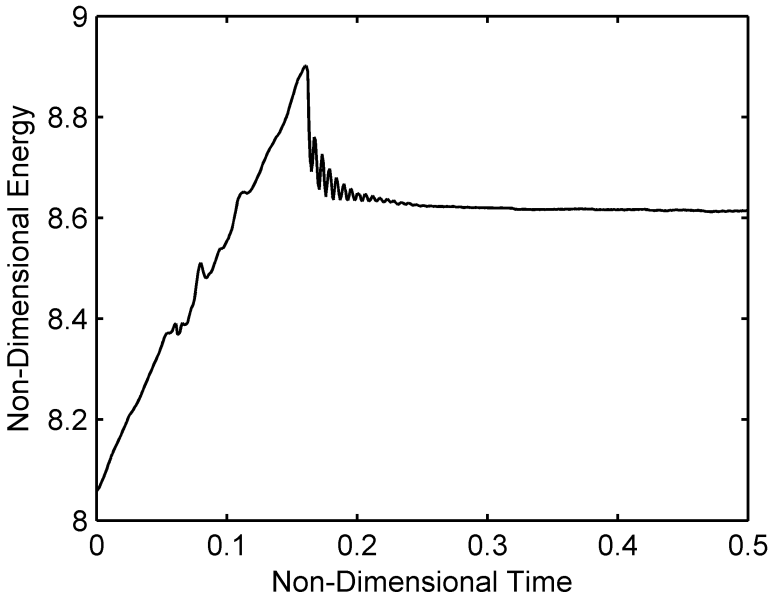

Figure A.13.: Non-Dimensional energy with time for droplet to plug transitions at $\theta = 110°$. Initial Volume = 3.0. Transition Volume = 3.65.

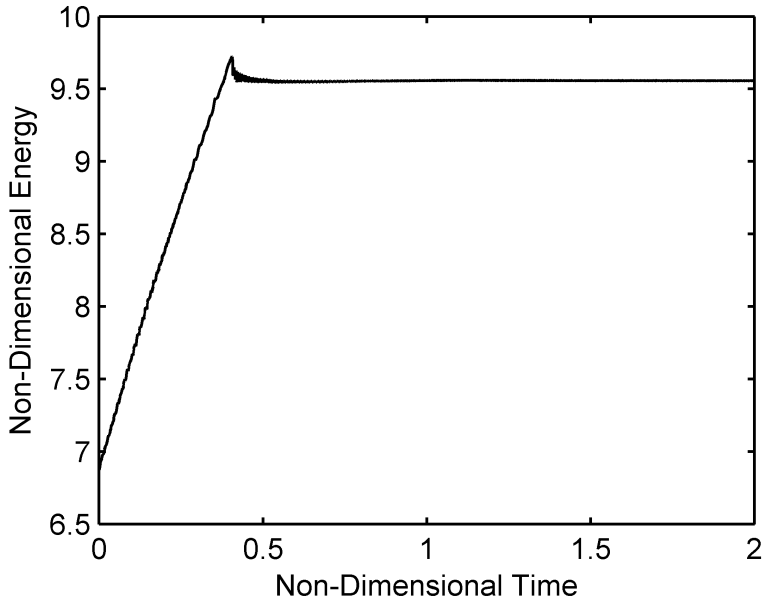

Figure A.14.: Non-Dimensional energy with time for droplet to plug transitions at $\theta = 120°$. Initial Volume = 2.0. Transition Volume = 3.63.

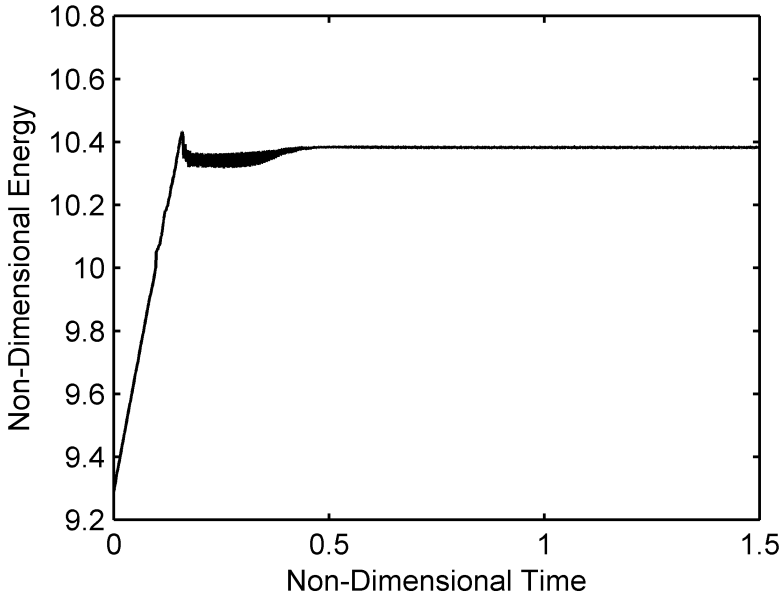

Figure A.15.: Non-Dimensional energy with time for droplet to plug transitions at $\theta = 130°$. Initial Volume = 3.0. Transition Volume = 3.65.

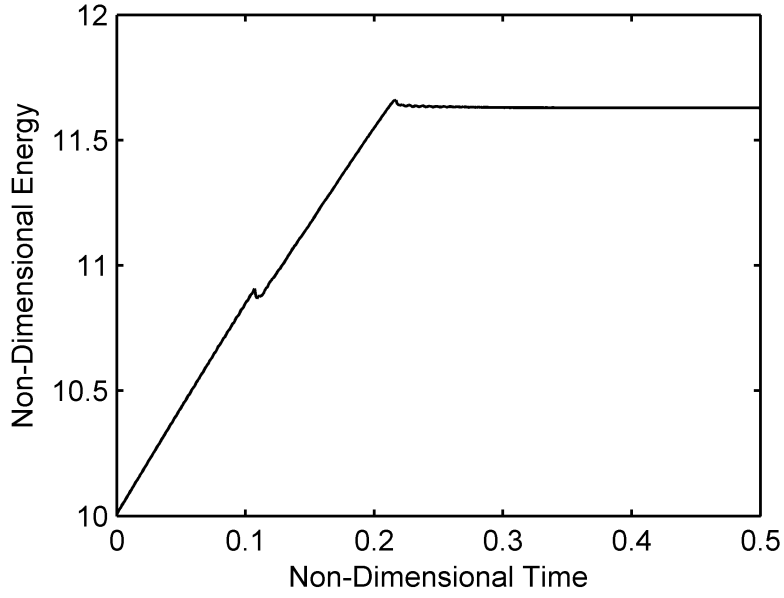

Figure A.16.: Non-Dimensional energy with time for droplet to plug transitions at $\theta = 150°$. Initial Volume = 3.0. Transition Volume = 3.87.

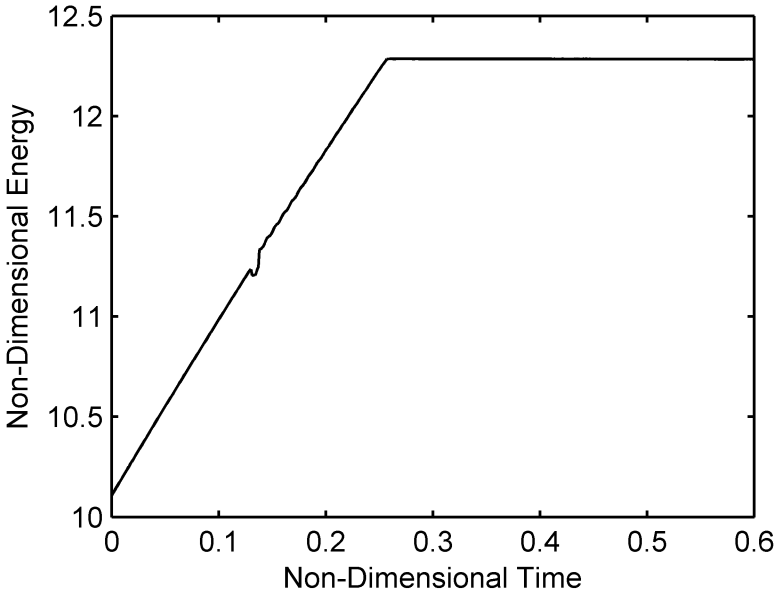

Figure A.17.: Non-Dimensional energy with time for droplet to plug transitions at $\theta = 170°$. Initial Volume = 3.0. Transition Volume = 4.03.

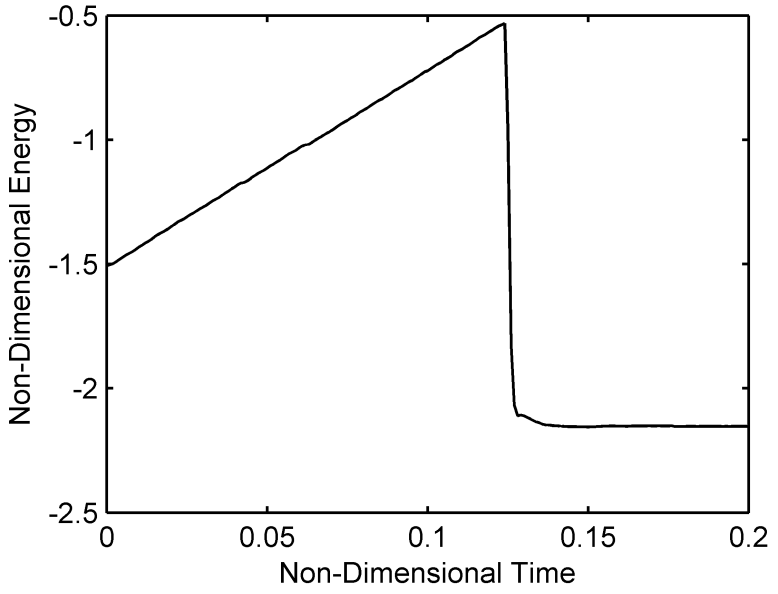

Figure A.18.: Non-Dimensional energy with time for plug to droplet transitions at $\theta = 10°$. Initial Volume = 3.0. Transition Volume = 2.49.

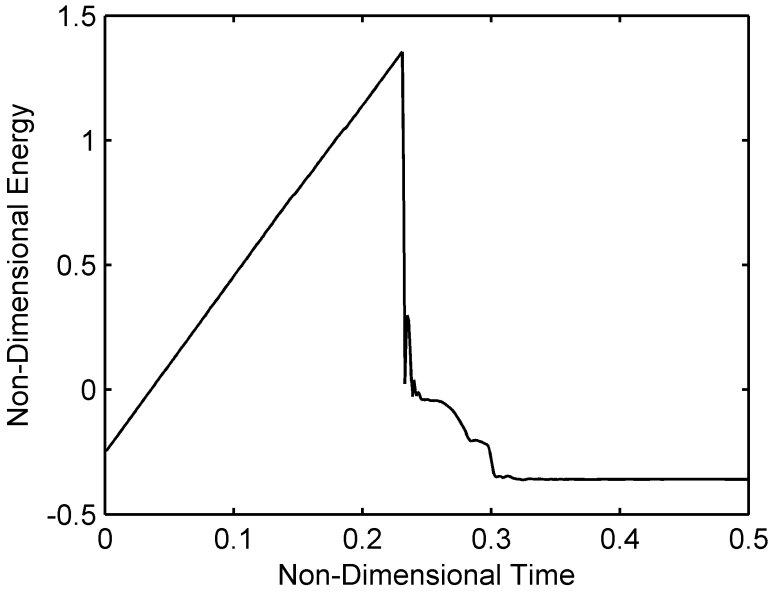

Figure A.19.: Non-Dimensional energy with time for plug to droplet transitions at $\theta = 30°$. Initial Volume = 3.0. Transition Volume = 2.07.

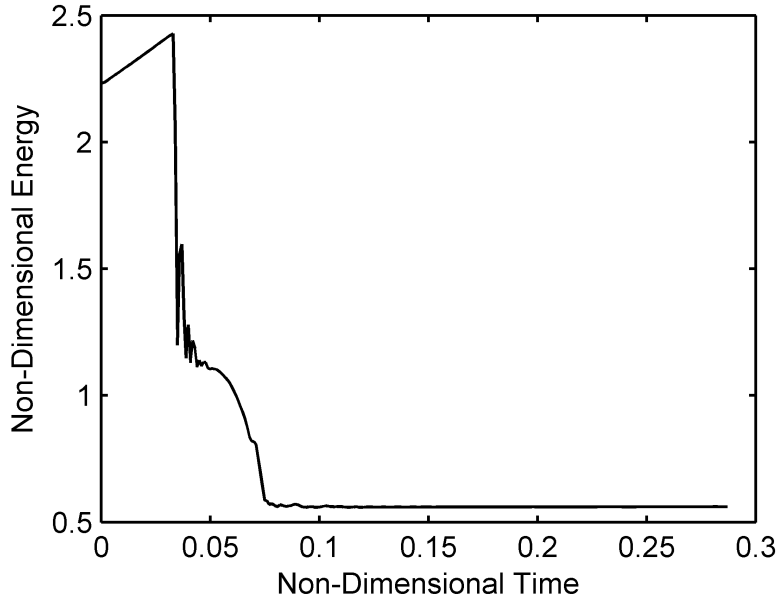

Figure A.20.: Non-Dimensional energy with time for plug to droplet transitions at $\theta = 40°$. Initial Volume = 2.0. Transition Volume = 1.86.

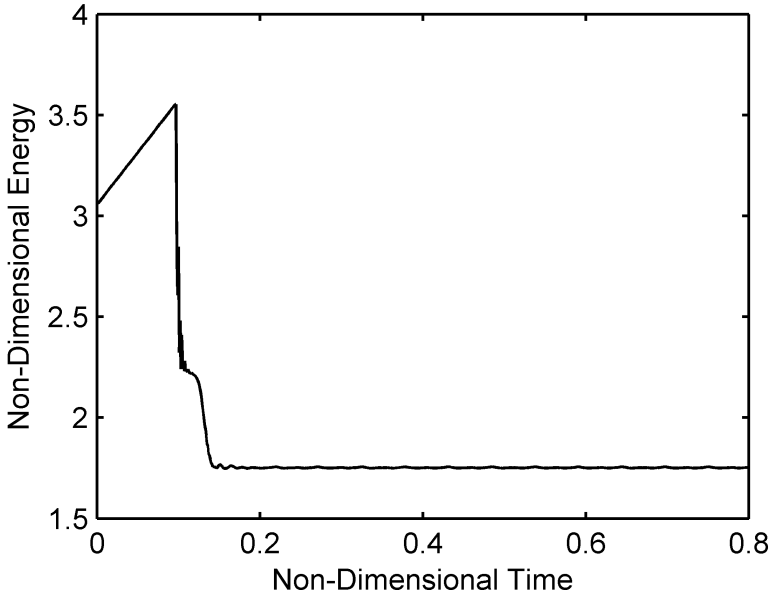

Figure A.21.: Non-Dimensional energy with time for plug to droplet transitions at $\theta = 50°$. Initial Volume = 2.0. Transition Volume = 1.61.

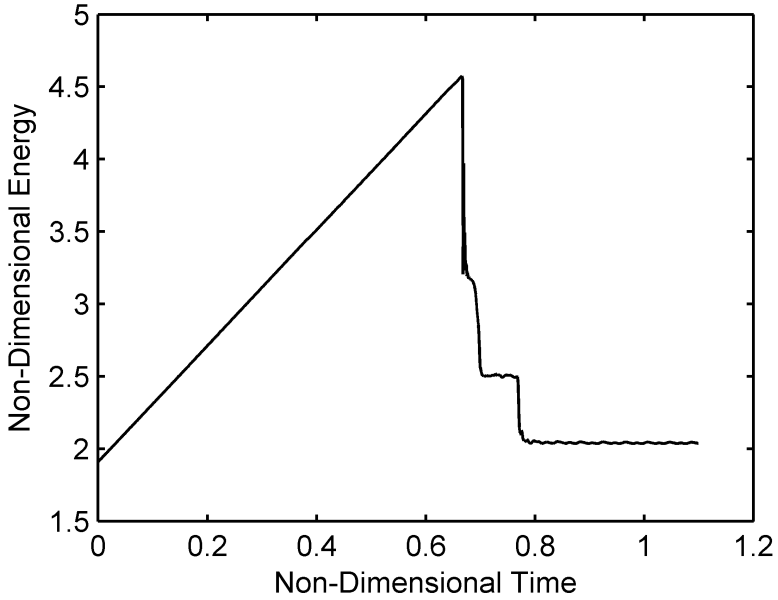

Figure A.22.: Non-Dimensional energy with time for plug to droplet transitions at $\theta = 60°$. Initial Volume = 4.0. Transition Volume = 1.33.

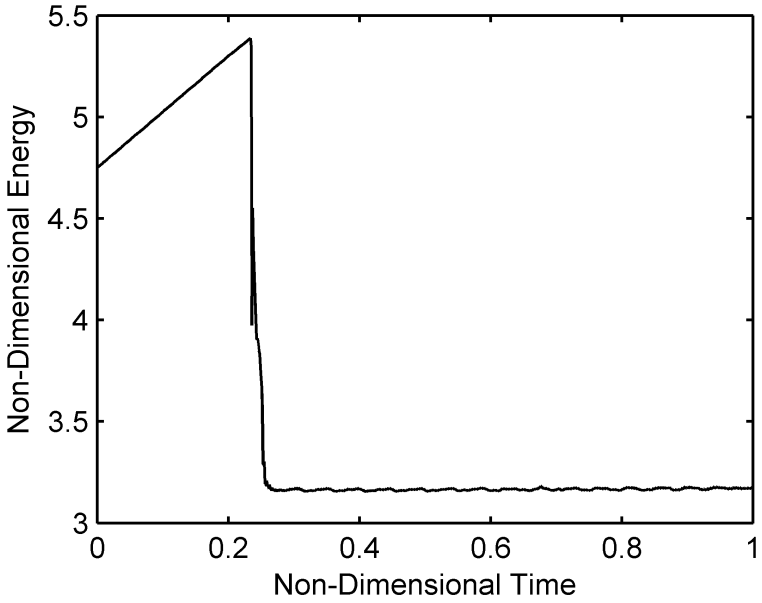

Figure A.23.: Non-Dimensional energy with time for plug to droplet transitions at $\theta = 70°$. Initial Volume = 2.0. Transition Volume = 1.06.

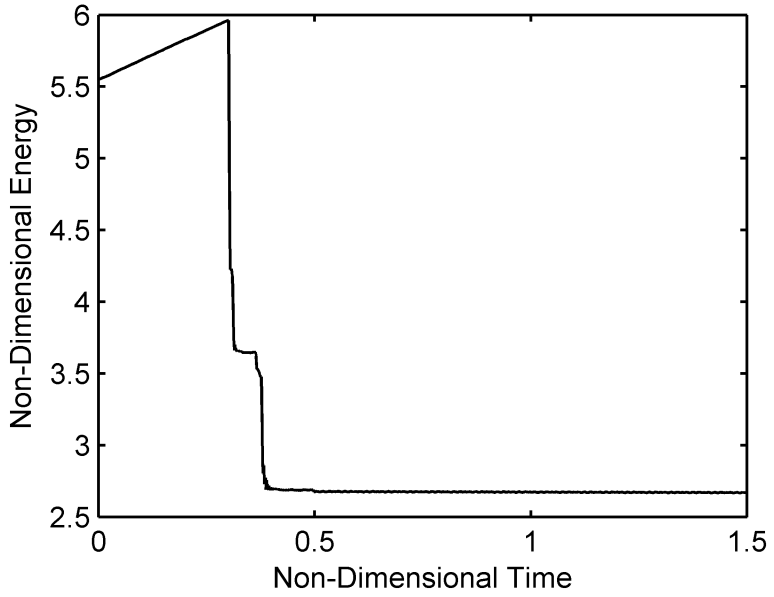

Figure A.24.: Non-Dimensional energy with time for plug to droplet transitions at $\theta = 80°$. Initial Volume = 2.0. Transition Volume = 0.79.

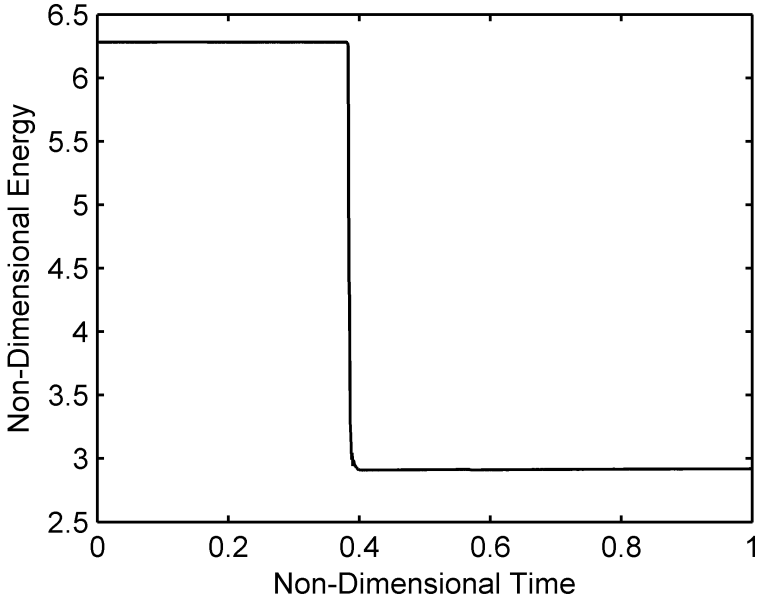

Figure A.25.: Non-Dimensional energy with time for plug to droplet transitions at $\theta = 90°$. Initial Volume = 2.0. Transition Volume = 0.52.

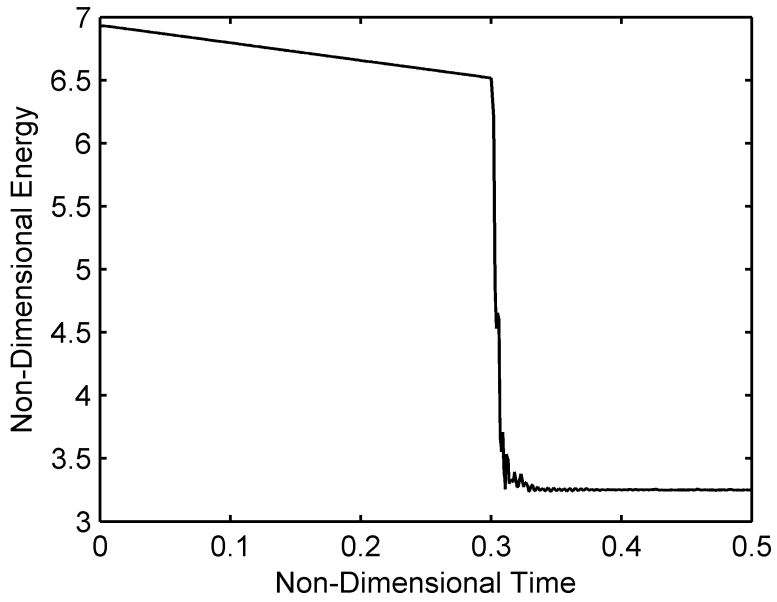

Figure A.26.: Non-Dimensional energy with time for plug to droplet transitions at $\theta = 100°$. Initial Volume = 2.0. Transition Volume = 0.79.

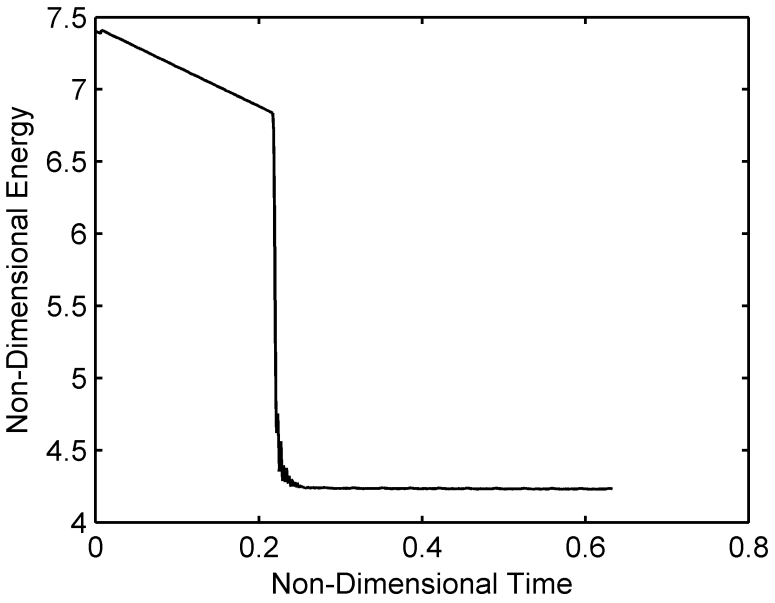

Figure A.27.: Non-Dimensional energy with time for plug to droplet transitions at $\theta = 110°$. Initial Volume = 1.92. Transition Volume = 1.05.

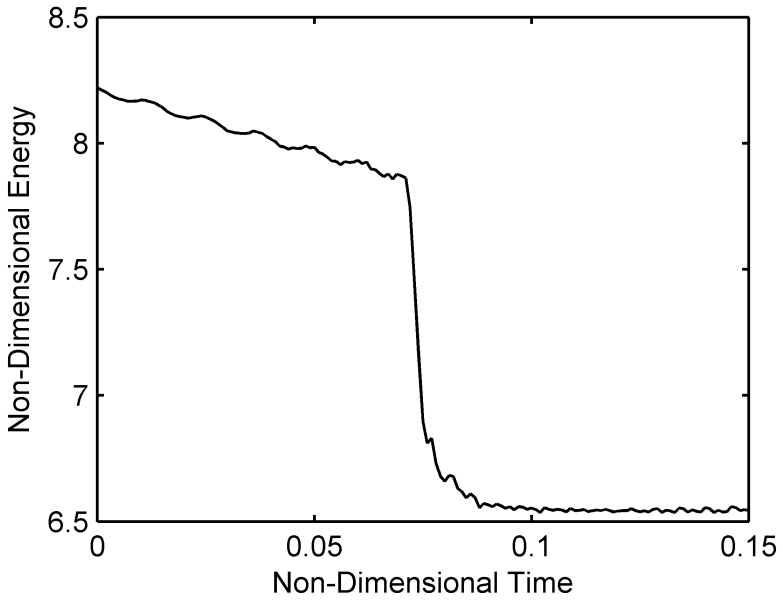

Figure A.28.: Non-Dimensional energy with time for plug to droplet transitions at $\theta = 130°$. Initial Volume = 2.0. Transition Volume = 1.72.

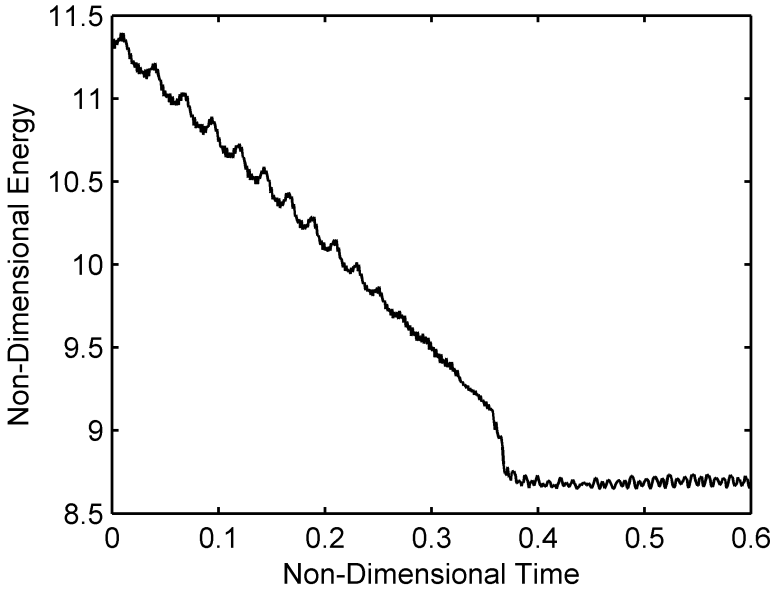

Figure A.29.: Non-Dimensional energy with time for plug to droplet transitions at $\theta = 140°$. Initial Volume = 4.0. Transition Volume = 2.15.

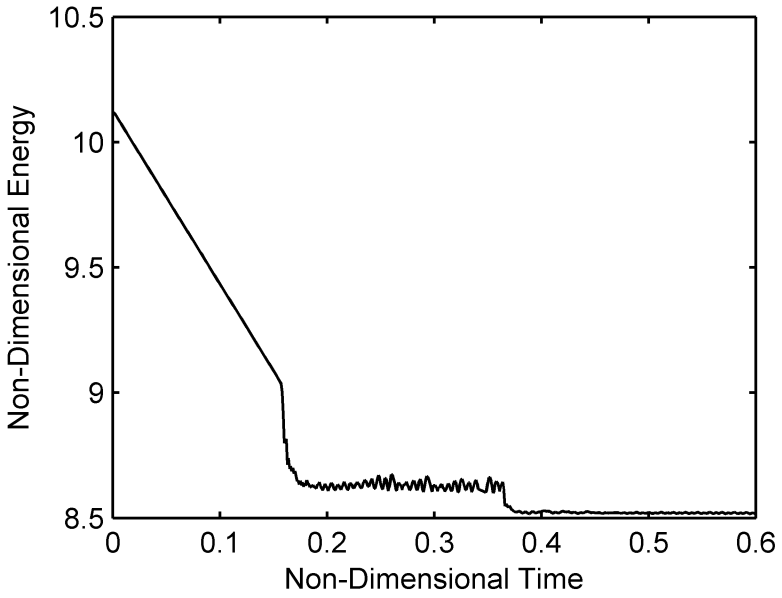

Figure A.30.: Non-Dimensional energy with time for plug to droplet transitions at $\theta = 150°$. Initial Volume = 3.0. Transition Volume = 2.37.

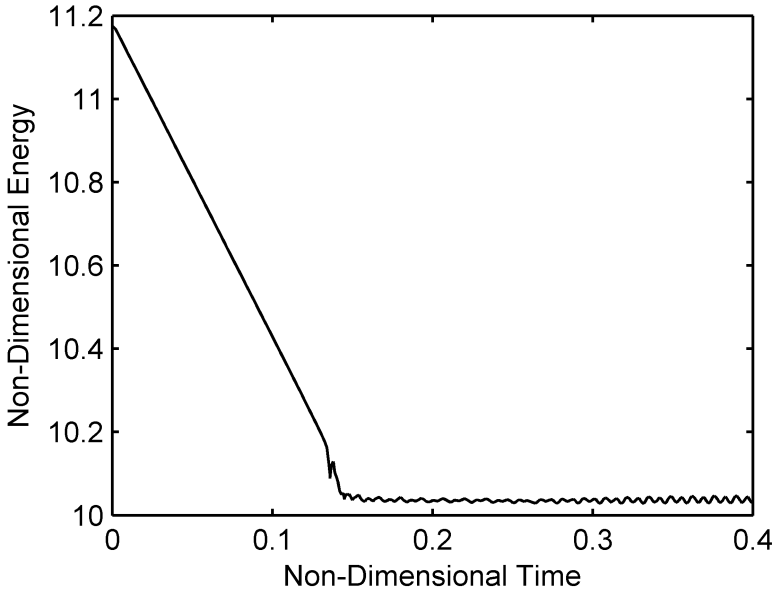

Figure A.31.: Non-Dimensional energy with time for plug to droplet transitions at $\theta = 160°$. Initial Volume = 3.5. Transition Volume = 2.97.